Quantifying fluvial and glacial erosion using (detrital) thermochronology, cosmogenic nuclides and numerical modelling:
A case study in the European Alps

Von der Naturwissenschaftlichen Fakultät der
Gottfried Wilhelm Leibniz Universität Hannover

zur Erlangung des Grades
Doktorin der Naturwissenschaften (Dr. rer. nat.)

genehmigte Dissertation
von
Cornelia Wangenheim, M. Sc.

[2016]

Referent: Dr. Christoph Glotzbach
Korreferent: Prof. Dr. Ulrich Heimhofer
Tag der Promotion: 25.11.2016

Abstract

The shape of Alpine landscapes is predominantly controlled by the interaction of tectonics and erosion. The latter is mainly influenced by climate, which regulates the relative contribution of fluvial and glacial erosion. However, the exact impact of these processes on the Alpine landscape evolution is still unclear. Therefore, the overall aim of this thesis is to quantify the influence of fluvial and glacial erosion on Alpine valley evolution in the Central European Alps since the Miocene. The study area is located in the Aar massif, which is an external massif in the Central Alps of Switzerland.

Thermochronological methods are applied to estimate surface cooling ages, long-term exhumation rates and the provenance of fluvial sediments. Three different thermochronometers are used to cover different time spans; zircon fission track (ZFT), apatite fission track (AFT) and apatite (U-Th-Sm)/He (AHe) dating. The thermochronological data reveal that since the initial rapid exhumation of the Aar massif (17 - 12 Ma), the massif has been exhumed uniformly with 0.5 km/Ma. Thermal models indicate strongly elevation-dependent different cooling events, but in this thesis they are associated with a high-relief topography induced perturbation of near surface isotherms. Nevertheless, the spatial distributions of AFT and AHe ages suggest an increase of exhumation at a distinct elevation range within the last 2 Ma. The focused accelerated exhumation is assigned to effective glacial erosion around the equilibrium line of altitude (ELA) of extensive Pleistocene glaciations. Numerical models prove that focused erosion may have influenced the exhumation rates at this distinct elevation range.

Provenance analyses of stream sediment with detrital AFT combined with the measurement of recent catchment-wide denudation rates demonstrate the distribution of erosion in Alpine valleys during an interglacial. The denudation rates are based on cosmogenic-produced ^{10}Be in quartz. The erosion pattern in Alpine valleys is still characterized by the impact of present and past glaciers: glacial erosion at the ELA of present-day glaciers and fluvial erosion around the ELAs of Pleistocene glaciers. Corresponding recent denudation rates indicate that glacial erosion is at least twice as effective as fluvial erosion. In contrast, fluvial erosion rates coincide with long-term exhumation rates.

Summarized, the impact of a cooling climate exceeds the influence of fluvial erosion on the landscape evolution. Therefore, climate changes that may have led to shifts in the precipitation pattern may not be reproducible with the exhumation history.

Keywords: Alpine landscape evolution, glacial erosion, thermochronology

Zusammenfassung

Das Erscheinungsbild alpiner Landschaften wird vorwiegend durch das Zusammenspiel von Tektonik und Erosion reguliert. Letztere wird durch das Klima beeinflusst, indem es die Anteile von fluviatiler und glazialer Erosion bestimmt. Die Auswirkungen dieser Prozesse auf die Landschaftsentwicklungsgeschichte im alpinen Raum sind jedoch noch nicht vollständig geklärt. Das Ziel dieser Dissertation besteht daher darin, die Einflüsse fluviatiler und glazialer Erosion im Bezug auf die Entwicklung von Alpentälern seit dem Miozän in den zentralen europäischen Alpen zu rekonstruieren. Das Arbeitsgebiet befindet sich im Aarmassiv, einem Externmassiv in den zentralen Alpen der Schweiz.

Mit Hilfe von thermochronologischen Methoden werden Abkühlalter, langfristige Exhumationsraten und Herkunftsgebiete fluviatiler Sedimente bestimmt. Hierfür werden drei unterschiedliche Thermochronometer benutzt: Zirkon-Spaltspuranalyse (ZFT), Apatit-Spaltspuranalyse (AFT) und Apatit (U-Th-Sm)/He Datierung (AHe). Die thermochronologischen Alter zeigen auf, dass seit der anfänglichen, schnellen Exhumation (17 – 12 Mio. Jahre) des Aarmassivs, die Exhumationsraten konstant und gleichmäßig bei 0.5 km/Ma sind. Allerdings deuten thermische Modelle auf unterschiedliche Abkühlungsereignisse hin, die jedoch deutlich von der Höhe abhängig sind und deswegen vermutlich eher eine Folge eines gestörten Verlaufs von oberflächennahen Isothermen unterhalb einer ausgeprägten Topographie sind. Die räumliche Verteilung von AFT und AHe Altern weist dennoch auf einen Anstieg der Exhumation innerhalb der letzten 2 Mio. Jahre an einer bestimmten Höhe hin. Die konzentrierte, verstärkte Exhumation wird als Folge von effektiver, glazialer Erosion um die Gletschergleichgewichtslinie der maximal ausgedehnten Pleistozänen Gletscher angesehen. Numerische Modelle belegen, dass diese konzentrierte Erosion die Exhumationsraten an dieser bestimmten Höhe beeinflusst haben könnte.

Basierend auf den Herkunftsgebieten der Flusssedimente, die mit Hilfe von AFT ermittelt wurden, ergibt sich die Verteilung der Erosion in Alpentälern während eines Interglazials. Diese Ergebnisse kombiniert mit der Messung der Konzentration von in-situ produziertem ^{10}Be in den Flusssedimenten resultiert in der räumlichen Verteilung rezenter Erosionsraten. Die Erosionsverteilung in den Alpentälern ist noch immer durch die Auswirkungen von heutigen und früheren Gletschern geprägt. Hierbei stellt sich heraus, dass die Erosion hauptsächlich auf zwei Bereiche konzentriert ist; glaziale Erosion unterhalb der heutigen Gletschergleichgewichtslinie und fluviatile Erosion auf der Höhe der ehemaligen Gletschgleichgewichtslinie des Pleistozän. Die dazugehörigen Erosionsraten belegen, dass die glaziale Erosion

mindestens zweimal so effektiv ist wie die fluviatile, die mit den langfristigen Exhumationsraten übereinstimmt. Daraus folgt, dass die Auswirkungen eines sich abkühlenden Klimas deutlich den Einfluss von fluviatiler Erosion im Bezug auf die Landschaftsentwicklung übersteigen. Demnach sind vermutlich Klimaveränderungen, die zu einer Veränderung im Niederschlagsmuster führten, nicht auflösbar mit der Exhumationsgeschichte.

Schlagwörter: Alpine Landschaftsentwicklung, glaziale Erosion, Thermochronologie

Contents

Abstract III

Zusammenfassung V

Contents VII

List of abbreviations XI

1 Objectives and background 1

1.1 The evolution of the European Alps . . . 5

1.2 Thermochronology . . . 9

1.2.1 Fission track dating . . . 11

1.2.2 (U-Th-Sm)/He Dating . . . 15

1.3 Synopsis . . . 18

References . . . 18

2 Exhumation history of the Aar massif 25

2.1 Abstract . . . 26

2.2 Introduction . . . 27

2.3 Geological setting . . . 29

2.4 Methods . . . 32

2.4.1 Fission track dating . . . 35

2.4.2 (U-Th-Sm)/He dating . . . 35

2.4.3 Thermal modelling . . . 36

2.5 Results . . . 37

2.5.1 ZFT ages . . . 37

2.5.2 AFT ages . . . 40

2.5.3 AHe ages . . . 42

2.6 Discussion . . . 44

2.6.1 Initial exhumation of the Aar massif . . . 44

2.6.2 Exhumation history since Late Miocene . . . 48

2.6.3 Overlapping AFT and AHe ages . . . 55

2.7 Conclusions . . . 56

2.8 Appendix 57
References 58

3 Maximum glacial erosion around the equilibrium line altitude of glaciers: New insights from low-temperature thermochronology 65
3.1 Abstract 66
3.2 Introduction 67
3.3 Methods 69
3.4 Results 71
3.5 Discussion 73
3.6 Conclusions 76
3.7 Appendix 77
3.7.1 Thermal-kinematic modelling of AFT ages 77
3.7.2 Thermal modelling 79
References 80

4 Non-uniform erosion in Alpine catchments lead to bias in cosmogenically derived denudation rates 85
4.1 Abstract 86
4.2 Introduction 87
4.3 Study area 89
4.3.1 Tectonic evolution 89
4.3.2 Geomorphic setting 90
4.4 Methods 93
4.4.1 Sampling 94
4.4.2 Detrital thermochronology 94
4.4.3 ^{10}Be catchment-wide denudation rates 97
4.4.4 Modifying catchment-wide denudation rates 99
4.5 Results 104
4.5.1 Detrital thermochronology 104
4.5.2 ^{10}Be-derived denudation rates 107
4.6 Discussion 109
4.6.1 Controls on the erosion pattern 110
4.6.2 Erosion pattern-weighted denudation rates 115
4.6.3 Future potential 116
4.7 Conclusions 117
4.8 Appendix 118
References 120

5 Summary and conclusions **129**
5.1 The exhumation history of the Aar massif - tectonics or climate changes ? . 130
5.2 The landscape evolution of inner-Alpine valleys during the glaciations . . . 132
5.3 The distribution of erosion in the present-day interglacial 133
5.4 Conclusions 135
References 136

Acknowledgements/Danksagung **139**

Curriculum vitae **141**

List of abbreviations

^{4}He	Helium isotope
^{10}Be	Beryllium isotope
^{147}Sm	Samarium isotope
^{232}Th	Thorium isotope
^{238}U, ^{235}U	Uranium isotopes
$^{40}Ar/^{39}Ar$	argon-argon dating
AFT	apatite fission track
AHe	(U-Th-Sm)/He dating on apatites
CDF	cumulative density function
Cl-apatite	chlorine - apatite
D_{par}	length of etch figure parallel to the crystallographic c-axis that appears if fission track intersects crystal surface
ELA	equilibrium line of altitude of glaciers
F-apatite	fluorine - apatite
Ft correction	He particle ejection correction for apatites
LGM	Last Glacial Maximum
LIA	Little Ice Age
MAAT	mean annual air temperature
MTL / TL	mean (confined) track length
PAZ	partial annealing zone; where fission tracks are annealed and shortened
PRZ	partial retention zone; where He is partially retained or ejected
Tc	closure temperature of thermochronometer
tT-model	time-Temperature model
SRTM	Shuttle Radar Topography Mission
ZFT	zircon fission track

1 Objectives and background

During my dissertation I investigated the short- to long-term impact of glacial and fluvial erosion on the landscape evolution in an Alpine setting. Present landscapes of mountainous areas throughout the world obtain their characteristic relief by an interaction between active tectonics (tectonic deformation and rock uplift) and erosion at the surface. Therefore, erosion, independently of prevailing fluvial or glacial erosion, is crucial for the evolution of orogens, because (1) the height of mountain ranges mainly grows until a steady-state between tectonics and erosion is achieved and (2) the present shape of mountains is mainly the result of erosion (e.g. Willett, 1999; Willett and Brandon, 2002). Consequently, the quantification of erosional processes is necessary for the understanding of the landscape evolution of mountain ranges.

This work focuses on the European Alps, in which the study area is located in the Central Alps of Switzerland, in the Bernese Alps (Fig. 1.1). In the Central Alps, Alpine convergence rates have decreased within the last 10 Ma and are presently nearly non-existent (e.g. Schmid et al., 1996; Schlatter et al., 2005). In contrast, there is a lack of understanding of the distribution of erosion during the same time interval. Sediment budget analyses reveal increasing erosion rates since the last 5 Ma (e.g. Cederbom et al., 2004; Willett et al., 2006; Kuhlemann et al., 2002), whereas exhumation rate patterns display steady-state exhumation rather than accelerated erosion (e.g. Bernet et al., 2001; Glotzbach et al., 2011; Vernon et al., 2008). This dissertation concentrates on the landscape evolution since Miocene, which also comprises several glacial and interglacial cycles within the Quaternary. The identified distributions of exhumation provide information about the erosion pattern in a million year time scale, whereas estimated recent erosion rates reflect the past 1 ka. Consequently, this study will identify the influence of climate shifts on the topography as well as the relative contributions of fluvial and glacial erosion.

Central questions of this study:

The aim of this study is to reconstruct how the Alpine landscape has been evolved since Miocene with an emphasis on the impact of glacial erosion on inner-Alpine valleys. This thesis addresses the following questions:

(1) **How did the exhumation pattern evolve through time and did the exhumation rates display any of the proposed erosion pulses - and if so, which were the triggering processes?**
By now, two distinct erosion pulses are suggested for the Central Alps. A first one is supposed to have taken place at 5 Ma as demonstrated by sediment budget calculations and thermochronology in the North Alpine foreland basin (e.g. Willett et al., 2006; Kuhlemann et al., 2002; Cederbom et al., 2004). A second one is assumed to have led to increasing erosion rates, because of the extensive glaciations during the Pleistocene (e.g. Haeuselmann et al., 2007; Valla et al., 2011; Glotzbach et al., 2010, 2013). Instead, at orogen-scale, a steady-state exhumation is suggested by detrital and bedrock thermochronology for the same period of time (e.g. Bernet et al., 2001; Glotzbach et al., 2011). This study is intended to resolve the exhumation pattern regarding these two or more erosion pulses as well as their driving forces.

(2) **How intense was the impact of glacial erosion during Pleistocene glaciations on inner-Alpine valleys?**
It is known that glacial erosion during the most extensive glacial advances in Pleistocene led to accelerated valley incision of Alpine valleys (e.g. Valla et al., 2011; Haeuselmann et al., 2007). However, only little is known about the factors that triggered valley incision as well as about the local distribution of glacial erosion in different valleys. The concern of this thesis is to provide a better understanding of the distribution of glacial erosion in inner-Alpine valleys during the Pleistocene.

(3) **During the present interglacial, how is the spatial distribution of erosion and which processes control the pace and location of erosion?**
Recent cosmogenic-nuclide derived erosion rates on stream sediments reflect the mean erosion rate of sample points' upstream catchment (e.g. von Blanckenburg, 2005), but it is not distinguished between fluvial or glacial erosion. However, recent studies in the European Alps observed either a large influence of glacial erosion (Delunel et al., 2014) or of fluvial erosion (Fox et al., 2015) on Alpine catchments. In this thesis an innovative approach using bedrock and detrital thermochronology is applied to estimate present-day sediment provenances. The results are used to modify catchment-wide denudation rates.

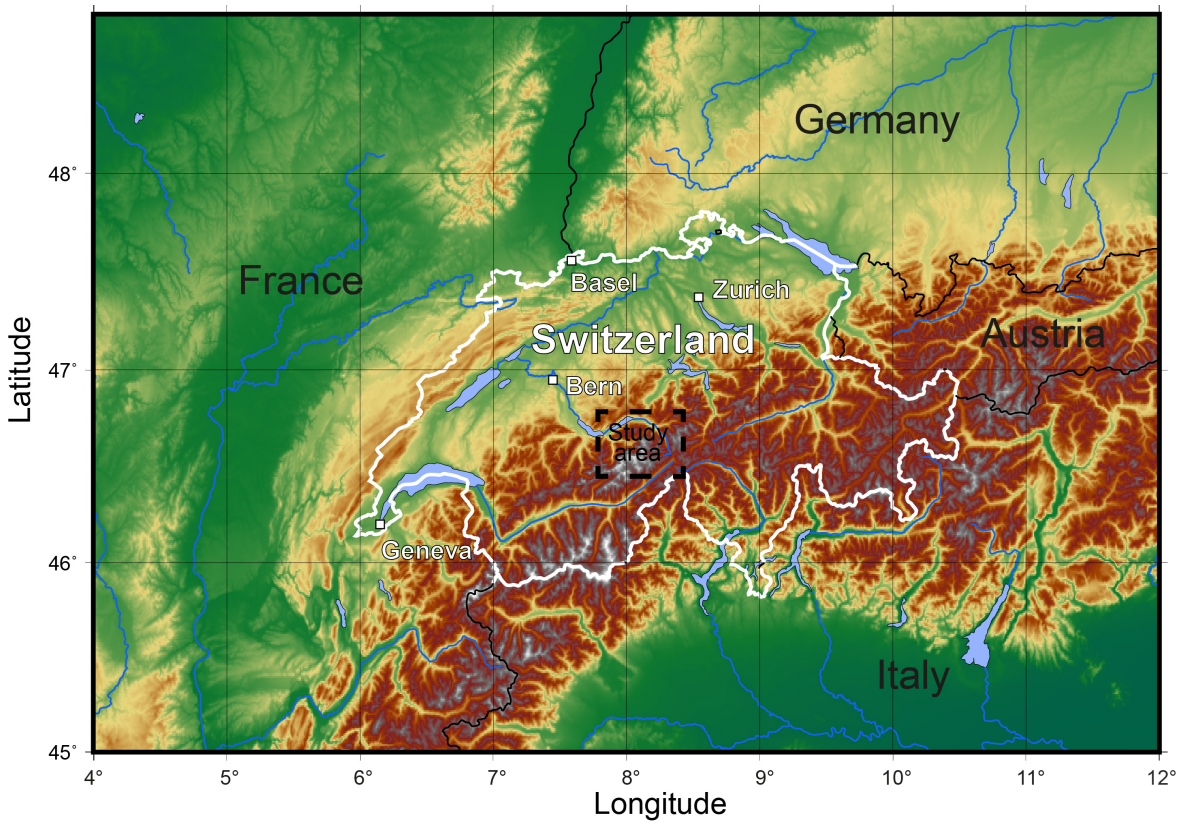

Figure 1.1: Location of the study area in the Central Alps of Switzerland. The topography is based on 90 m SRTM data (USGS, 2006).

1.1 The evolution of the European Alps

The European Alps are the result of continent-continent collision involving several (micro-) tectonic plates and ocean basins, whereby the main driving forces originate from the convergence between Europe and Africa. The geology of the Alps is nowadays divided into three major units (Helvetic, Penninic, and Austroalpine and South Alpine) that are describing their paleogeographic position prior the collision (e.g. Frisch, 1979). The evolution of the Alps is explained briefly in the following section.

In the Early Mesozoic era, the supercontinent Pangaea broke apart into several small continental plates and ocean basins, which were later involved in the Alpine orogeny (Frisch, 1979). It is assumed that the formation of the European Alps can be separated into two different orogenies each followed by extensional overprinting (e.g. Schmid et al., 1996, 2004; Froitzheim and Manatschal, 1996; Froitzheim et al., 1994; Steck and Hunziker, 1994); the first one during the Cretaceous is followed by a second one during the Early Cenozoic. The first orogenic phase in the Early Cretaceous started with the closure of the Meliata ocean. The Meliata ocean opened during Middle Triassic in a south-eastern position of the later Alps. The closure of the ocean resulted in a collision of various micro-plates, in which the later Adriatic plate was involved. The collision was presumably driven by a southeast-dipping intra-oceanic subduction zone forming an early mountain range. The collision caused an arising instability of the early orogen, resulting in orogen-parallel extension (Froitzheim et al., 1994). Remnants of this former ocean basin are rare and are only found in the Austroalpine unit in the Eastern Alps (Schmid et al., 1996).

The second orogenic phase in the Early Cenozoic is the main collision phase during Alpine orogeny. This phase is characterized by the closure of ocean basins and subduction of microtectonic plates between the Adriatic and European continent. This was preceded by the opening of the Piedmont-Liguria ocean in the Late Triassic / Early Jurassic that separated the Adriatic continent from the European plate. The opening is assumed to be kinematically linked to the opening of the Central Atlantic ocean (e.g. Schmid et al., 2004; Frisch, 1979). As a result of the ongoing opening of the Northern Atlantic ocean in the Early Cretaceous, a second ocean opened; the Valais ocean at the southern margin of the European continent separated the micro-continent Briançonnais from Europe (e.g. Frisch, 1979). The positions of continental and oceanic plates at this stage are shown in Fig. 1.2. Note that the actual positions of former oceans and continents are still a matter of debate and thus Fig 1.2 only provides a simplified overview.

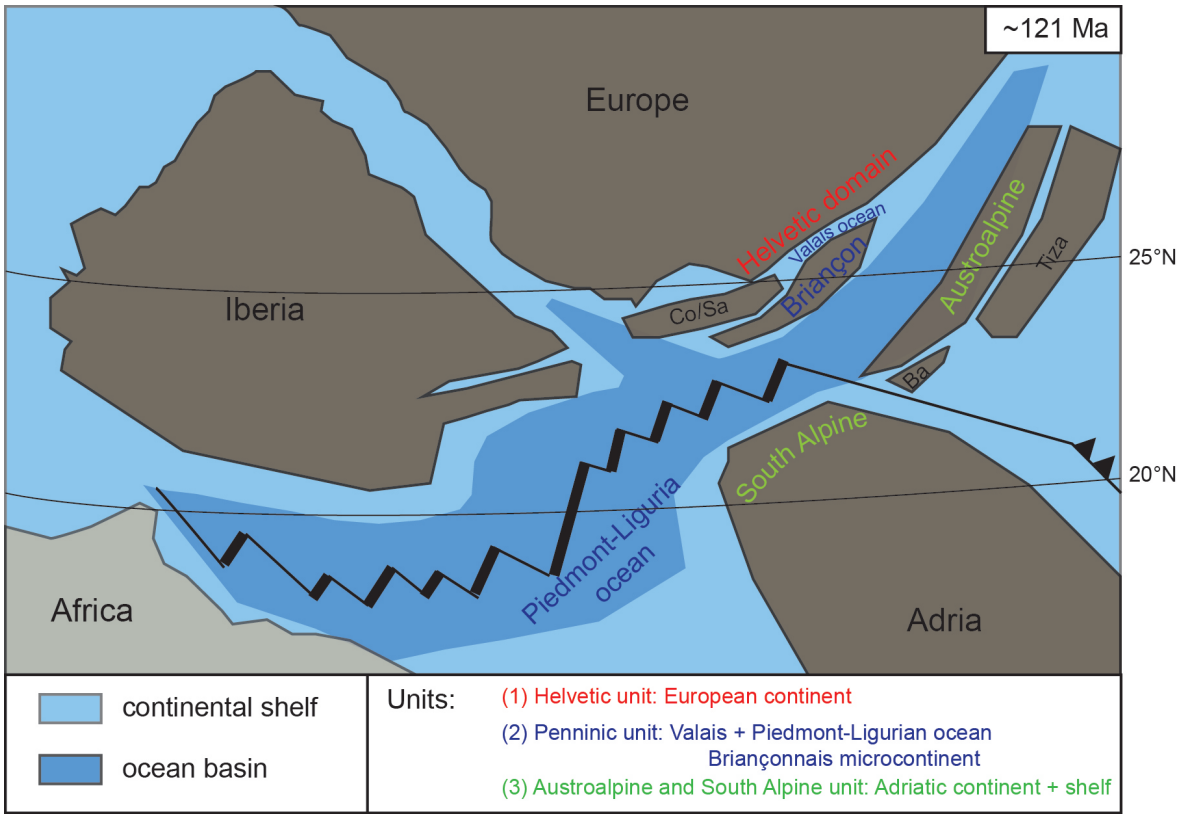

Figure 1.2: Paleogeographic postion of Alpine units in the Lower Cretaceous simplified after Wortmann et al. (2001). Co/Sa corresponds to Corsica and Sardinia, Tiza is now found in the Northwest Dinarides and Romanian Carpathians and Ba corresponds to the Bakony mountains.

According to these paleogeographic locations of oceans and (micro-) continents, the geology of the Alps is classified. In the north, the European continent and corresponding distal margin is assigned to the Helvetic unit. In the south, the Adriatic continent is subdivided into a northerly part corresponding to the Austroalpine and a more southerly part associated with the South Alpine. The Austroalpine and South Alpine are combined, because both parts have never been separated by an ocean and therefore comprise continental deposits of the Adriatic continent. Between both described units were located the Briançonnais, and the Valais and Piedmont-Liguria oceans. The continental deposits and oceanic rocks are assigned to the Penninic unit (Fig. 1.2).

The collision and nappe stacking started with the south-southeastward subduction of the Piedmont-Liguria ocean below the Adriatic continent (South Alpine and Austroalpine unit) at 95 Ma, followed by the subduction of the Briançonnais at ~65 Ma (Fig. 1.3 A). A second southward subduction zone successively closed the Valais ocean. During subduction, the geologic parts corresponding to the Penninic unit were partly metamorphosed up to eclogite facies. The entire width of the Briançonnais was subducted completely in the Late Eocene (~50 Ma) and led to the collision and subduction of the European margin, whereby rocks

of the Helvetic unit were mainly metamorphosed to greenschist and amphibolite facies (e.g. Frisch, 1979; Schmid et al., 1996; Marquer and Burkhard, 1992). The collision between the European continent and the Adriatic indenter caused crustal shortening and finally the uplift of the Alps (e.g. Steck and Hunziker, 1994). Highest convergence rates of 1.3 to 1.5 cm/a have been achieved during that time period (between 65 and 40 Ma) (Schmid et al., 1996). According to the position during collision, the Austroalpine unit as the southernmost unit, is highest and rested upon the Penninic and Helvetic units. However, in the Early Oligocene (~32 Ma) parts of the European continent (Helvetic unit) started to exhume due to back-thrusting onto the Austroalpine (southern unit) along the Insubric Line (Fig. 1.3 B). Back-thrusting combined with erosion led to exhumation of large parts of the Helvetic and Penninic units in central parts of the Alps (Schmid et al., 1996).

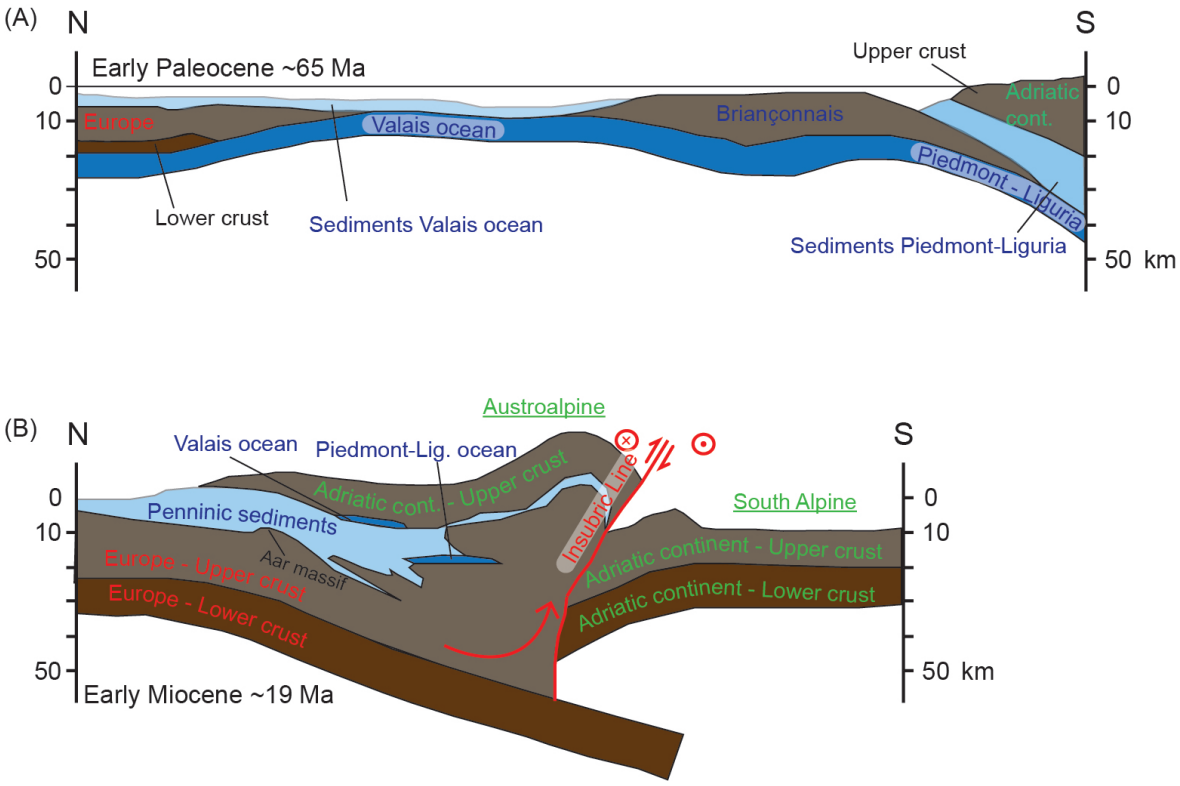

Figure 1.3: **(A)** and **(B)** schematic transect through the Central Alps displaying the kinematic evolution in the Oligocene and Early Miocene, simplified according to Schmid et al. (1996). Note that for the Early Miocene a first updoming of the Aar massif is suggested.

Since Early Oligocene, the North Alpine foreland basin has been subsided and recorded the tectonic evolution of the Alps with deposited Molasse sediments. In the Late Miocene / Early Pliocene the basin was inverted and instead of accumulating sediments, it began to erode (e.g. Cederbom et al., 2004; Willett et al., 2006; Schmid et al., 2004). Simultaneously, the Alps are proposed to have been changed from orogenic construction to orogenic deconstruction (e.g. Willett et al., 2006). Since Late Eocene (40 Ma), the convergence rates have decreased successively to almost no convergence today in the Central Alps (Schmid et al., 1996). In contrast, only in the Eastern Alps ongoing convergence is detected, because of the continuing anticlockwise-rotation of the Adriatic indenter (e.g. Grenerczy et al., 2000). Present-day horizontal movements derived by GPS measurements therefore indicate a N-S shortening with a rate of 2 mm/a in the Eastern Alps, whereas west of a longitude of 10°E horizontal crustal movement in the Central and Western Alps is almost non-existent ($<$1 mm/a) (Nocquet, 2012; D'Agostino et al., 2005).

This Cenozoic orogeny led to orogen-parallel extension due to lateral escape of crustal material perpendicular to the direction of convergence (e.g. Mancktelow, 1992; Steck and Hunziker, 1994). In the Central Alps, for example, the extension resulted in rapid exhumation of the Lepontine Gneiss dome and in movement along the prominent Simplon Fault zone, which is assumed to be still active (Steck and Hunziker, 1994; Mancktelow, 1992; Seward and Mancktelow, 1994; Campani et al., 2010).

This dissertation focuses on the Aar massif, which comprises crystalline rocks of the European continent and therefore it belongs to the Helvetic unit. Besides the Aar massif, there are further external massifs at which basement rocks from the former European margin are outcropping in an orogen-parallel string on the northern and western rim of the Alps, e.g. Mont Blanc massif, Belledonne Massif, Argentera Massif and Pelvoux Massif (e.g. Schmid et al., 2004).

The exhumation of the Aar massif began in Miocene (e.g. Michalski and Soom, 1990; Vernon et al., 2009) (cf. Fig. 1.3 B). The northern boundary of the Aar massif is limited by the Helvetic thrust at which the crystalline rocks and the sedimentary cover of the Aar massif were thrust onto Helvetic nappes (e.g. Labhart, 1977). This thrust may mark the boundary between autochthon and allochthon European foreland. The uplift of the Aar massif is proposed to be a consequence of a ramp-fold at the detachment between lower and upper European crust (Schmid et al., 1996). For a detailed description of the evolution of the Aar massif, please refer to chapter 2.

1.2 Thermochronology

Samples in this thesis are mainly analysed by thermochronological methods to evaluate the long-term exhumation pattern and reconstruct the landscape evolution. Hence, this section focuses on the methodological details of thermochronology, analytical details are provided in the following chapters. Numerical modelling based on thermochronological ages as well as the calculation of cosmogenic ^{10}Beryllium (Be)-derived catchment-wide denudation rates are described in chapters 3 and 4.

Thermochronology is based on the accumulation of daughter products through naturally occurring radioactive decay reactions of parent isotopes in geologic relevant material and the removal of that daughter product by thermal activated processes (e.g. Reiners, 2005; Braun et al., 2006). The ages (t) can be determined, because the decay rate of the radioactive decay is known, which results in this general form of the isotopic age equation:

$$t = \frac{1}{\lambda} ln(\frac{N_d}{N_p} + 1), \tag{1.1}$$

whereby λ is the decay constant, and N_d and N_p are the number of daughter and parent isotopes, respectively. Generally, thermochronology provides information about the thermal and temporal history of rocks or minerals and therefore differs from geochronology, which is solely used to determine the absolute timing of geologic events (e.g. Reiners, 2005).

The age of minerals, whose calculation is based on the accumulation of daughter isotopes, depends on the time when the mineral was at its closure temperature (Dodson, 1973). At temperatures lower than the mineral-dependent closure temperature, daughter isotopes are retained or fission tracks are produced in the minerals, whereas at higher temperatures, the daughter products diffuse or fission tracks are erased as fast as they are formed. If, therefore, the mineral cooled rapidly and uniform, the thermochronological ages would ideally refer to the time since the mineral has left the closure temperature range (cooling age) (e.g. Reiners, 2005). The age also depends on the cooling rate that is associated with the exhumation rate (Fig. 1.4) (e.g. Braun et al., 2006). In this context, exhumation describes the history of the vertical displacement of rocks with respect to the Earth's surface, which is caused by the combined processes of active tectonics triggering rock uplift and erosion at surface (England and Molnar, 1990).

There are three commonly used thermochronometers; ^{40}Ar/^{39}Ar (argon-argon dating) on micas, amphiboles and K-feldspars (e.g. McDougall and Harrison, 1999), Fission track thermochronology on apatites and zircons (e.g. Gallagher et al., 1998; Tagami et al., 1996) and (U-Th-Sm)/He (uranium-thorium-samarium/helium) dating on apatites and zircons (e.g. Farley, 2002). Each thermochronometer is based on different closure temperatures and therefore provides cooling information over different time scales. The higher the closure temperature

the deeper the isotherm of the closure temperature and consequently the longer the time of exhumation. In this thesis, fission track dating on apatites (AFT) and zircons (ZFT), and (U-Th-Sm)/He dating on apatites (AHe) are applied.

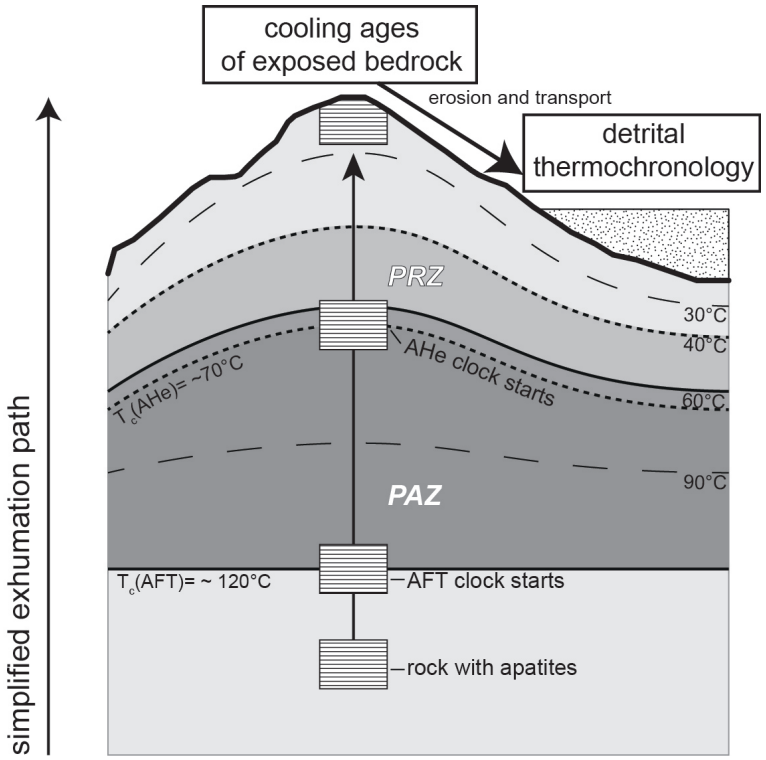

Figure 1.4: Simplified description of the concepts of apatite fission track (AFT) and (U-Th-Sm)/He dating on apatites. Modified from Bernet et al. (2009).

These two methods are commonly applied to calculate cooling ages on bedrocks to reconstruct the thermal evolution of sedimentary basins for hydrocarbon exploration (e.g. Gleadow et al., 1986) as well as to estimate exhumation rates for the reconstruction of the evolution of mountain belts (e.g. Spotila, 2005). Provenance analysis in sedimentary basins is also common, as thermochronological age compositions provides information about the denudation rates, paleodrainage directions and/or depositional ages (Fig. 1.4). For detrital thermochronology it is supposed that the time of exposure is the same as the time of deposition. The period of time between exposure and deposition (residence time) is assumed to be insignificant compare to the old thermochronological ages and their large errors (e.g. Bernet et al., 2009; Wagner and van den Haute, 1992).

1.2.1 Fission track dating

Fission track dating was first introduced in the 1960s by the pioneering work by Fleischer et al. (1965) and further developed within the last 30 years (e.g. Green et al., 1986; Gallagher et al., 1998). This method is based on the spontaneous decay of ^{238}U, which is naturally incorporated in several minerals (e.g. zircons and apatites) during crystallization (e.g. Tagami and O'Sullivan, 2005). ^{238}U does not only decay by α or β emissions, there is also a small proportion at which ^{238}U decays by forming nuclear fissions. The spontaneous fission of a ^{238}U isotope, in general, occurs only with very low probability; for example, decay reactions by α or β emissions occur 2 x 10^6 times more frequently than spontaneous fission (e.g. Galbraith, 2005; Tagami and O'Sullivan, 2005).

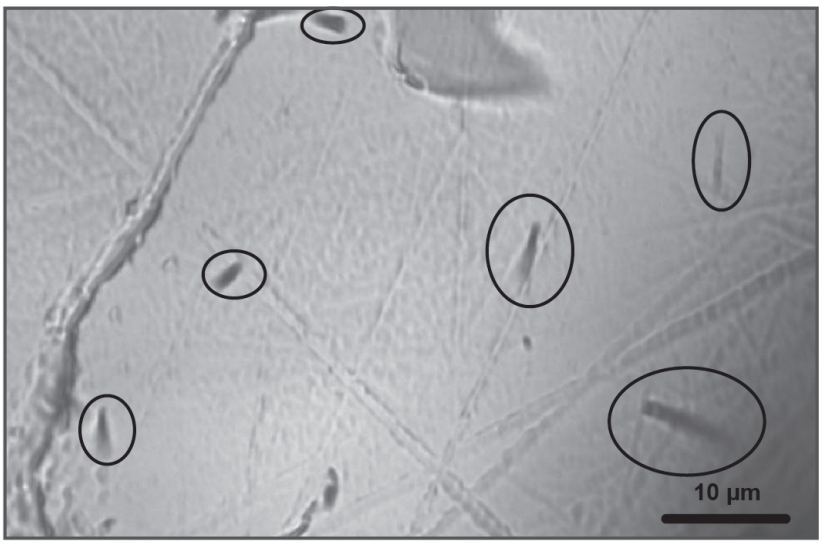

Figure 1.5: Spontaneous fission tracks in apatite (Photo from sample CGP236).

In the process of nuclear fission, an unstable nucleus splits into two positively charged high-energy nuclei that are propelled away in opposite directions, creating a randomly oriented single linear trail (e.g. Tagami and O'Sullivan, 2005; Galbraith, 2005; Braun et al., 2006). If this reaction takes place in a mineral, a damage trail will be formed, which is named fission track. Consequently, calculating an age will be possible if the relative abundance of the number of ^{238}U isotopes "parent product" and the number of spontaneous fission tracks "daughter product" per unit volume is estimated (cf. equation 1.1).
When they are formed, spontaneous fission tracks in apatites and zircons are about 16-17 µm and 11 µm long (Fig. 1.5). The width of fission tracks ranges between 0.0025 - 0.0050 µm

(e.g. Li et al., 2010, 2011, 2012). Fission tracks can be revealed by chemical etching, thus the counting of the spontaneous fission of ^{238}U isotopes under an optical microscope will be possible (e.g. Gallagher et al., 1998). The abundance of ^{238}U "parent product" is estimated by determining the abundance of ^{235}U, because the ratio between ^{235}U/^{238}U is naturally constant. In order to achieve this, the minerals are irradiated with low-energy thermal neutrons in a nuclear detector and the ^{235}U isotopes are also able to decay by forming nuclear fissions (e.g. Gallagher et al., 1998). The induced tracks of the fission of ^{235}U, which refers to the abundance of ^{235}U, can also be revealed by chemical etching and are countable under an optical microscope (Tagami and O'Sullivan, 2005). Spontaneous and induced fissions are physically unrelated and therefore the numbers of isotopes that decayed by nuclear fissions are statistically independent (Galbraith, 2005)

There are three ways to estimate fission track ages, the population and the external detector method as well as the LA-ICP-MS-based fission track technique, whereby the external detector method is commonly used and was also applied in this study (Hurford and Green, 1982; Hurford, 1990; Gallagher et al., 1998; Hasebe et al., 2004; Chew and Donelick, 2012). The minerals are usually embedded in epoxy resin to prepare a mount. As a first step of the external detector method, the mount is grinded and polished to expose an internal surface. Secondly, the sample is etched to reveal the spontaneous tracks of the decay of ^{238}U (Fig. 1.5 and 1.6). As a third step, an external detector, usually a thin layer of muscovite, is attached to the sample. The sample and attached mica are irradiated simultaneously by thermal neutrons. Afterwards, the external detector is also etched to reveal the induced tracks of the decay of ^{235}U. Before the counting of spontaneous and induced tracks begins, a slide is prepared, which includes the spontaneous tracks on the one hand and the corresponding image of induced tracks on the other hand (Fig. 1.6) (e.g. Gallagher et al., 1998). Hence, the external detector method has the major advantage that single grains are considered individually, whereby grain-dependent variations of the uranium content are taken into account.

The external detector method is simplified by adding a ζ -factor, which is calibrated individually by each analyst by counting standard samples of known age (commonly used for AFT: Durango-apatite from Mexico) (Hurford and Green, 1983). The equation 1.1 is then transformed into the fission track age equation:

$$t = \frac{1}{\lambda_D} ln(\lambda_D \frac{\rho_s}{\rho_i} \rho_d \zeta g + 1), \tag{1.2}$$

whereby λ_D is the decay constant for ^{238}U, ρ_s and ρ_i are the densities of spontaneous and induced tracks (number of tracks/unit area), ρ_d is the track density of the dosimeter, g is a known geometry factor and the ζ-factor (e.g. Hurford and Green, 1983; Gallagher et al., 1998). During irradiation, the thermal neutron flux is constrained with a dosimeter glass

of known uranium concentration, which is irradiated simultaneously with the samples. The track density of this dosimeter is stated as ρ_d.
In practice, about 20 grains per sample are counted and the resulting age is reported with its central age. The central age is the logarithmic mean of the single-grain ages and corresponding age dispersion that depends on the relative standard error of the single-grain ages (Galbraith, 2005).
In contrast to the external detector method, the population method is based on the assumption that the distribution of uranium is uniform in each grain, why the sample is first separated into two splits at which only one split is irradiated. Both splits are embedded and counted individually; the unirradiated reveals the spontaneous tracks and the irradiated comprises the total track density (e.g. Naeser, 1979). For LA-ICP-MS-based apatite fission track thermochronology, the uranium concentration is measured with LA-ICP-MS. This approach has the advantage that samples do need to be irradiated, which increases the speed of analyses (Hasebe et al., 2004) as well as it enables the measurement of further elements (e.g. Th, Sm, Pb) at the same time, facilitating a combination of dating methods (e.g. with U-Pb dating). However, this method has also the disadvantage that grain-dependent variations of the uranium content can not be considered as it can be done with the external detector method (Chew and Donelick, 2012). Therefore, the assumption of an uniform distribution of uranium mainly limits the application of these methods and that is the reason why the external detector method is normally applied (e.g. Galbraith and Laslett, 1993; Gallagher et al., 1998; Braun et al., 2006).
An important characteristic of the fission track thermochronometer is its ability to anneal fission tracks with increasing temperature, which allows a reconstruction of the cooling history of the minerals. Thereby, atoms and electrons move through the crystal towards the ionized track, causing a shortening of tracks. If the tracks are shortened, the thermochronological ages will become younger, as there are fewer tracks to count (Green et al., 1986; Tagami et al., 1996). The temperature range at which fission tracks may efficiently anneal, the partial annealing zone (PAZ), varies and is associated with the mineral-dependent closure temperature; for example, the temperature range at which apatites may anneal is between 60 - 120°C (e.g. Wagner and van den Haute, 1992) and for zircons between 190 - 380°C (e.g. Rahn et al., 2004).

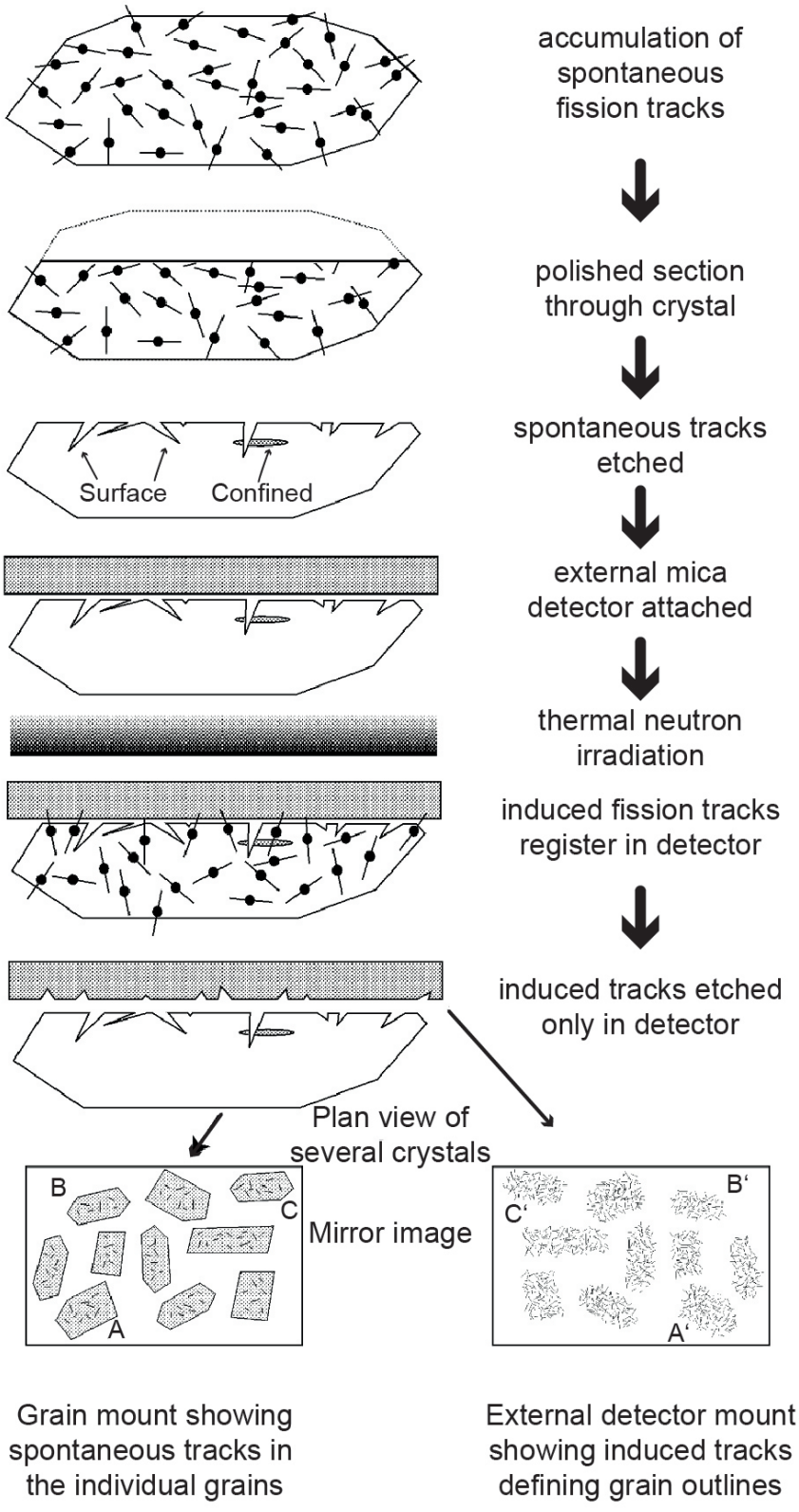

Figure 1.6: The external detector method according to Hurford and Green (1982); Hurford (1990) and illustrated by Gallagher et al. (1998).

To estimate if tracks are already shortened, a measurement of confined track lengths is required. Confined tracks are located below the mineral surface, ideally horizontal (subhorizontal) (Fig. 1.6), and represent the best approximation of true track length distributions (Gleadow et al., 1986; Green et al., 1989). Typically, 50 - 100 track lengths are measured under an optical microscope (e.g. Gallagher et al., 1998). It is more common to measure confined track length distributions in apatites than in zircons, because the process of annealing is more understood in apatites than in zircons (e.g. Wagner and van den Haute, 1992; Tagami et al., 1996)

For apatites it is assumed that annealing processes are influenced by the chemical composition (e.g. Green et al., 1986; Barbarand et al., 2003) and etching characteristics of the mineral (e.g. Wagner and van den Haute, 1992; Barbarand et al., 2003; Donelick et al., 2005). The most common thing to do is to measure the D_{par}, which is an etch figure that appears if a fission track intersects the mineral surface. The size of maximum etch figures measured as D_{par}, parallel to the crystallographic c-axis, provides information about the chemical composition of the apatites; for example, it is assumed that apatites with short D_{par} anneal faster than apatites with long D_{par}. Short D_{par} are almost end-members of F-apatites, whereas long D_{par} are typical for Cl-apatite (e.g. Donelick et al., 2005). However, it is not suggested to take the D_{par} as a proxy for the Cl content, as the influencing parameter are not fully constrained, either, it is just a first approximation of that problem (e.g. Donelick et al., 2005). Measuring the D_{par} of analyzed apatite grains is commonly done during counting.

1.2.2 (U-Th-Sm)/He Dating

(U-Th-Sm)/He dating in its initial state was the first described geochronological dating method in the early 20th century (Rutherford, 1905). The method is based on the production of ^{4}He (α particle) as a result of the ^{235}U, ^{238}U, ^{232}Th and ^{147}Sm decay series, whose isotopes are all naturally incorporated in crystal lattices. The abundance of ^{4}He relative to the parent isotopes results in cooling ages, following the He ingrowth equation:

$$^4He = 8 \cdot ^{238}U(e^{\lambda_{238}t}-1)+7\cdot\frac{^{238}U}{137.88}(e^{\lambda_{235}t}-1)+6\cdot^{232}Th(e^{\lambda_{232}t}-1)+1\cdot^{147}Sm(e^{\lambda_{147}t}-1), \tag{1.3}$$

where t is the He age, ^4He,^{238}U,^{232}Th and ^{147}Sm are the measured present-day abundances of these isotopes, and $\lambda_{238}, \lambda_{235}, \lambda_{232}$ and λ_{147} are the corresponding decay constants. The factor 137.88 represents the present-day ^{238}U/^{235}U ratio. This equation excludes any extra sources of He (e.g. Wolf et al., 1998; Farley, 2002; Ehlers and Farley, 2003; Hourigan et al.,

2005).

In the beginning, the (U-Th-Sm)/He dating often provided inexplicable (too young) ages, which is a consequence of the diffusive lost of ^{4}He. However, since Zeitler et al. (1987) has discovered that the diffusion of ^{4}He occurs systematically at low temperatures, this method became a thermochronometer.

The diffusion of ^{4}He is very sensitive to temperature, which was demonstrated by diffusion experiments on apatites. The experiments revealed that ^{4}He diffuses until a temperature as low as 40°C (e.g. Wolf et al., 1996; Farley, 2000). Consequently, within the temperature range between 40°C and the effective closure temperature of AHe of 70 - 75°C, ^{4}He is either retained or diffused (e.g. Farley, 2000, 2002). According to the PAZ of the fission track thermochronometer, this temperature range is named the partial retention zone (PRZ). Therefore, AHe ages may constrain the cooling through very low temperatures, ~35°C lower than the AFT system (Wolf et al., 1998). In comparison, the closure temperature for zircon (U-Th-Sm)/He analysis varies between 190 - 200°C (e.g. Reiners, 2005), which is also lower than the analogous ZFT system.

Two factors may mainly bias the He measurement in minerals; undetected inclusions with a high U and Th concentration and/or He particles may be ejected from crystal surfaces (α-ejection). According to the first problem, it is very common that apatite grains contain of inclusions from minerals such as zircon and monazite. Both minerals are characterized by high U and Th concentrations. If, therefore, grains containing inclusions are not excluded prior the measurement, cooling ages will be strongly overestimated, because both minerals have contributed ^{4}He to the measured abundance in the grain. This can only be avoided by a very thorough selection of grains, but often the inclusions remain undiscovered and a careful interpretation of AHe ages is inevitable (e.g. Farley, 2002; Ehlers and Farley, 2003). More than one grain per sample is usually analysed to simplify the interpretation of AHe ages.

The second potential problem arises, because if α particles are produced, they are sufficiently energetic to travel up to 20 µm through the crystal lattice and thereby they may be ejected from crystal edges (Fig. 1.7). Accordingly, ejected particles from the surroundings of grains could also be implanted in other crystals, but this effect is neglected due to often common low U and Th concentrations in the host rocks of the minerals (e.g. Farley et al., 1996; Farley, 2002). However, the travel distance (stopping distance) from the α particles is long (20 µm) compared to the size of analyzed grains, which is the reason why the geometry of the grains is important for the determination of AHe ages (Farley et al., 1996; Farley, 2002; Meesters and Dunai, 2002*a*; Hourigan et al., 2005). The ejection effects, especially in small grains, may cause underestimated AHe ages (Farley et al., 1996), because of too many ejected particles. Thus, it is suggested to correct cooling ages for this effect (namely Ft correction). Nowadays, there exist various correction methods with different approaches,

(e.g. Farley et al., 1996; Farley, 2002; Meesters and Dunai, 2002*a*,*b*; Hourigan et al., 2005; Herman et al., 2007), but they all have in common that it is necessary to estimate the size and shape of grains before measuring the He ages, because the corrections are based on the surface-area-to-volume-ratio. The main difference between the methods is the assumed distribution of U and Th in the grains, if it is homogeneously or inhomogeneously distributed (zoning).

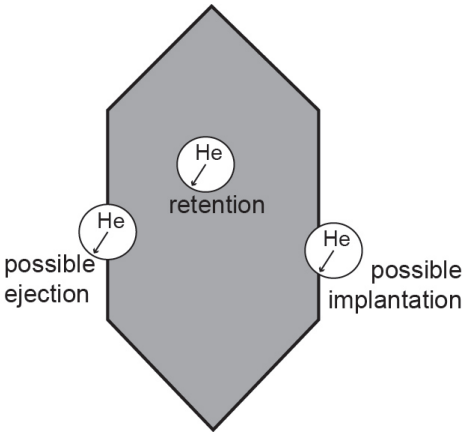

Figure 1.7: α (He) ejection in apatite grain, one particle will be retained, one might be ejected and one might be implanted from the surroundings, whereby the latter is only rare. It is conspicuous that especially the peripheral areas of the grain are affected by α ejection, why it is necessary to document size and shape of apatite grains prior the measurement. Sketch modified from Farley (2002).

1.3 Synopsis

This thesis is subdivided into three main chapters according to different methods and different objectives. The main chapters provide information about the topographic evolution of the Aar massif (Central Alps of Switzerland) since the Miocene, comprising a detailed reconstruction of the landscape evolution during glacials (Pleistocene) and interglacials (today).

Chapter 2 presents the exhumation history from the Aar massif beginning by the initial exhumation in the Miocene. New thermochronological data is compared to published data to figure out, how the exhumation proceeded. Thus, the exhumation history is discussed in therms of their influencing factors, tectonics or climate changes. The latter influences the erosional pattern, in which it affects the distribution and extent of glacial and fluvial erosion.

Chapter 3 focuses on the impact of accelerated glacial erosion on the exhumation pattern during the prominent Pleistocene glaciations. Accordingly, numerical models calculating the exhumation history based on a steady-state topography and on a pre-glacial topography, are compared to the thermochronological age dataset. The spatial distribution of glacial erosion in three Alpine valleys is constrained and consequences on the topographic evolution are quantified.

Chapter 4 describes the present distribution of erosion in an Alpine landscape, while differentiating between fluvial and glacial erosion. Denudation rates are measured based on the cosmogenic-produced ^{10}Be concentration in stream sediments, representing the mean denudation of the sample points' upstream catchment. In addition, provenance analyses of the stream sediments provide information about the spatial distribution of erosion in the present-day interglacial and constrain fluvial and glacial erosion. Note that the term denudation comprises the combined effects of physical erosion and chemical weathering and is usually used in this context (von Blanckenburg, 2005).

References

Barbarand, J., Carter, A., Wood, I. and Hurford, T. (2003), 'Compositional and structural control of fission-track annealing in apatite', *Chemical Geology* **198**(1-2), 107–137.

Bernet, M., Brandon, M., Garver, J., Balestieri, M. L., Ventura, B. and Zattin, M. (2009), 'Exhuming the Alps through time: Clues from detrital zircon fission-track thermochronology', *Basin Research* **21**(6), 781–798.

Bernet, M., Zattin, M., Garver, J. I., Brandon, M. T. and Vance, J. A. (2001), 'Steady-state exhumation of the European Alps', *Geology* **29**(1), 35.

Braun, J., van der Beek, P. and Batt, G. E. (2006), *Quantitative Thermochronology: Numerical Methods for the Interpretaion of Thermochronological Data*, Cambridge University Press, Cambridge.

Campani, M., Herman, F. and Mancktelow, N. (2010), 'Two- and three-dimensional thermal modeling of a low-angle detachment: Exhumation history of the Simplon Fault Zone, central Alps', *Journal of Geophysical Research* **115**(B10).

Cederbom, C. E., Sinclair, H. D., Schlunegger, F. and Rahn, M. K. (2004), 'Climate-induced rebound and exhumation of the European Alps', *Geology* **32**(8), 709.

Chew, D. M. and Donelick, R. A. (2012), Combined apatite fission track and U-Pb dating by LA-ICP-MS and its application in apatite provenance , *in* P. Sylvester, ed., 'Quantitative Mineralogy and Microanalysis of Sediments and Sedimentary Rocks', Mineralogical Association of Canada.

D'Agostino, N., Cheloni, D., Mantenuto, S., Selvaggi, G., Michelini, A. and Zuliani, D. (2005), 'Strain accumulation in the southern Alps (NE Italy) and deformation at the northeastern boundary of the Adria observed by CGPS measurements', *Geophysical Research Letters* **32**.

Delunel, R., van der Beek, P. A., Bourlès, D. L., Carcaillet, J. and Schlunegger, F. (2014), 'Transient sediment supply in a high-altitude Alpine environment evidenced through a 10 Be budget of the Etages catchment (French Western Alps)', *Earth Surface Processes and Landforms* **39**(7), 890–899.

Dodson, M. H. (1973), 'Closure temperature in cooling geochronological and petrological systems', *Contributions to Mineralogy and Petrology* **40**(3), 259–274.

Donelick, R. A., O'Sullivan, P. B. and Ketcham, R. A. (2005), 'Apatite Fission-Track Analysis', *Reviews in Mineralogy and Geochemistry* **58**, 49–94.

Ehlers, T. A. and Farley, K. A. (2003), 'Apatite (U–Th)/He thermochronometry: Methods and applications to problems in tectonic and surface processes', *Earth and Planetary Science Letters* **206**(1-2), 1–14.

England, P. and Molnar, P. (1990), 'Surface uplift, uplift of rocks, and exhumation of rocks', *Geology* **18**(12), 1173.

Farley, K. A. (2000), 'Helium diffusion from apatite: General behavior as illustrated by Durango fluorapatite', *Journal of Geophysical Research* **105**(B2), 2903.

Farley, K. A. (2002), '(U-Th)/He Dating: Techniques, Calibrations, and Applications', *Reviews in Mineralogy and Geochemistry* **47**(1), 819–844.

Farley, K. A., Wolf, R. A. and Silver, L. T. (1996), 'The effects of long alpha-stopping distances on (UTh)/He ages', *Geochimica et Cosmochimica Acta* **60**(21), 4223–4229.

Fleischer, R. L., Price, P. B. and Walker, R. M. (1965), 'Effects of temperature, pressure, and ionization of the formation and stability of fission tracks in minerals and glasses', *Journal of Geophysical Research* **70**(6), 1497–1502.

Fox, M., Leith, K., Bodin, T., Balco, G. and Shuster, D. L. (2015), 'Rate of fluvial incision in the Central Alps constrained through joint inversion of detrital 10Be and thermochronometric data', *Earth and Planetary Science Letters* **411**, 27–36.

Frisch, W. (1979), 'Tectonic progradation and plate tectonic evolution of the Alps', *Tectonophysics* **60**(3-4), 121–139.

Froitzheim, N. and Manatschal, G. (1996), 'Kinematics of Jurassic rifting, mantle exhumation, and passive-margin formation in the Austroalpine and Penninic nappes (eastern Switzerland)', *Geological Society of America Bulletin* **108**(9), 1120–1133.

Froitzheim, N., Schmid, S. M. and Conti, P. (1994), 'Repeated change from crustal shortening to orogen-parallel extension in the Austroalpine units of Graubünden', *Eclogae Geologicae Helvetiae* **87**(2), 559–612.

Galbraith, R. F. (2005), *Statistics for Fission Track Analysis*, Chapman and Hall, New York.

Galbraith, R. F. and Laslett, G. M. (1993), 'Statistical models for mixed fission track ages', *Nuclear Tracks and Radiation Measurements* **21**(4), 459–470.

Gallagher, K., Brown, R. and Johnson, C. (1998), 'Fission Track Analysis and its Applications to Geological Problems', *Annual Review of Earth and Planetary Sciences* **26**(1), 519–572.

Gleadow, A. J. W., Duddy, I. R., Green, P. F. and Lovering, J. F. (1986), 'Confined fission track lengths in apatite: a diagnostic tool for thermal history analysis', *Contributions to Mineralogy and Petrology* **94**(4), 405–415.

Glotzbach, C., Bernet, M. and van der Beek, P. (2011), 'Detrital thermochronology records changing source areas and steady exhumation in the Western European Alps', *Geology* **39**(3), 239–242.

Glotzbach, C., Reinecker, J., Danišík, M., Rahn, M., Frisch, W. and Spiegel, C. (2010), 'Thermal history of the central Gotthard and Aar massifs, European Alps: Evidence for steady state, long-term exhumation', *Journal of Geophysical Research* **115**(F3).

Glotzbach, C., van der Beek, P., Carcaillet, J. and Delunel, R. (2013), 'Deciphering the driving forces of erosion rates on millennial to million-year timescales in glacially impacted landscapes: An example from the Western Alps', *Journal of Geophysical Research: Earth Surface* **118**(3), 1491–1515.

Green, P., Duddy, I., Gleadow, A., Tingate, P. and Laslett, G. (1986), 'Thermal annealing of fission tracks in apatite', *Chemical Geology: Isotope Geoscience section* **59**, 237–253.

Green, P., Duddy, I., Laslett, G., Hegarty, K., Gleadow, A. and Lovering, J. (1989), 'Thermal annealing of fission tracks in apatite 4. Quantitative modelling techniques and extension to geological timescales', *Chemical Geology: Isotope Geoscience section* **79**(2), 155–182.

Grenerczy, G., Kenyeres, A. and Fejes, I. (2000), 'Present crustal movement and strain distribution in Central Europe inferred from GPS measurements', *Journal of Geophysical Research: Solid Earth* **105**(B9), 21835–21846.

Haeuselmann, P., Granger, D. E., Jeannin, P.-Y. and Lauritzen, S.-E. (2007), 'Abrupt glacial valley incision at 0.8 Ma dated from cave deposits in Switzerland', *Geology* **35**(2), 143–146.

Hasebe, N., Barbarand, J., Jarvis, K., Carter, A. and Hurford, A. J. (2004), 'Apatite fission-track chronometry using laser ablation ICP-MS', *Chemical Geology* **207**(3-4), 135–145.

Herman, F., Braun, J., Senden, T. J. and Dunlap, W. J. (2007), '(U–Th)/He thermochronometry: Mapping 3D geometry using micro-X-ray tomography and solving the associated production–diffusion equation', *Chemical Geology* **242**(1-2), 126–136.

Hourigan, J. K., Reiners, P. W. and Brandon, M. T. (2005), 'U-Th zonation-dependent alpha-ejection in (U-Th)/He chronometry', *Geochimica et Cosmochimica Acta* **69**(13), 3349–3365.

Hurford, A. J. (1990), 'International union of geological sciences subcommission on geochronology recommendation for the standardization of fission track dating calibration and data reporting', *International Journal of Radiation Applications and Instrumentation. Part D. Nuclear Tracks and Radiation Measurements* **17**(3), 233–236.

Hurford, A. J. and Green, P. F. (1982), 'A users' guide to fission track dating calibration', *Earth and Planetary Science Letters* **59**(2), 343–354.

Hurford, A. J. and Green, P. F. (1983), 'The zeta age calibration of fission-track dating', *Chemical Geology* **41**, 285–317.

Kuhlemann, J., Frisch, W., Székely, B., Dunkl, I. and Kázmér, M. (2002), 'Post-collisional sediment budget history of the Alps: tectonic versus climatic control', *International Journal of Earth Sciences* **91**(5), 818–837.

Labhart, T. P. (1977), *Aarmassiv und Gotthardmassiv*, Gebr. Borntraeger, Berlin.

Li, W., Lang, M., Gleadow, A. J., Zdorovets, M. V. and Ewing, R. C. (2012), 'Thermal annealing of unetched fission tracks in apatite', *Earth and Planetary Science Letters* **321-322**, 121–127.

Li, W., Wang, L., Lang, M., Trautmann, C. and Ewing, R. C. (2011), 'Thermal annealing mechanisms of latent fission tracks: Apatite vs. zircon', *Earth and Planetary Science Letters* **302**(1-2), 227–235.

Li, W., Wang, L., Sun, K., Lang, M., Trautmann, C. and Ewing, R. C. (2010), 'Porous fission fragment tracks in fluorapatite', *Physical Review B* **82**(14).

Mancktelow, N. S. (1992), 'Neogene lateral extension during convergence in the Central Alps: Evidence from interrelated faulting and backfolding around the Simplonpass (Switzerland)', *Tectonophysics* **215**(3-4), 295–317.

Marquer, D. and Burkhard, M. (1992), 'Fluid circulation, progressive deformation and mass-transfer processes in the upper crust: the example of basement-cover relationships in the External Crystalline Massifs, Switzerland', *Journal of Structural Geology* **14**(8/9), 1047–1057.

McDougall, I. and Harrison, T. M. (1999), *Geochronology and Thermochronology by the 40Ar/39Ar Method*, Oxford University Press, New York.

Meesters, A. and Dunai, T. (2002*a*), 'Solving the production–diffusion equation for finite diffusion domains of various shapes: Part I. Implications for low-temperature (U–Th)/He thermochronology', *Chemical Geology* **186**(3-4), 333–344.

Meesters, A. and Dunai, T. J. (2002*b*), 'Solving the production–diffusion equation for finite diffusion domains of various shapes: Part II. Application to cases with a-ejection and nonhomogeneous distribution of the source', *Chemical Geology* **186**(3-4), 347–363.

Michalski, I. and Soom, M. (1990), 'The Alpine thermo-tectonic evolution of the Aar and Gotthard massifs, Central Switzerland: fission track ages on zircon and apatite and K-Ar mica ages', *Schweiz. Mineral. Petrogr. Mitt.* (70), 373–387.

Naeser, C. W. (1979), 'Fission-Track Dating and Geologic Annealing of Fission Tracks', *Isotope Geology* pp. 154–169.

Nocquet, J.-M. (2012), 'Present-day kinematics of the Mediterranean: A comprehensive overview of GPS results', *Tectonophysics* **579**, 220–242.

Rahn, M. K., Brandon, M. T., Batt, G. E. and Garver, J. I. (2004), 'A zero-damage model for fission-track annealing in zircon', *American Mineralogist* **89**(4), 473–484.

Reiners, P. W. (2005), 'Past, Present, and Future of Thermochronology', *Reviews in Mineralogy and Geochemistry* **58**(1), 1–18.

Rutherford, E. (1905), 'Present problems in radioactivity', *Pop. Sci. Monthly* **May**, 1–34.

Schlatter, A., Schneider, D., Geiger, A. and Kahle, H.-G. (2005), 'Recent vertical movements from precise levelling in the vicinity of the city of Basel, Switzerland', *International Journal of Earth Sciences* **94**(4), 507–514.

Schmid, S. M., Fügenschuh, B., Kissling, E. and Schuster, R. (2004), 'Tectonic map and overall architecture of the Alpine orogen', *Eclogae Geologicae Helvetiae* **97**(1), 93–117.

Schmid, S. M., Pfiffner O. A., Froitzheim N., Schönborn G. and Kissling E. (1996), 'Geophysical - geological transect and tectonic evolution of the Swiss-Italian Alps', *Tectonics* **15**, 1036–1064.

Seward, D. and Mancktelow, N. S. (1994), 'Neogene kinematics of the central and western Alps: Evidence from fission-track dating', *Geology* **22**(9), 803.

Spotila, J. A. (2005), 'Applications of Low-Temperature Thermochronometry to Quantification of Recent Exhumation in Mountain Belts', *Reviews in Mineralogy and Geochemistry* **58**(1), 449–466.

Steck, A. and Hunziker, J. (1994), 'The Tertiary structural and thermal evolution of the Central Alps—compressional and extensional structures in an orogenic belt', *Tectonophysics* **238**(1-4), 229–254.

Tagami, T., Carter, A. and Hurford, A. J. (1996), 'Natural long-term annealing of the zircon fission-track system in Vienna Basin deep borehole samples: Constraints upon the partial annealing zone and closure temperature', *Chemical Geology* **130**(1-2), 147–157.

Tagami, T. and O'Sullivan, P. B. (2005), 'Fundamentals of Fission-Track Thermochronology', *Reviews in Mineralogy and Geochemistry* **58**(1), 19–47.

Valla, P. G., Shuster, D. L. and van der Beek, P. A. (2011), 'Significant increase in relief of the European Alps during mid-Pleistocene glaciations', *Nature Geoscience* **4**(10), 688–692.

Vernon, A. J., van der Beek, P. A. and Sinclair, H. D. (2009), 'Spatial correlation between long-term exhumation rates and present-day forcing parameters in the western European Alps', *Geology* **37**(9), 859–862.

Vernon, A., van der Beek, P., Sinclair, H. and Rahn, M. (2008), 'Increase in late Neogene denudation of the European Alps confirmed by analysis of a fission-track thermochronology database', *Earth and Planetary Science Letters* **270**(3-4), 316–329.

von Blanckenburg, F. (2005), 'The control mechanisms of erosion and weathering at basin scale from cosmogenic nuclides in river sediment', *Earth and Planetary Science Letters* **237**(3-4), 462–479.

Wagner, G. and van den Haute, P. (1992), *Fission-track Dating*, Kluwer, Dordrecht.

Willett, S. D. (1999), 'Orogeny and orography: The effects of erosion on the structure of mountain belts', *Journal of Geophysical Research* **104**(B12), 28957.

Willett, S. D. and Brandon, M. T. (2002), 'On steady states in mountain belts', *Geology* **30**(2), 175.

Willett, S. D., Schlunegger, F. and Picotti, V. (2006), 'Messinian climate change and erosional destruction of the central European Alps', *Geology* **34**(8), 613.

Wolf, R., Farley, K. and Kass, D. (1998), 'Modeling of the temperature sensitivity of the apatite (U–Th)/He thermochronometer', *Chemical Geology* **148**(1-2), 105–114.

Wolf, R., Farley, K. and Silver, L. (1996), 'Helium diffusion and low-temperature thermochronometry of apatite', *Geochimica et Cosmochimica Acta* **60**(21), 4231–4240.

Wortmann, U. G., Weissert, H., Funk, H. and Hauck, J. (2001), 'Alpine plate kinematics revisited: The Adria Problem', *Tectonics* **20**(1), 134–147.

Zeitler, P. K., Herczeg, A. L., McDougall, I. and Honda, M. (1987), 'U-Th-He dating of apatite: A potential thermochronometer', *Geochimica et Cosmochimica Acta* **51**(10), 2865–2868.

2 Exhumation history of the Aar massif

2.1 Abstract

The reconstruction of the exhumation history of the Central European Alps led to different interpretations. Exhumation history models range from long-term uniform exhumation to one or two phases of accelerated exhumation. Three different thermochronometers are combined to reproduce the exhumation history of the external Aar massif, which is located in Switzerland (Central Alps). The zircon (ZFT) and apatite (AFT) fission track ages as well as apatite (U-Th-Sm)/He (AHe) ages are used to model the thermal history in a high-relief topography. The oldest cooling ages reveal a localized initial cooling during the onset of collision between the Adriatic indenter and the European continent at 27 - 19 Ma. However, the widespread incidence of similar ZFT ages suggests rapid cooling in the whole Aar massif that was caused by the main exhumation of the massif between 17 - 12 Ma, similar to other external massifs in the Western Alps. Since ~8 Ma, the massif has been exhumed with a steady-state exhumation of 0.5 km/Ma. The modelled thermal history does not show any exhumation pulses until the Pleistocene, but rather strongly elevation-dependent accelerated cooling. This is assumed to be a consequence of a perturbation of near surface isotherms below a high-relief topography, which caused a different timing and pace of cooling at steady-state exhumation. Nevertheless, the extensive glaciations during the Pleistocene led to high valley incision rates that can be reconstructed by an increased occurrence of young AFT and AHe ages in valleys. The relief development can also be observed in time-Temperature paths that reveal rapid cooling within the last 2 Ma, at which the impact on the thermal history may be intensified by perturbed near surface isotherms.

2.2 Introduction

The European Alps and in particular the external massifs of the Central and Western Alps have long been in focus of thermochronological studies to investigate the roles of tectonics and climate on the long-term exhumation (e.g. Michalski and Soom, 1990; Reinecker et al., 2008; Vernon et al., 2008, 2009a; Glotzbach et al., 2010, 2011a; Valla et al., 2011a, 2012). However, the outcome of these studies seems inconsistent; predicted exhumation histories of the external massifs differ strongly. Several distinct exhumational pulses were identified that have led to the exposure of the external massifs as one of the last parts during Alpine orogeny.

This study focuses on the Aar massif, which is an external massif within the Central Alps in Switzerland. Previous studies analysed surface and tunnel bedrock samples within the same massif propose either one or two phases of accelerated exhumation since ~12 – 10 Ma; suggested exhumation pulses range between 10 – 7 Ma, between 5 – 3 Ma and/or within the last ~2 - 1 Ma (e.g. Michalski and Soom, 1990; Reinecker et al., 2008; Vernon et al., 2008, 2009a; Glotzbach et al., 2010; Valla et al., 2011a, 2012). Furthermore, based on data from the Mont Blanc and Ecrins-Pelvoux massifs in the Western Alps, rapid exhumation until ~6 - 5 Ma followed by moderate exhumation is identified that concludes with an increase of exhumation rates during the last ~2 Ma (e.g. Glotzbach et al., 2008; van der Beek et al., 2010; Glotzbach et al., 2011a). Detrital thermochronological records from foreland, river and synorogenic sediment samples, however, indicate uniform exhumation rates in the Central and Western Alps since 15 and 10 Ma, respectively (e.g. Bernet et al., 2001; Glotzbach et al., 2011b).

Consequently, the question arises, why the detrital record differs from the identified exhumation histories based on bedrock thermochronological data. Additionally, if the massif was undergone by distinct exhumation pulses, how many pulses would have taken place and which forces would have triggered them.

The youngest increase of exhumation rates ($\leq$2 Ma), which was also observed at other places (Herman et al., 2013), is assigned to effective glacial erosion during the prominent glaciations in the Quaternary. The glacial erosion led to relief growth through glacial valley carving (e.g. Haeuselmann et al., 2007; Glotzbach et al., 2008; Reinecker et al., 2008; Glotzbach et al., 2011a; Valla et al., 2011a, 2012). Moreover, a lack of correlation between recent released seismic energy and long-term exhumation rates exclude active tectonics as a short-term influencing factor on the exhumation pattern (Vernon et al., 2009b). On the contrary, the other two exhumation pulses (10 – 7 Ma and 5 – 3 Ma) have not been fully understood yet. Possible explanations range from localized rock uplift due to tectonic activity to changes in the precipitation pattern, because of climate changes (e.g. Schmid et al., 1996; Kuhlemann

et al., 2002; Cederbom et al., 2004, 2011; Willett et al., 2006). Kuhlemann et al. (2002) detected an increasing sediment flux from the inner Alps towards the outer regions at ~5 Ma, which Willett et al. (2006) explained by a transition towards wetter climate conditions within the last phase of the Messinian salinity crisis. According to that, thermochronological investigations about the North Alpine foreland basin reveal intensified erosion of the Molasse basin in the late Miocene and again in the Pleistocene, whereby the latter is also assigned to accelerated erosion caused by glaciations. The Late Miocene erosion pulse, however, is also assumed to be climatically induced (Cederbom et al., 2004, 2011), supporting Willett et al. (2006). On the contrary, studies from von Hagke et al. (2012, 2014) about the Subalpine Molasse basin suggest that any movements in the foreland basin are related to active tectonics rather than climatic oscillations. The Subalpine foreland basin is kinematically linked to the external massifs in the Central Alps due to the pro-wedge geometry formed above the subducting European plate. It is generally assumed that the Alpine convergence rates have decreased since Miocene, which probably led to decreasing rock uplift rates (e.g. Schmid et al., 1996).

In this study, new thermochronological data of three different thermochronometers (zircon and apatite fission track, and (U-Th-Sm)/He dating on apatites) from the middle Aar massif (48 km x 32 km, Fig. 2.1A) are used to trace the exhumation history of the external massif. The new dataset is interpreted together with samples from previous studies (e.g Michalski and Soom, 1990; Reinecker et al., 2008; Vernon et al., 2008, 2009a; Glotzbach et al., 2010). The dense spatial distribution of thermochronological ages is used to reconstruct the (not yet fully understood) exhumation history (e.g. Michalski and Soom, 1990; Reinecker et al., 2008; Vernon et al., 2008, 2009a; Glotzbach et al., 2010; Valla et al., 2011a, 2012), as well as the triggering factors (tectonics vs. climate). For this purpose, standard interpretation techniques for thermochronological data are used: for example, age-elevation relationships as well as thermal history modelling based on fission track length distributions.

2.3 Geological setting

The Alps are the result of convergence between the European continent and the Adriatic micro-continent, which caused nappe stacking, crustal thickening and finally tectonic uplift since the Eocene (e.g. Schmid et al., 1996). Nowadays, the European Alps are divided into three major tectonic units (Helvetic, Penninic, and Austroalpine and South Alpine units) corresponding to their Upper Cretaceous paleogeographic position. The Helvetic and Austroalpine - South Alpine units represent continental units of the European and Adriatic plates, respectively. The Penninic unit mainly comprises oceanic rocks of the Valais and Piedmont-Liguria oceanic basins and the sedimentary cover of the Briançonnais microcontinent, which is assumed to have been separated from the former European margin in the Early Cretaceous (e.g. Schmid et al., 1996, 2004). During orogeny, as a consequence of the collision of the European continent and the Adriatic micro-plate, the three units were thrust northwards, contemporaneously to an anticlockwise rotation of the Adriatic micro-plate (e.g. Steck and Hunziker, 1994; Schmid et al., 2004).

The study area is part of the Helvetic domain, which comprises in addition to the sediments from the distal part of the former European continental margin, crystalline basement rocks from the European continent. These are outcropping as individual massifs in the external part of the Alps, e.g. Mont Blanc massif, Belledonne massif and Aar massif (e.g. Schmid et al., 2004). This study is focused on the Aar massif, which is surrounded by Helvetic nappes that mainly consist of limestone (Fig. 2.1). The southern border of the Aar massif and accordingly the Helvetic domain is constrained by the Penninic frontal thrust, at which in Early Miocene (~20 Ma) Penninic nappes were thrust onto Helvetic nappes (Schmid and Kissling, 2000). This thrust was probably active between 25 - 17 Ma with maximum movement in the Early Miocene (Schmid and Kissling, 2000; Pleuger et al., 2012).

Due to the north-directed convergence; the sediments forming the Helvetic nappes were thrust towards the north. After the emplacement of the Helvetic nappes, thrusting of the Aar massif caused subsequent doming and, finally, led to the exhumation of the massif. Doming of the crystalline basement rocks between Miocene and Pliocene (20 - 5 Ma) caused a bending of the Helvetic thrust (northern border of the Aar massif, Fig. 2.1) (Herwegh and Pfiffner, 2005) and an overthrusting of the autochthonous sedimentary cover of the crystalline rocks onto the Helvetic nappes (Fig. 2.1B) (e.g. Labhart, 1977; Schmid et al., 1996). Consequently, the crystalline basement was imbricated and steepened and dips between 20-45° below the Helvetic sediments to the northwest (e.g. Labhart, 1977). The imbrications and the thrusting of the Aar massif were active simultaneously and therefore built an antiformal stack, which resulted in very steep structures at the northern border of the massif (e.g. Herwegh and Pfiffner, 2005). Both major fault structures surrounding the Aar massif, Helvetic

and Penninic frontal thrust are supposed to have been inactive since ~17 Ma (Pleuger et al., 2012). Due to the lack of sediments derived from the crystalline basement in the Molasse basin (e.g. Trümpy, 1980), an overall exhumation of the crystalline Aar massif might have only taken place within the last 10 Ma (Late Miocene – Pliocene).

The crystalline Aar massif comprises two units; the Variscan basement and the Aar granite (Fig. 2.1), of which the latter consists of late Variscan subalkaline intrusive bodies with an age of 298 Ma (e.g. Quadt and Schaltegger, 1990). The Variscan basement unit comprises metasediments, anatectic migmatites, metasedimentary and granitic gneisses, and volcanoclastic sediments of mainly Variscan age and minor pre-Variscan age (e.g. Albrecht, 1994). At the latest, during Variscan orogeny the crystalline zone of the Aar massif was metamorphosed to amphibolite facies; however, during Alpine orogeny, the Aar massif has been only metamorphosed up to greenschist facies (peak metamorphism between 35 – 30 Ma) with increasing metamorphic grade from north to south (Marquer and Burkhard, 1992; Albrecht, 1994; Herwegh and Pfiffner, 2005).

Vernon et al. (2009a) and Glotzbach et al. (2010) suggest fairly constant long-term exhumation rates of ~0.3 – 0.7 km/Ma throughout the late Neogene with a potential acceleration during the late Pliocene. Nevertheless, presumably increasing climatically controlled erosion may have been balanced by decreasing tectonic activity (e.g. Reinecker et al., 2008; Glotzbach et al., 2010). Since late Neogene, the convergence between the European continent and Adriatic micro-plate has decreased (e.g. Schmid et al., 1996), which is supported by present-day GPS data of the Central Alps (e.g. Calais et al., 2002; Nocquet, 2012). Therefore, recent rock uplift rates from repeated precise levelling across the Aar massif that range between 0.5 – 1 mm/a from north to south (e.g. Schlatter et al., 2005), are assumed to be independent of active tectonic movements. Recent rock uplift roughly correlates with Holocene erosion rates derived from cosmogenic nulicde measurements on stream sediments (e.g. Wittmann et al., 2007; Champagnac et al., 2009).

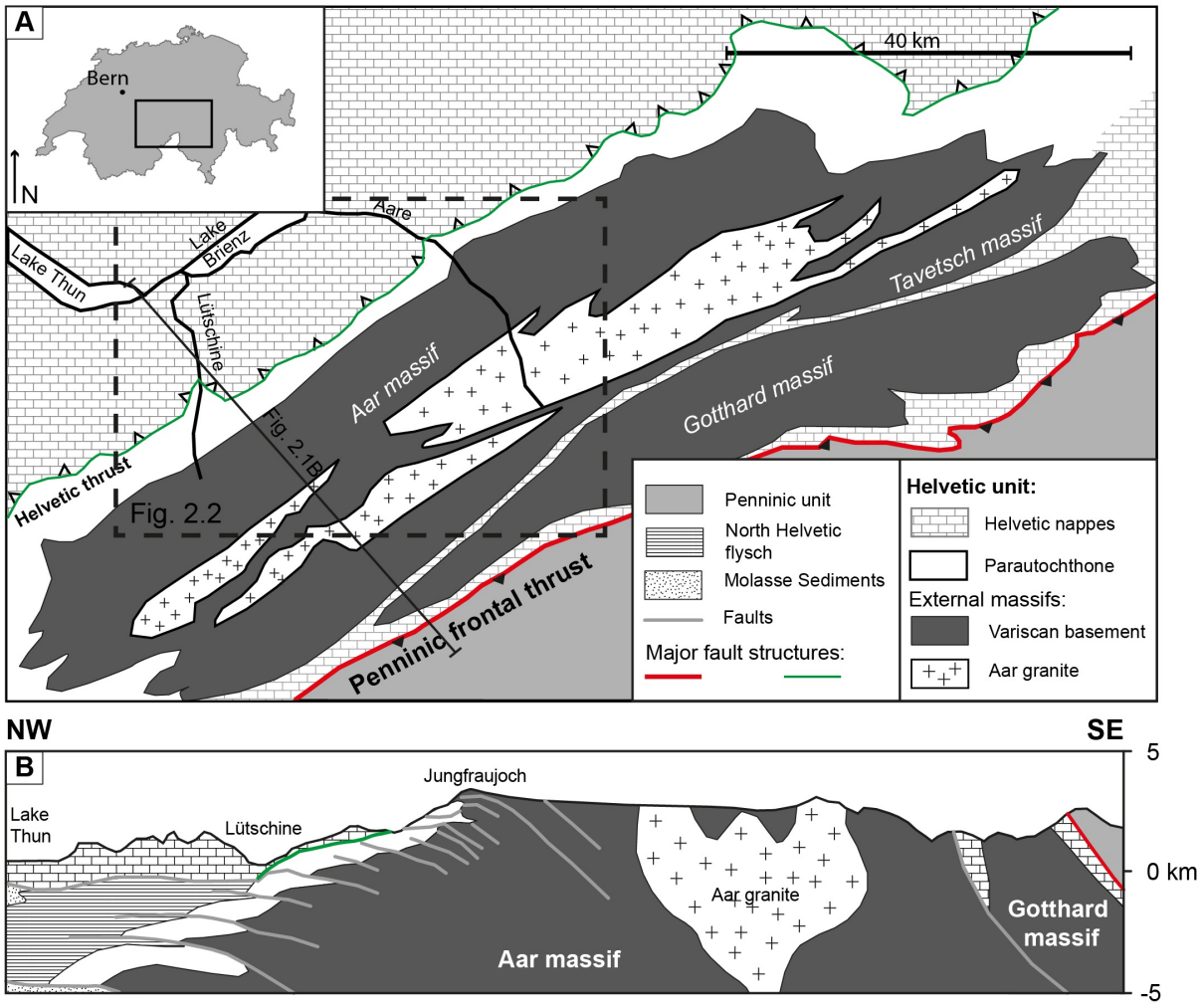

Figure 2.1: **(A)** Simplified and modified geological map of the study area based on the Tectonic map of Switzerland 1:500 000. **(B)** Simplified cross section through the study area modified from Hänni and Pfiffner (2001).

2.4 Methods

In this study we applied low-temperature thermochronology on apatites and zircons from bedrocks outcropping in the crystalline zone of the Aar massif (Fig. 2.2). The thermochronogical data derived from 34 samples from this study (Tab. 2.1) are combined with 35 already analysed samples from Michalski and Soom (1990); Vernon et al. (2009a) and M. Rahn (unpublished data), which are located within or close by the study area (Fig. 2.2). The apatites and zircons were separated from the bedrock samples using standard mineral preparation methods; crushing and sieving to a grain size fraction $<$500 µm is followed by magnetic and heavy liquid (LST-Fastfloat and diiodmethane) separations.

Thermochronology is based on the concept of closure temperature that represents a temperature range above which traces of radioactive decay in minerals are erased as fast as they are formed, whereas below, traces of radioactive decay are accumulated (Dodson, 1973). Accordingly, the thermochronological age may ideally represent the age since the mineral has left the closure temperature range, while it was brought rapidly and uniformly to the surface by exhumation (e.g. Wagner, 1968). In this study, three different thermochronological methods are combined; fission track dating on apatites (AFT) and zircons (ZFT) and (U-Th-Sm)/He analyses on apatites (AHe).

Fission track dating is based on the accumulation of fission tracks, which are continuously produced by spontaneous fission of ^{238}U in apatites and zircons (Wagner, 1968). Nevertheless, fission tracks can anneal in response to temperature and time, and the temperature window (PAZ – partial annealing zone) in which tracks may anneal ranges between 60 – 120°C for apatites and between 190 – 380°C for zircons (e.g. Wagner and van den Haute, 1992; Rahn et al., 2004; Ketcham et al., 2007).

The AHe method is based on the measurement of ^{4}He (α particles) in apatites, which is the decay product from the radioactive decay of uranium (^{238}U, ^{235}U), thorium (^{232}Th) and samarium (^{147}Sm). The particles are retained within the crystals and the measured amount of ^{4}He relative to the parent isotope provides a thermochronological age. However, the α particles can only be accumulated below ~70-75°C, at higher temperatures diffusion removes the ^{4}He as fast as it is generated (e.g. Zeitler et al., 1987; Farley, 2000, 2002; Ehlers and Farley, 2003). Hence, the AHe age represents the time since cooling below ~70-75°C (Green et al., 1986; Gallagher et al., 1998; Farley, 2000). According to the PAZ at which fission tracks may anneal, there is also a sensitive temperature range at which ^{4}He may partially diffused or retained (PRZ – partial retention zone) varying between 40 – 85°C (Wolf et al., 1996; Gallagher et al., 1998; Farley, 2000; Ehlers and Farley, 2003; Reiners and Brandon, 2006).

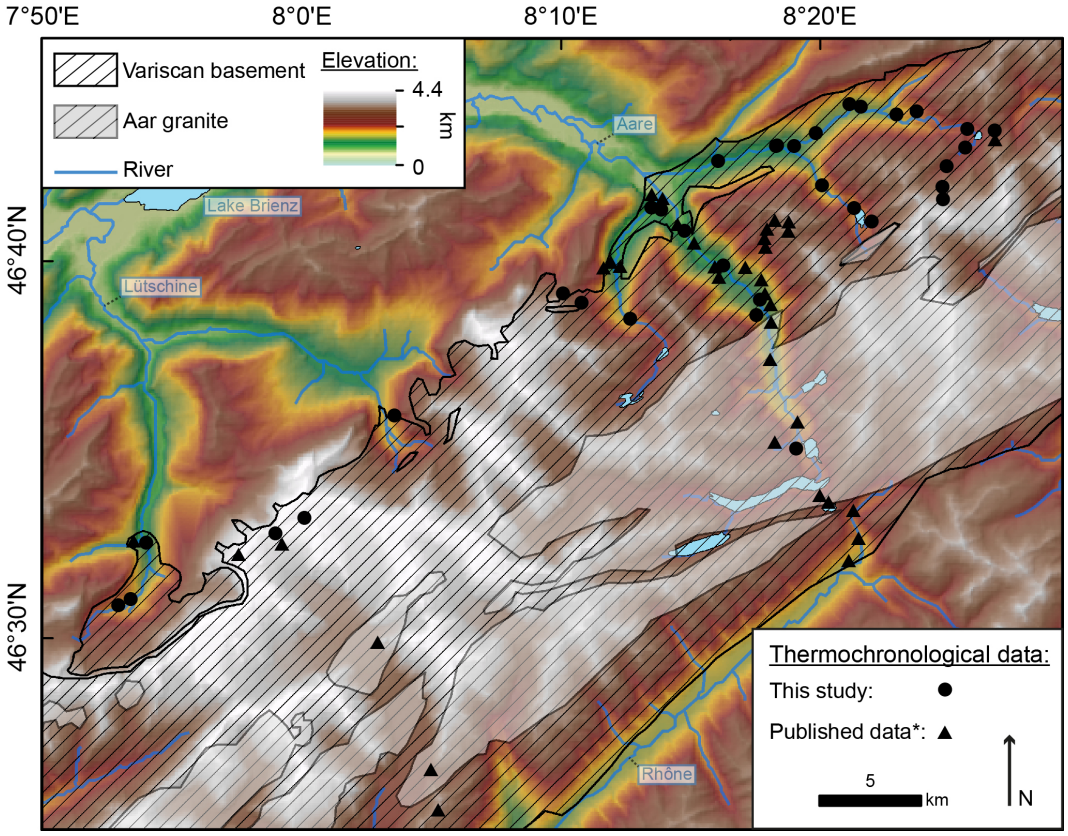

Figure 2.2: Topographic overview of sample locations based on SRTM data with 90 m resolution (NASA,2006). *Published data from: Michalski and Soom (1990); Vernon et al. (2009a) and M. Rahn (unpublished data)

Table 2.1: Sample Locations

Sample	Longitude	Latitude	Elevation (m)	Geological Unit	Lithology
CGP223	7.90417	46.54278	936	Variscan basement	Orthogneiss
CGP227	8.26849	46.71457	896	Variscan basement	Orthogneiss
CGP230	8.30568	46.72138	941	Variscan basement	Orthogneiss
CGP231	8.44643	46.72890	2234	Variscan basement	Orthogneiss
CGP232	8.42855	46.72965	1883	Variscan basement	Orthogneiss
CGP233	8.39581	46.73720	1614	Variscan basement	Granitic Gneiss
CGP234	8.38303	46.73571	1365	Variscan basement	Granitic Gneiss
CGP235	8.29619	46.65344	1093	Variscan basement	Biotite-Plagioclase Gneiss
CGP236	8.26968	46.66731	908	Variscan basement	Orthogneiss
CGP238	8.16959	46.65522	2664	Variscan basement	Granitic Gneiss
CGP239	8.18167	46.65139	2117	Variscan basement	Granitic Gneiss
CGP240	8.21279	46.64447	1448	Variscan basement	Granitic Gneiss
CGP241	8.22569	46.69368	793	Variscan basement	Granitic Gneiss
CW1	8.41333	46.70139	2778	Variscan basement	Orthogneiss
CW2	8.41278	46.70389	2571	Variscan basement	Orthogneiss
CW4	8.41556	46.71306	2078	Variscan basement	Orthogneiss
CW5	8.42722	46.72139	2025	Variscan basement	Orthogneiss
CW12	8.00556	46.55472	3660	Variscan basement	Orthogneiss
CW13	7.98694	46.54778	3495	Variscan basement	Orthogneiss
CW15	8.36750	46.68833	2090	Variscan basement	Biotite Orthogneiss
CW16	8.35611	46.69417	1755	Variscan basement	Biotite Orthogneiss
CW17	8.33556	46.70417	1386	Variscan basement	Biotite Orthogneiss
CW20	7.88674	46.51495	1600	Variscan basement	Granitic Gneiss
CW21	7.89478	46.51777	1379	Variscan basement	Granitic Gneiss
CW31	8.06222	46.60056	1750	Variscan basement	Orthogneiss
CW36	8.32028	46.58778	1804	Aar granite	Biotite Granite
CW40	8.35999	46.73912	1216	Variscan basement	Granitic Gneiss
CW41	8.35264	46.74028	1220	Variscan basement	Granitic Gneiss
CW42	8.33105	46.72730	1130	Variscan basement	Granitic Gneiss
CW43	8.31709	46.72134	1025	Variscan basement	Granitic Gneiss
CW44	8.30618	46.72172	940	Variscan basement	Granitic Gneiss
CW48	8.29665	46.64937	1140	Variscan basement	Biotite Orthogneiss
CW49	8.24716	46.68366	780	Variscan basement	Granitic Gneiss
CW50	8.22794	46.69282	850	Variscan basement	Orthogneiss

2.4.1 Fission track dating

In preparation for fission track dating, the apatites were embedded in araldite2020 resin and zircons in PFA Teflon^{TM}. Polished apatites were etched for 20s at 20°C with 5M HNO_3, whereas polished zircon mounts were etched with an eutectic melt of KOH-NaOH at ~220°C, following Zaun and Wagner (1985). Two zircon mounts per sample were prepared to account for inter-sample differences in etching efficiencies (e.g. Naeser et al., 1987). After irradiation with thermal neutrons at the FRM-II reactor facility in Garching (TU München), the mica external detectors of apatites and zircons were etched to reveal induced tracks using 40% HF at 20°C for 30 min.

The fission track counting on ca. 20 grains per sample was carried out using an Olympus BX51 microscope and dry objectives. The dating is based on the external detector method (Naeser, 1967; Gleadow, 1981) and the zeta calibration approach (Hurford and Green, 1982, 1983). AFT and ZFT ages were calculated using Trackkey 4.2g (Dunkl, 2002) and are provided with a central age and corresponding 1σ errors (Tab. 2.2 and 2.3) (Galbraith and Laslett, 1993).

Both, AFT and ZFT samples were used to measure confined track lengths in samples with a statistically relevant amount of measurable lengths (Tab.2.2 and 2.3). Track length distributions provide details about the thermal evolution of samples, such as fast or slow cooling or even reheating (e.g. Tagami et al., 1996; Gallagher et al., 1998).

2.4.2 (U-Th-Sm)/He dating

AHe dating was applied on two to five single-crystal replicates per sample (Tab. 2.5). Suitable grains were hand-picked under a stereo microscope by selecting grains of an appropriate size and morphology without any visible inclusions, following Farley (2002). In this study, the increased presence of inclusions was a limiting factor for choosing more samples for AHe analyses. Length and width of selected crystals were measured to correct raw ages for their α ejection (Ft correction) after Farley et al. (1996) and Hourigan et al. (2005). Before packing into Pt foil tubes, crystals were digitally photographed. The AHe measurement was performed at the GÖochronology laboratory at the University of Göttingen, whereby the He was extracted from the crystals by heating the encapsulated grains in vacuum with an IR laser at a temperature of ~900°C. Before the ^{4}He content was measured by a Hiden Hal-3F/PIC triple-filter quadrupole mass spectrometer, the gas was purified with an SAES Ti-Zr getter. The apatites were then dissolved in 2% ultrapure HNO_3 (+0.05% HF) in an ultrasonic bath and spiked with calibrated ^{233}U and ^{230}Th solutions to measure the elements U, Th and Sm. Measurements of the isotope concentrations were performed with inductively coupled

plasma mass spectrometry (ICP-MS) using the isotope dilution method with a Perkin Elmer Elan DRC II system equipped with an APEX micro-flow nebulizer.

2.4.3 Thermal modelling

AFT track length distributions were used to model time-temperature histories (tT-model) (Fig. 2.9) in HeFTy v.1.8.3 (Ketcham, 2005), using the AFT annealing model from Ketcham et al. (2007) and available ZFT ages as high temperature constraints. If there is no corresponding ZFT age available or the corresponding ZFT age is of Pre-Alpine age (CGP241), the constrain box will be placed at ~12 Ma and in the temperature range of the ZFT PAZ. 12 Ma is a prevailing ZFT age in the Aar massif as confirmed by a previously published study (Michalski and Soom, 1990). ZFT track length distributions were added to two tT-models (CGP234 and 236) using an annealing model from Rahn et al. (2004). Due to conflicting AFT and AHe ages, it was only possible to add corresponding AHe data to the tT-model of sample CW15. The AHe data were calibrated to the radiation model by Flowers et al. (2009). Each model is based on c-axis projected track lengths and ends at a fixed recent mean surface temperature of ~7°C.

2.5 Results

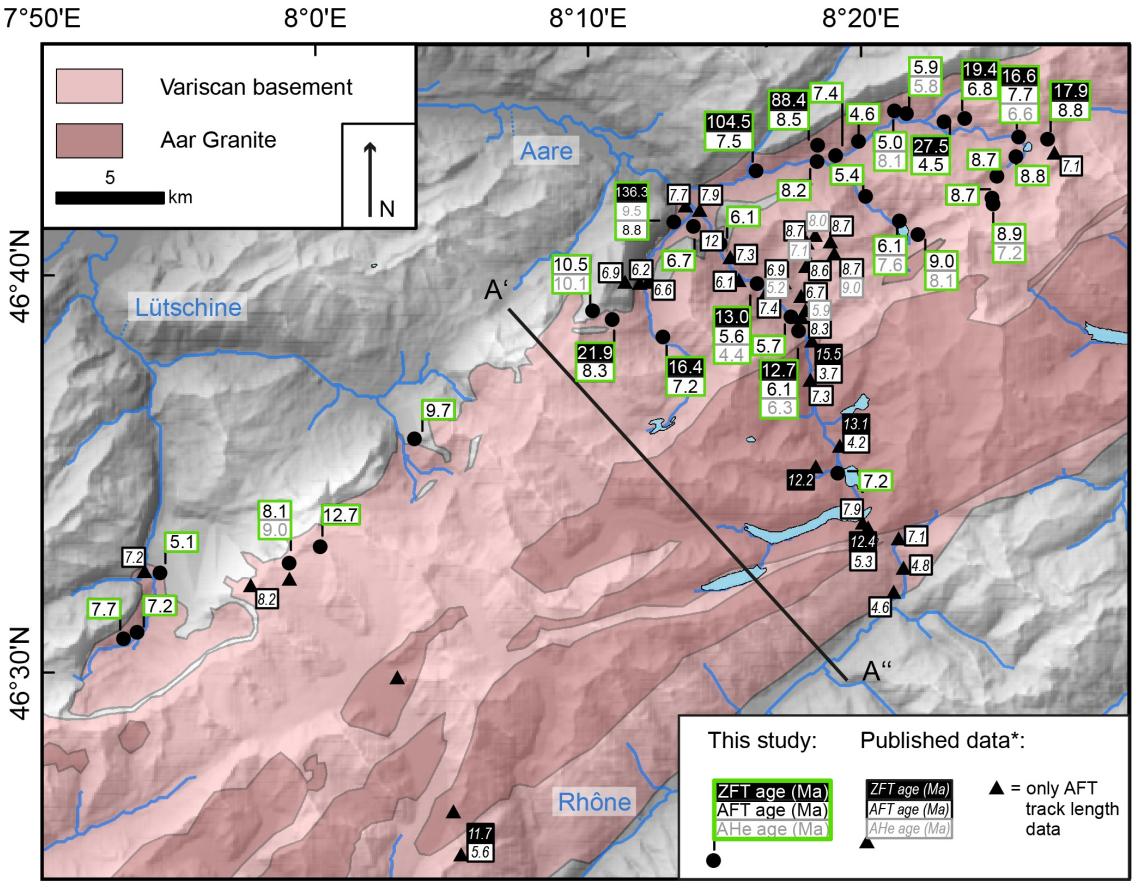

Figure 2.3: Sample locations and corresponding ZFT, AFT and AHe ages overlain on a shaded relief map and simplified geology from the crystalline part of the Aar massif (SRTM data from NASA (2006) with 90m resolution). *Published data derives from Michalski and Soom (1990); Vernon et al. (2008, 2009a) and unpublished ages from M. Rahn.

2.5.1 ZFT ages

11 counted ZFT ages range from 136.3 ± 11.9 to 12.7 ± 0.8 Ma (Tab. 2.2 and Fig. 2.3). There are major age discrepancies in the ZFT age pattern; most of the ages are between 12 to 27 Ma old and three are between 88 to 136 Ma old. Three samples (CGP230, CGP231 and 234) did not pass the chi-square (X^2) test above the 5% limit (Galbraith, 2005). Decomposing these three mixed grain ages reveal two individual grain age populations that represent at least between 7 and 27% of the measured single ages (Tab. 2.3). Exactly the same age range is covered by six ZFT ages by Michalski and Soom (1990) with most of the ages between 12 and 16 Ma and one sample yielding a ZFT age of 100 Ma (KAW 2207, 2208, 2213, 2219, 2408, 2761). However, the spatial distribution of ZFT ages along the NW-SE transect (Fig.

2.4A) demonstrates that old pre-Alpine ZFT ages (>35 Ma) are concentrated on the very northwestern boundary of the Aar massif, directly followed by ZFT ages ~20 Ma and slightly decreasing ages down to 12 Ma towards the southeast.
Corresponding ZFT track lengths are ~10.7 µm (Fig. 2.5, Tab. 2.2 and Fig. 2.10 in the Appendix), suggesting overall fast cooling through the ZFT PAZ since ~27 Ma. Sample CGP41 (ZFT age of ~136 Ma) yields in mean track lengths of <7 µm indicating that the sample was not completely reset during Alpine orogeny.

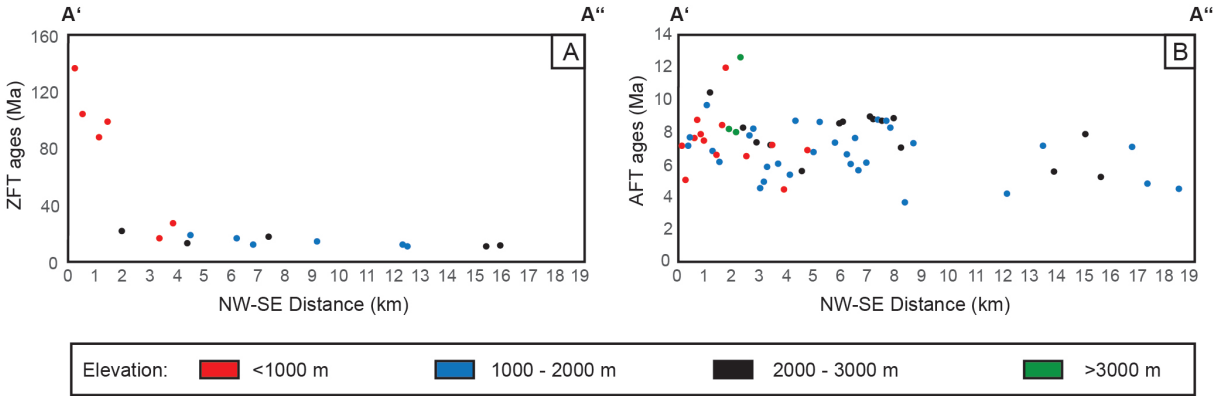

Figure 2.4: (A) ZFT ages from this study and (samples from Fig. 2.3) projected on a NW-SE average transect; relative location of profile is shown in Fig. 2.3. Published ages are from Michalski and Soom (1990) **(B)** AFT ages projected along the same NW-SE transect as depicted in Fig. 2.4A. Published data derived from Michalski and Soom (1990); Vernon et al. (2008, 2009a) and unpublished ages from M. Rahn

Table 2.2: Zircon fission track results

Sample	# grains	ρs	Ns	ρi	Ni	ρd	Nd	P(χ^2) [%]	Central age ± 1σ [Ma]	U [ppm]	Confined track lengths	
											# Length	MTL ± SD (µm)
CGP227	20	195.67	1311	37.463	251	3.707	2426	7	**104.5±9.3**	445		
CGP230	20	105.40	1328	23.968	302	3.706	2426	0	**88.4±6.5**	353		
CGP231	20	26.97	526	30.513	595	3.704	2426	1	**17.9±1.4**	363		
CGP232	20	22.09	517	26.88	629	3.704	2426	85	**16.6±1.2**	324		
CGP233	20	18.00	405	18.667	420	3.703	2426	6	**19.4±1.9**	230		
CGP234	20	41.77	330	28.734	227	3.701	2426	0	**27.5±3.7**	378	20	10.74 ± 0.9
CGP235	20	29.28	571	46.615	909	3.700	2426	90	**12.7±0.8**	531	25	10.77 ± 1.3
CGP236	20	28.88	495	44.813	768	3.699	2426	52	**13.0±0.9**	497	25	10.63 ± 0.9
CGP239	20	19.63	318	18.086	293	3.698	2426	67	**21.9±2.0**	200	25	10.73 ± 1.2
CGP240	20	28.17	445	34.747	549	3.697	2426	21	**16.4±1.3**	410		
CGP241	21	188.51	1263	27.612	185	3.696	2426	93	**136.3±11.9**	312	29	6.72 ± 1.2

$\rho s(\rho i)$ is the spontaneous (induced) track density (10^5 tracks/cm^2; Ns (Ni) is the number of counted spontaneous (induced) tracks; ρd is the dosimeter track density (10^5 tracks/cm^2; Nd is the number of tracks counted on the dosimeter; P(X^2) is the probability of obtaining Chi-square value (X^2) for n degree of freedom (where n is the number of crystals minus 1). Central ages and corresponding 1σ errors are calculated following Galbraith and Laslett (1993). MTL $\pm$ SD: Mean track length and standard deviation (not c-axis projected).

Table 2.3: Decomposition into age components with BINOMFIT (Ehlers et al., 2005) of samples that did not pass the chi-square (X^2) test above the 5% limit

Sample	P1 age ±1σ [Ma]	P1 (%)	P2 age ±1σ [Ma]	P2 (%)
CGP230	58.5	27.9	103.8	72.1
CGP231	7.1	6.9	19.1	93.1
CGP234	20.4	72.3	59.6	27.7

P1,2 age is the major age component in peak analysis and P1,2 (%) is the percentage of total number of grains in age peak range.

2.5.2 AFT ages

AFT age results are reported in Tab. 2.4 and Fig. 2.3. Ages calculated in this study range between 4.5 and 12.7 Ma, whereas most ages are ~7.5 Ma. All samples pass the chi-square (X^2) test above the 5% limit, which confirms that single grain ages probably derive from a common single age, presumably excluding any partial reheating event (Galbraith, 2005). 28 previously dated AFT samples from the same area (Fig. 2.3) vary in almost the same order from 3.7 to 12.0 Ma (Michalski and Soom (1990), Vernon et al. (2009a) and unpublished data from M. Rahn).

No spatial trend in AFT ages is visible in the dataset (Fig. 2.3), but the NW-SE transect over the Aar massif reveals slightly decreasing ages towards the SE (Fig. 2.4B). The large age difference in samples from the NW of the study area (~4 -12 Ma) derives primarily from variable sample elevations, which range here from >1000 m to <3000 m. However, approximately starting from the middle section of the transect towards the SE, the ages derive from similar elevations between 1000 to 3000 m, while they are slightly becoming younger compare to the ages from the northwest at elevations between 1000 to 3000.

Corresponding confined track length distributions from this study and unpublished data from M. Rahn vary between 11.2 and 14.7 μm (Tab. 2.4, Fig. 2.5, Fig. 2.8 and Fig. 2.10 in the Appendix). Most of the track lengths are ~14 μm long except for four samples from the Aare valley (Fig. 2.5) that yield track lengths <13 μm.

Table 2.4: Apatite fission track results

Sample	# grains	ρs	Ns	ρi	Ni	ρd	Nd	P(χ²) [%]	Central age ±1σ [Ma]	Dpar [µm]	U [ppm]	Confined track lengths # Length	Confined track lengths MTL ± SD (µm)
CGP223	20	4.527	134	71.588	2119	7.586	3257	50	**5.1±0.5**	1.4±0.1	136		
CGP227	20	3.900	94	45.145	1088	7.543	3257	57	**7.5±0.9**	1.4±0.1	82		
CGP230	24	2.448	59	25.187	607	7.517	3257	59	**8.5±1.2**	1.3±0.1	44		
CGP231	24	4.471	131	41.706	1142	7.374	3236	100	**8.8±0.9**	1.0±0.1	73		
CGP232	23	2.679	75	30.215	846	7.499	3257	62	**7.7±1.0**	1.1±0.1	53		
CGP233	20	4.882	83	62.235	1058	7.491	3257	41	**6.8±0.9**	1.2±0.1	108	53	14.2 ± 1.3
CGP234	20	3.436	78	65.463	1486	7.482	3257	80	**4.5±0.6**	1.1±0.1	122	101	13.9 ± 1.4
CGP235	20	1.647	41	23.213	578	7.473	3257	79	**6.1±1.0**	1.1±0.2	40	30	11.3 ± 1.4
CGP236	20	1.962	51	30.154	784	7.465	3257	89	**5.6±0.9**	1.0±0.2	53	50	11.2 ± 1.4
CGP238	20	6.131	168	50.693	1389	7.456	3257	14	**10.5±1.1**	1.4±0.1	91		
CGP239	21	6.530	143	68.174	1493	7.447	3257	71	**8.3±0.8**	1.1±0.1	122		
CGP240	20	4.550	91	54.750	1095	7.439	3257	57	**7.2±0.9**	1.1±0.1	96		
CGP241	20	3.661	82	35.938	805	7.430	3257	92	**8.8±1.1**	1.2±0.1	64	81	13.7 ± 1.4
CW1	20	1.489	49	14.559	479	7.342	3236	99	**8.9±1.4**	1.3±0.2	26		
CW2	20	2.735	61	29.462	657	7.951	3106	97	**8.7±1.2**	1.1±0.2	49		
CW4	25	1.632	62	16.158	614	7.326	3236	100	**8.7±1.2**	1.3±0.2	30		
CW5	20	2.183	43	23.147	456	7.947	3106	100	**8.8±1.5**	1.2±0.1	42		
CW12	18	5.315	118	61.441	1364	7.936	3106	38	**8.1±0.9**	1.3±0.2	110		
CW13	30	3.243	108	23.904	796	7.933	3106	98	**12.7±1.4**	1.1±0.1	41		
CW15	20	4.377	130	45.354	1347	7.929	3106	84	**9.0±0.9**	1.2±0.1	78	54	14.1 ± 1.1
CW16	20	2.098	64	32.295	985	7.926	3106	98	**6.1±0.8**	1.2±0.1	55		
CW17	8	1.488	18	25.702	311	7.922	3106	90	**5.4±1.3**	1.2±0.2	47		
CW20	21	3.828	98	46.328	1186	7.918	3106	96	**7.7±0.9**	1.1±0.1	78		
CW21	5	0.054	37	0.710	485	7.915	3106	43	**7.2±1.3**	1.4±0.1	118		
CW31	23	3.043	98	29.783	959	7.900	3106	62	**9.7±1.1**	1.2±0.2	55		
CW36	30	1.247	51	16.064	657	7.890	3106	100	**7.2±1.1**	1.0±0.1	29		
CW40	25	0.220	52	3.591	847	8.364	3032	94	**5.9±0.9**	1.2±0.2	6		
CW41	20	0.268	55	5.105	1047	8.334	3032	94	**5.0±0.7**	1.1±0.1	8	48	14.2 ± 1.5
CW42	21	0.378	67	7.885	1398	8.319	3032	91	**4.6±0.6**	1.1±0.1	14		
CW43	20	0.156	28	1.992	358	8.304	3032	99	**7.4±1.5**	1.1±0.1	3		
CW44	20	0.169	28	1.995	323	8.289	3032	100	**8.2±1.6**	1.0±0.1	3		
CW48	20	0.176	44	2.938	733	8.273	3032	93	**5.7±0.9**	1.3±0.1	5	33	12.8 ± 1.3
CW49	16	0.190	30	2.933	462	8.258	3032	91	**6.1±1.2**	1.2±0.1	5		
CW50	20	0.371	59	5.245	835	8.243	3032	100	**6.7±0.9**	1.2±0.2	8		

For explanations see Tab. 2.2. D_{par} is the etch pit diameter of fission tracks, averaged from 4 measurements per analysed grain with their standard deviation.

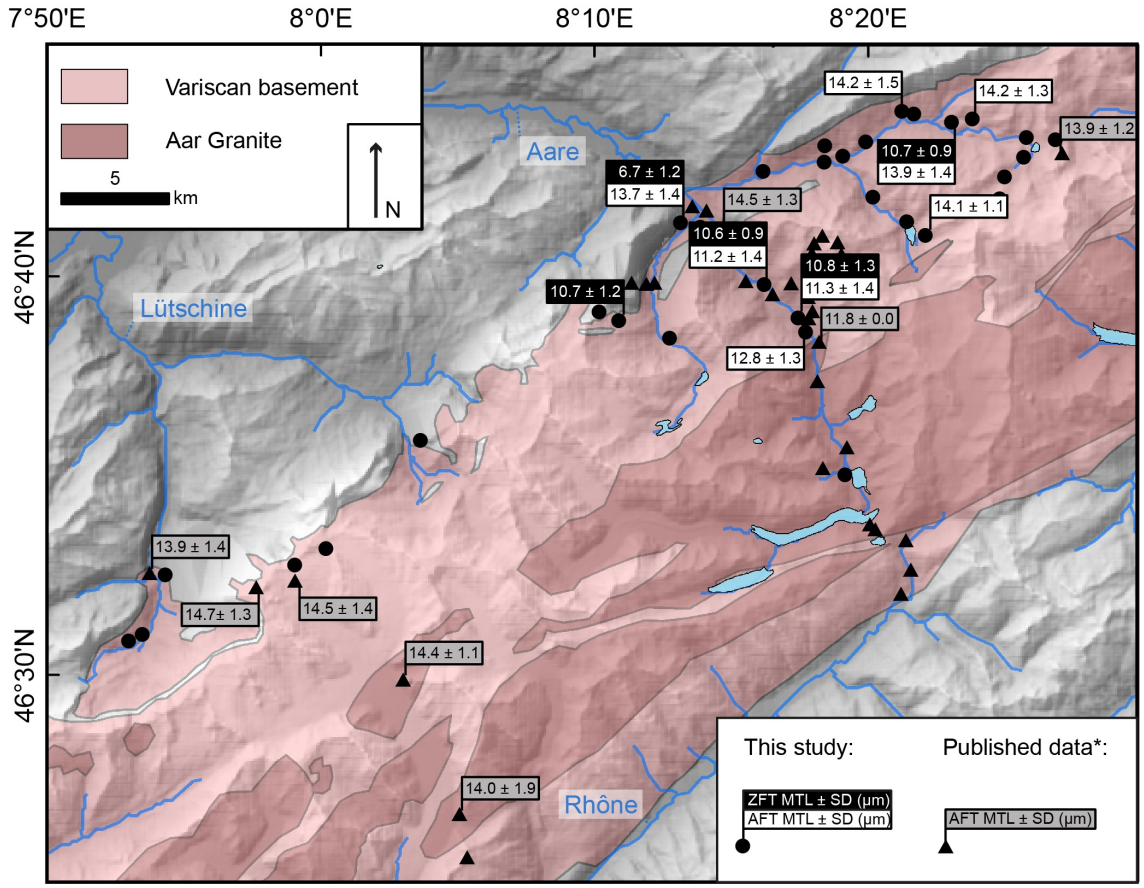

Figure 2.5: Mean track length (MTL) distributions from AFT and ZFT data.*MTLs from Michalski and Soom (1990) and unpublished ones from M. Rahn.

2.5.3 AHe ages

11 bedrock samples yielded suitable apatite grains to measure reliable (U-Th-Sm)/He ages (Tab. 2.5). Four single-grain ages of samples CGP235, CGP241 and CW1 were discarded, because of significantly older ages (>10 Ma), possibly due to micro-inclusions. The AHe ages range from 4.4 to 10.1 Ma, which is exactly within the same range as AFT ages. However, seven AHe ages are as old as their corresponding AFT age or even older (CGP235, 238, 241, CW12, 16, 40, 41). The other AHe ages are not significantly younger, either, as it would have been anticipated with the distinct closure temperature ranges for AHe and AFT thermochronometers, 55-80°C (Farley, 2000) and 90-120°C (e.g. Brandon et al., 1998), respectively.

Table 2.5: AHe ages

Sample	He		U238			Th232				Sm			Excl. ages	Ejection correct.	Uncorr. He-age	Ft-corr. He-age	2σ	Sample unweighted aver. ± 2
	vol. [ncc]	1s [%]	mass [ng]	1s [%]	conc. [ppm]	mass [ng]	1s [%]	conc. [ppm]	Th/U ratio	mass [ng]	1s [%]	conc. [ppm]		(Ft)	[Ma]	[Ma]	[Ma]	[Ma]
CGP232 a1	0.208	1.6	0.341	1.8	39.6	0.028	2.8	3.2	0.08	1.848	9.2	215		0.80	4.76	5.95	0.45	
CGP232 a2	0.234	1.5	0.329	1.8	44.7	0.021	3.3	2.8	0.06	1.577	9.2	214		0.80	5.59	7.00	0.53	**6.6 ± 0.2**
CGP232 a3	0.362	1.3	0.513	1.8	51.8	0.066	2.5	6.7	0.13	2.315	9.2	233		0.81	5.47	6.79	0.49	
CGP232 a4	0.165	1.7	0.258	1.8	50.7	0.015	3.1	2.9	0.06	1.159	9.3	228		0.77	5.04	6.54	0.55	
CGP235 a1	0.123	1.7	0.225	1.8	28.9	0.008	3.6	1.0	0.03	1.604	9.2	206		0.79	4.25	5.36	0.42	
CGP235 a2	0.102	1.8	0.159	1.9	30.1	0.016	3.1	3.1	0.10	1.349	9.2	256		0.71	4.87	6.86	0.69	**6.3 ± 0.5**
CGP235 a3	0.092	2.0	0.136	1.9	23.1	0.025	2.8	4.2	0.18	1.907	9.2	325		0.74	4.85	6.54	0.62	
CGP235 a6	0.623	1.2	0.251	1.8	44.5	0.086	2.5	15.2	0.34	1.450	9.2	258	e	0.78	18.23	23.41	1.82	
CGP236 a2	0.091	2.2	0.218	1.8	48.0	0.013	3.2	2.8	0.06	0.960	9.2	212		0.76	3.31	4.36	0.40	
CGP236 a4	0.050	2.5	0.106	1.9	43.2	0.007	3.7	2.8	0.06	0.489	9.3	200		0.72	3.75	5.20	0.54	**4.4 ± 0.3**
CGP236 a5	0.042	2.8	0.136	1.9	52.5	0.009	3.5	3.3	0.06	0.586	9.3	225		0.66	2.41	3.62	0.44	
CGP236 a6	0.043	2.6	0.104	1.9	31.2	0.005	4.0	1.4	0.04	0.645	9.3	193		0.75	3.23	4.31	0.42	
CGP238 a2	0.308	1.4	0.312	1.8	105.7	0.030	2.7	10.2	0.10	0.750	9.3	255		0.72	7.86	10.95	1.05	
CGP238 a3	0.873	1.2	0.823	1.8	76.3	0.075	2.5	7.0	0.09	3.185	9.2	295		0.83	8.34	10.05	0.66	**10.1 ± 0.4**
CGP238 a4	0.194	1.5	0.233	1.8	110.5	0.022	2.9	10.4	0.09	0.647	9.3	307		0.72	6.60	9.17	0.88	
CGP238 a6	1.150	1.1	1.132	1.8	138.6	0.082	2.5	10.0	0.07	2.568	9.2	314		0.80	8.12	10.18	0.74	
CGP241 a1	0.079	2.1	0.087	1.9	23.6	0.032	2.7	8.6	0.37	0.622	9.3	168		0.75	6.57	8.76	0.81	
CGP241 a2	0.396	1.3	0.145	1.9	42.5	0.010	3.5	2.8	0.07	1.028	9.3	301	e	0.75	21.06	28.09	2.44	**9.5 ± 1.1**
CGP241 a3	2.308	1.1	0.846	1.8	56.2	0.039	2.7	2.6	0.05	4.667	9.3	310	e	0.85	21.36	25.13	1.51	
CGP241 a5	0.248	1.4	0.245	1.8	43.9	0.004	4.1	0.7	0.02	1.820	9.2	326		0.76	7.88	10.33	0.87	
CW1 a1	0.032	3.0	0.020	3.4	20.8	0.006	3.8	6.2	0.30	0.217	9.6	230	e	0.69	11.51	16.69	2.09	
CW1 a2	0.022	3.7	0.037	2.4	26.7	0.007	3.7	5.1	0.19	0.358	9.4	259		0.63	4.38	6.99	0.99	**7.2 ± 0.3**
CW1 a3	0.019	3.9	0.030	2.6	26.2	0.006	3.8	5.3	0.20	0.288	9.4	250		0.61	4.55	7.41	1.10	
CW12 a1	0.123	1.7	0.123	1.9	57.0	0.009	3.5	4.3	0.08	0.587	9.4	271		0.77	7.82	10.15	0.86	
CW12 a2	0.272	1.4	0.330	1.8	87.5	0.013	3.3	3.4	0.04	1.438	9.2	382		0.79	6.54	8.28	0.64	**9.0 ± 0.6**
CW12 a3	0.646	1.2	0.653	1.8	111.3	0.489	2.4	83.4	0.75	1.659	9.3	283		0.79	6.84	8.68	0.65	
CW15 a1	0.316	1.4	0.402	1.8	101.7	0.005	3.9	1.3	0.01	1.127	9.2	285		0.75	6.35	8.47	0.74	
CW15 a2	0.858	1.2	1.115	1.8	116.4	0.027	2.8	2.8	0.02	2.909	9.2	304		0.79	6.21	7.88	0.60	**8.1 ± 0.2**
CW15 a3	0.524	1.3	0.704	1.8	141.9	0.030	2.7	6.0	0.04	1.641	9.2	331		0.77	5.99	7.82	0.64	
CW16 a1	0.110	1.8	0.183	1.8	76.2	0.004	3.9	1.8	0.02	0.559	9.3	233		0.68	4.84	7.11	0.77	
CW16 a2	0.701	1.2	0.936	1.8	73.7	0.045	2.6	3.5	0.05	2.984	9.2	235		0.81	5.98	7.34	0.51	**7.6 ± 0.4**
CW16 a3	0.211	1.5	0.287	1.8	83.7	0.020	2.9	5.9	0.07	0.808	9.2	236		0.70	5.87	8.43	0.86	
CW40 a1	0.021	3.6	0.054	2.1	41.0	0.000	-194.1	0.0	0.00	0.370	9.3	284		0.66	3.13	4.78	0.63	**5.8 ± 1.5**
CW40 a2	0.029	3.2	0.051	2.1	33.1	0.000	297.7	0.1	0.00	0.351	9.3	226		0.64	4.38	6.85	0.90	
CW41 a1	0.758	1.2	0.908	1.8	53.2	0.090	2.5	5.3	0.10	4.515	9.2	265		0.85	6.49	7.63	0.46	**8.1 ± 0.7**
CW41 a2	0.771	1.2	0.805	1.8	44.4	0.054	2.6	3.0	0.07	6.240	9.2	344		0.85	7.34	8.66	0.53	

Ejection correction is the Ft correction following Farley et al. (1996); Hourigan et al. (2005). Significant older ages are excluded. The sample age is given as the unweighted average of the used ages and 2 standard error.

2.6 Discussion

2.6.1 Initial exhumation of the Aar massif

The ZFT ages can be divided into a northern small area with ZFT ages >80 Ma that have not been reset during Alpine orogeny and into Alpine ages of 27 - 12 Ma with decreasing ages towards the south (Fig. 2.4A). Increasing metamorphic grades from north to south (e.g. Marquer and Burkhard, 1992; Albrecht, 1994; Herwegh and Pfiffner, 2005) confirm the assumption that this area has undergone spatially variable maximum temperatures during Alpine orogeny. Due to the big age discrepancy in the spatial distribution of ZFT ages and almost no variation of ages at elevations (Fig. 2.4A), it is resigned to interpret an age-elevation relationship.

The old ages do not represent a distinct cooling event, but rather presenting a part within the external massif, which was overprinted with only very low grade metamorphism during Alpine orogeny (probably always below the ZFT closure temperature of ~260°C) (e.g. Brandon et al., 1998). During Alpine metamorphism, the area has been exposed to sufficiently high temperatures to reset AHe and AFT ages from corresponding samples and also to anneal tracks in zircons (e.g. short MTL from sample CGP241 with ~7 µm, Tab. 2.2, Fig. 2.5 and Fig. 2.10 in the Appendix). Thus, temperatures probably ranged within the PAZ from the ZFT system (e.g. Rahn et al., 2004). The present location of the exposed former ZFT PAZ from the Alpine orogeny is restricted to the first kilometre from the northwest boundary of the massif (Fig. 2.4A).

The majority of ZFT ages range between 12 - 17 Ma independently of the elevation (Fig. 2.4A), however, three ages are older than 19 Ma (CGP233, 234 and 239). The three ages derive from samples that are located close to the northern boundary of the massif (Fig. 2.3 and 2.4A), at which the former ZFT PAZ is nowadays exposed at the surface. According to the corresponding ZFT track lengths distributions of CGP234 and CGP239, these samples were indeed completely reset during Alpine orogeny and, therefore, may demonstrate very early cooling of the Aar massif. Between 30 - 20 Ma, temperatures are supposed to have been ranged around 300°C in most parts of the Aar massif (except for the very northwest boundary from the massif, see above) (Herwegh and Pfiffner, 2005), which was high enough to reset the ZFT thermochronometer. Therefore, the cooling between 27 - 19 Ma could have been due to very early thrusting of the Aar massif contemporaneously with the collision of the European continent with the Adriatic micro-continent that have caused an overall shortening of the massif (e.g. Schmid et al., 1996; Kirschner et al., 2003; Boutoux et al., 2016). This hypothesis is in accordance to the study of Schmid et al. (1996), who suggest that a first updoming of the Aar massif can already be identified for the Early Miocene (~19 Ma) (cf. Fig. 1.3B). The early updoming of the Aar massif might have been preceded by first

exhumation causing very early cooling already at ~27 Ma.
The samples that recorded the first cooling within the Aar massif (ZFT ages: 27 - 19 Ma) appear to be spatially restricted on a small band with a width of ~3 km elongating parallel to the striking direction of the Aar massif (Fig. 2.3 and 2.4A). However, the vast majority of the massif yield in ZFT ages of ~12 - 17 Ma (Fig. 2.3) indicating rapid cooling in that time period. This result is in accordance with the dating of mica formation in the central parts of the massif, which mainly crystallized between 21 - 17 Ma. Since 17 Ma, temperatures have been too low for mica crystallisation (Challandes et al., 2008).
Rapid cooling that began 17 Ma ago in the main parts of the Aar massif would be almost synchronous to the initial cooling of other external massifs, which started at 18 ($\pm$ 1) Ma in the Mont Blanc and Aiguilles Rouges massifs in the Western Alps (Boutoux et al., 2016). The onset of cooling is assumed to be the result of exhumation above frontal crustal ramps within the pro-wedge geometry (Boutoux et al., 2016; von Hagke et al., 2012, 2014).
Mixed brittle-ductile shear zones striking subparallel to the Aar massif in the southeast part of this study area reveal the initiation of transpressive tectonics along the Alpine arc at 13 - 12 Ma (Rolland et al., 2009; Challandes et al., 2008), which coincides with prevailing ZFT ages in this part (Fig. 2.3). However, Rolland et al. (2009) hypothesized that due to shear zone activity in the southeast part of the study area, the main phase of exhumation has been started at ~13 - 12 Ma, whereas only little exhumation occurred before 13 Ma. The movements along the shear zones at 13 - 12 Ma are assumed to be the result of the accelerated anticlockwise rotation of the Adriatic micro-continent (Rolland et al., 2009).
These results lead to the conclusion that during Miocene this area has been undergone by temporally variable onset of exhumation and/or spatially variable exhumation rates along a NW-SE gradient. The Alpine ZFT PAZ at the very northwestern boundary of the massif represents a part, which experienced lower temperatures than the rest of the external massif. Consequently, this part has not been very deeply buried since the Variscan orogeny compare to the vast majority of the massif, which is also demonstrated with increasing metamorphic grades from north to south on presently outcropping bedrocks (Marquer and Burkhard, 1992; Albrecht, 1994; Herwegh and Pfiffner, 2005). According to geological field mapping of Labhart (1977), the ZFT PAZ may represent an autochthonous crystalline unit, which was overthrust by a parautochthonous crystalline unit from a more southerly position. This suggests that the overthrusting occurred out-of-sequence. However, the thrusting may explain the present situation, where rocks from the ZFT PAZ moved less during Alpine orogeny than the vast majority of the massif and, therefore, may have experienced lower temperatures than the rest. Similarly, the main shearing event in the Aar massif is assumed to have taken place between 22 - 20 Ma reflecting main internal shortening of the massif (Rolland et al., 2009; Challandes et al., 2008). Therefore, during the collision of the European continent with the

Adriatic indenter causing internal shortening, a 3 km wide band elongating parallel to the Aar massif may have been thrust towards the north leading to a first cooling between 27 - 19 Ma (Fig. 2.3 and 2.4A). Pre-Alpine ZFT ages are also found at the frontal parts of the Mont Blanc and Aiguilles Rouges massifs (e.g. Vernon et al., 2008), which may originate from a similar situation as in the Aar massif.

However, the onset of the main phase of exhumation in the Aar massif is assumed to have taken place between 17 - 12 Ma. This hypothesis may be supported by confirmed slightly faster exhumation rates between 16 - 14 Ma in the Aar massif and adjacent Gotthard massif by data of Glotzbach et al. (2010). As the middle section of the NW-SE gradient yield ZFT cooling ages of 17 - 15 Ma (kilometres 4 to ~10 in Fig. 2.4A) and the southern part reveals ZFT cooling ages between 13 - 12 Ma (kilometres 12 - 16 in Fig. 2.4A), it may be possible that the exhumation successively proceeded from the northwest to the southeast, confirming the conclusion of Michalski and Soom (1990). On the contrary, increasing metamorphic grades from north to south exposed in outcropping crystalline bedrocks (Marquer and Burkhard, 1992; Albrecht, 1994; Herwegh and Pfiffner, 2005) suggest that crystalline rocks from the south were formerly deeper buried than rocks from the north. This leads to the conclusion that instead of successively proceeding exhumation, the exhumation may have started at almost the same time, but with spatially different exhumation rates. Accordingly, the modelled thermal histories of samples CGP235 and 236 reveal very rapid cooling at 13 - 12 Ma (Fig. 2.6). Nevertheless, it can not be completely excluded that the exhumation started in the north of the massif, even though bedrocks from different depths were brought to the surface.

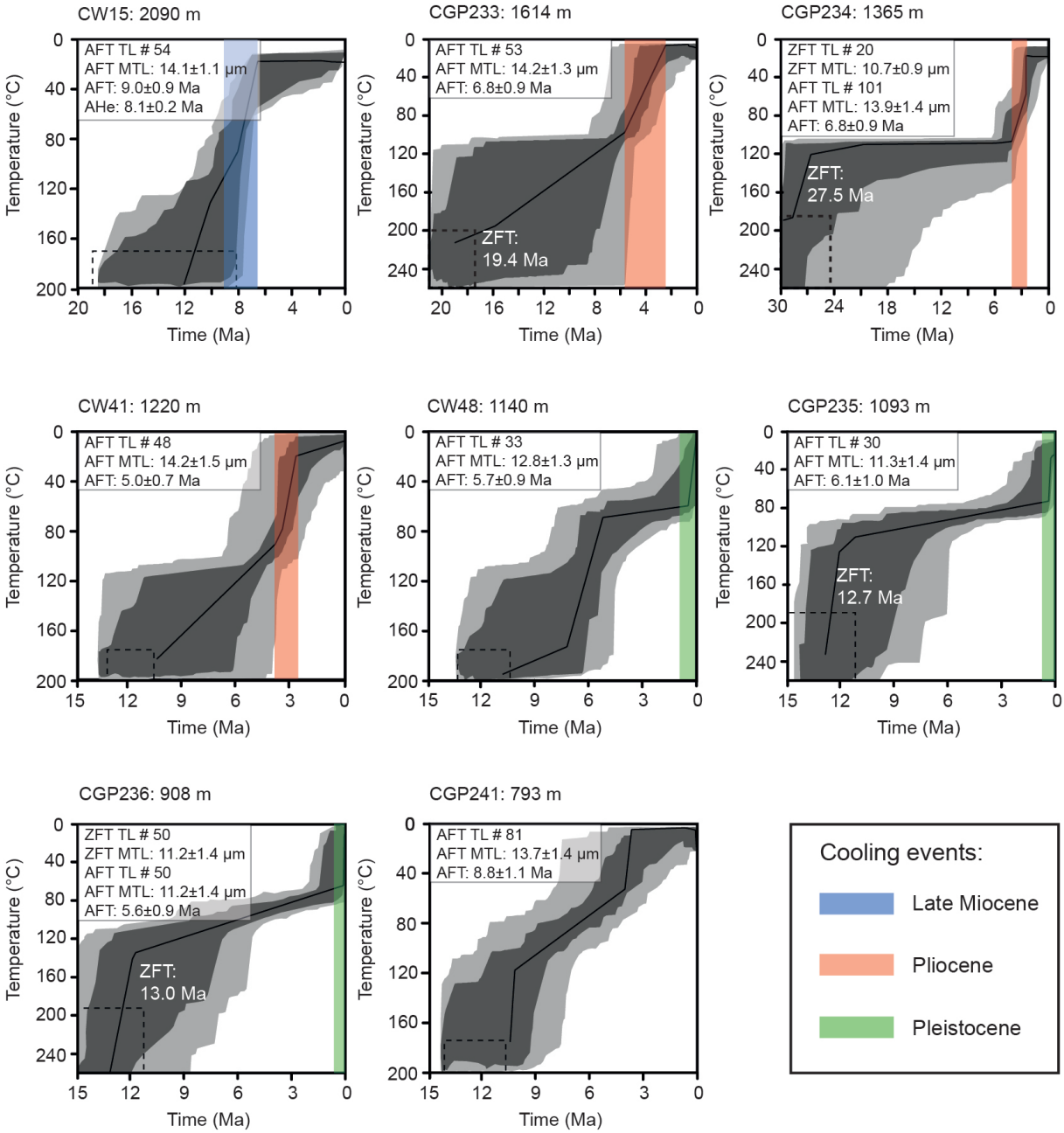

Figure 2.6: HeFTy (Ketcham, 2005) derived time-Temperature (tT) paths for samples with measured AFT track lengths. Named thermochronometers correspond to used input data during modelling. The dashed lines mark the constrain boxes. Models are displayed with a best-fit model (black line), acceptable paths (light gray area) and good paths (dark gray area) (good and acceptable paths correspond to values of the goodness of fit (GOF) of 0.5 and 0.05). Cooling events highlight one phase per sample of rapid cooling (>20°C/Ma) since Late Miocene.

2.6.2 Exhumation history since Late Miocene

Newly determined apatite thermochronological ages cover the same age range (AFT: 4.5 – 12.7 Ma; AHe: 4.4 – 10.1 Ma) as measured ages in the Aar massif and surroundings in other studies (e.g. Michalski and Soom, 1990; Seward and Mancktelow, 1994; Reinecker et al., 2008; Vernon et al., 2008, 2009a; Glotzbach et al., 2010). Therefore, age distributions from this study are combined with published data and are put into context to already existing exhumation histories of this area.

Focusing on the study area, the AFT ages are slightly decreasing towards the south (Fig. 2.4B) confirming former studies of Michalski and Soom (1990) and Reinecker et al. (2008). In contrast, Vernon et al. (2009a) have not observed such a trend, because they counted AFT ages (older ages), which are contradictory to those of Michalski and Soom (1990); especially towards the SE. They speculated that the difference in AFT ages may partly be explained by a generally lower number of counted spontaneous tracks and by apatites of poor quality that are predominant in this area. However, the suggested trend of decreasing AFT ages from north to south is also based on a remarkably old age found by Michalski and Soom (1990) of 12 Ma at 720 m (KAW2207) (Fig. 2.7) that was collected close to the sample CW49 from this study, which, instead, yields only an AFT age of 6.1 Ma (Fig. 2.3). Therefore, due to contradicting AFT ages, the assumed trend of decreasing AFT ages along a NW-SE gradient through the massif may only partly be confirmed by the presented data.

Both, AFT and AHe age-elevation relationships are presented in Fig. 2.7. The ages vary significantly with elevation and do not follow a simple straight trend. It is conspicuous that the AHe ages overlap with the AFT ages. Reasons for this effect will be discussed in a following section (cf. section 2.6.3).

Apparent exhumation rates from previously predicted age-elevation trends of ~0.5 km/Ma for the Aar massif from Michalski and Soom (1990); Reinecker et al. (2008) and Vernon et al. (2009a) are presented in Fig. 2.7. The suggested exhumation rates from Reinecker et al. (2008) and Vernon et al. (2009a) mostly coincide with the shown ages. Greatest deviations appear at lower elevations: “too old” ages at elevations $<$1000 m and “too young” ages at elevations between 1000 – 1600 m. The “too old” ages mostly originate from samples from the northwest boundary of the Aar massif, supporting the assumption of increasing ages towards the NW of Michalski and Soom (1990) and Reinecker et al. (2008), whereas the “too young” ages derive from all over the study area (Fig. 2.3 and 2.4B).

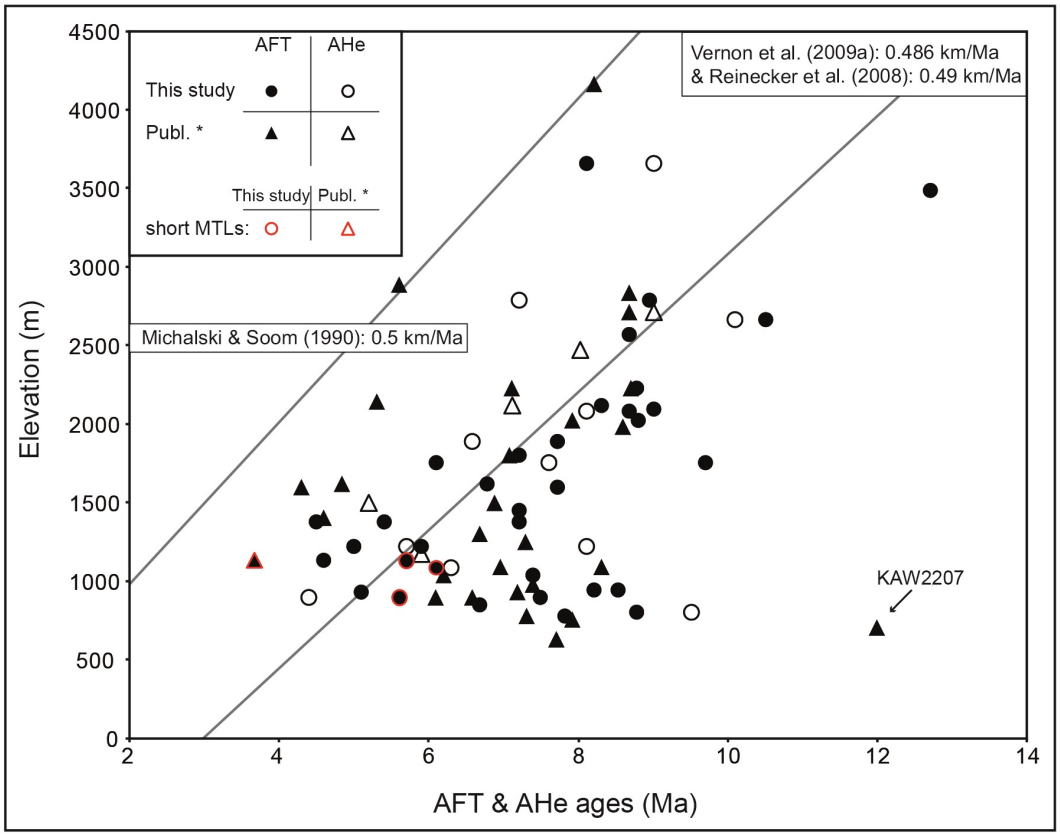

Figure 2.7: Age-elevation relationship of published and new AFT and AHe ages. Apparent exhumation rates correspond to studies from Michalski and Soom (1990); Reinecker et al. (2008) and Vernon et al. (2009a). Note that error bars are not shown due to a high sample density, whose error bars may overlay age-elevation trends.

Large-scale tectonic activity that would have caused spatially variable exhumation in this area can be excluded, because this would have had a recognizable effect on high elevations, too. The occurrence of old ages at the valley bottom in the northwest part of the Aar massif may be a consequence of spatially different exhumation rates and/or temporally different exhumation during the initial exhumation of the Aar massif (cf. section 2.6.1). The widespread incidence of "too young" ages at lower elevations, however, leads to two possible explanations. On the one hand, accelerated hydrothermal activity in the valleys would affect the thermochronological system. On the other hand, relief changes that may result from localized surficial erosion causing accelerated exhumation, would also impact the thermochronological system. The present-day spatial distribution of geothermal fluids does not coincide with the youngest AFT ages and geothermal fluids only reach temperatures of $<30°C$ in this area (Sonney and Vuataz, 2008). This temperature would be too low to influence the AFT thermochronometer, but it can influence the AHe thermochronometer, if the temperature prevails long enough (e.g. Farley, 2000; Gautheron et al., 2009; Flowers et al., 2009). Hence, this would have led to conspicuous young AHe ages (much younger than AFT ages), which is not the case. Therefore, the young ages at low elevations are probably a consequence of

relief changes, presumably caused by the impact of extensive glaciations during the Pleistocene. Furthermore, high valley incision rates during the glaciations were identified for regions south and north of the study area (e.g. Haeuselmann et al., 2007; Valla et al., 2011a) and an impact of accelerated glacial erosion on the exhumation rates was already observed in other studies of the Central and Western Alps (Michalski and Soom, 1990; Reinecker et al., 2008; Glotzbach et al., 2011a; Valla et al., 2012).
It is already known that relief changes are difficult to extract from age-elevation trends (e.g. Vernon et al., 2009a; Valla et al., 2011b). Thus, it may not be surprising that especially at the lower elevations, where the glacial erosion is supposed to be most effective with the largest impact on the topography, no clear age-elevation trend can be seen. However, at high elevations, the AFT and AHe ages can be fitted to an exhumation rate of ~0.5 km/Ma (Fig. 2.7). Therefore, since ~8 - 10 Ma this area has been exhumed with a rate of ~0.5 km/Ma, while especially in the valleys, the thermochronological age distribution was significantly impacted by the effective glacial erosion during the extensive glaciations in the Quaternary.

2.6.2.1 Thermal evolution since Late Miocene

Confined track lengths distributions of apatites can be used to reconstruct the thermal history of rocks. Figure 2.8 demonstrates the relationship between mean track lengths (MTLs) of apatites and sample elevations. Most of the track lengths are about $>$13.5 µm long. This indicates relatively fast cooling through the AFT PAZ (e.g. Gallagher et al., 1998). However, four samples yield short MTLs that indicate a long stay within the PAZ and whose corresponding thermochronological ages may not represent cooling ages. Short AFT MTLs prevail at elevations between 1000 – 1500 m and corresponding samples reveal comparable young ages between 3.7 and 6.1 Ma (Fig. 2.7). Therefore, shortened MTLs at this elevation range may also be the result of effective valley incision during the extensive glaciations (cf. section 2.6.2), which may have caused accelerated exhumation within the last ~2 Ma (Fig. 2.6).
Due to the elevation dependency of AFT MTLs, the tT-models (Fig. 2.6) are also sorted by elevation beginning with the highest sample and measured track lengths (CW15 from 2090 m). Each modelled tT-path shows uniform cooling with at least one phase of rapid cooling with cooling rates of $>$20°C/Ma since Late Miocene. Generally, it can be concluded that decreasing sample elevation leads to decreasing age of cooling events, suggesting that cooling events may be dependent on elevation. This situation is similar to other studies from the Rhône valley (SW of this study area) and the Mont Blanc massif (e.g. Valla et al., 2011a; Glotzbach et al., 2011a).

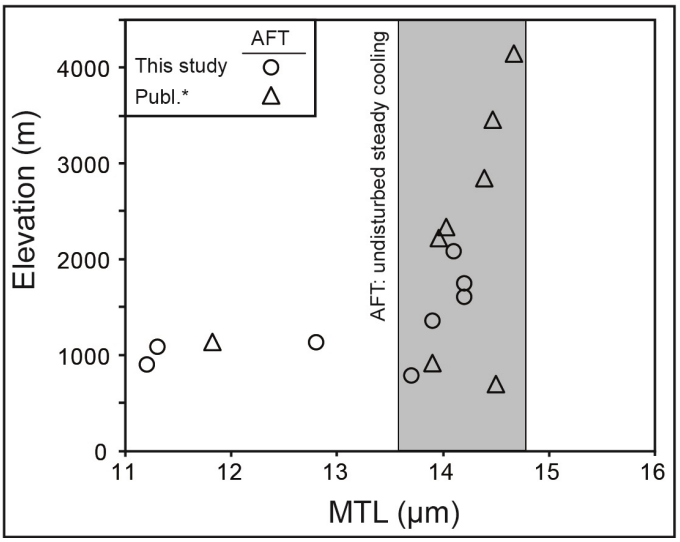

Figure 2.8: AFT mean track lengths (MTL). The gray area highlights MTLs that characterize undisturbed steady cooling. *Published AFT MTL from Michalski and Soom (1990) and unpublished data from M. Rahn.

A cooling event that is here defined as rapid cooling with cooling rates >20°C is completed by 6.5 Ma in the highest sample CW15 (Fig. 2.6). In contrast, samples from elevations between 1600 - 1200 m show accelerated cooling between 5 - 2.5 Ma (CGP233, 234, CW41). Both cooling events are followed by slow or almost no cooling until exposure at surface. tT-models from samples CGP235, 236 and CW48 from elevations between 1100 - 900 m indicate rapid cooling within the last ~1 Ma after a 4 - 5 Ma rest in the AFT PAZ. Moderate cooling between 10 – 4.5 Ma followed by slightly rapid cooling between 4.5 - 3 Ma characterizes the tT-path from sample CGP241. The ZFT age of 136 Ma from sample CGP241 was not reset during Alpine orogeny and, therefore, it was not used as constrain age for the tT-modelling. Due to a strong dependency of choice of constrain age on the tT-models, the thermal history of sample CGP241 might not be reliable. Consequently, the cooling event between 4.5 - 3 Ma is not considered for the interpretation of the thermal history. Nevertheless, rapid cooling within the last ~2 Ma can also be excluded, because track lengths indicate undisturbed steady cooling. Valla et al. (2011a) also described the same phenomenon that $^{4}He/^{3}He$ thermochronometric modelled cooling paths in the southern Aar massif show a strong dependency on elevation, as only at the lowest point an accelerated cooling within the last ~2 Ma is indicated. Their samples from higher elevations reveal elevation-dependent cooling events too.

Previous studies provided contradicting exhumation models for the evolution of the Aar massif (Vernon et al., 2009a; Glotzbach et al., 2010; Valla et al., 2012; Reinecker et al., 2008; Michalski and Soom, 1990), but every suggested exhumation pulse coincides with a tT-model of this dataset (Fig. 2.6). The first exhumation pulse between ~9 – 6.5 Ma was identified in studies from Vernon et al. (2009a); Glotzbach et al. (2010) and Valla et al. (2012), the second

signal between 5 - 2.5 Ma was suggested by studies from Vernon et al. (2009a, 2008) and the youngest exhumation pulse was confirmed by studies from Michalski and Soom (1990); Reinecker et al. (2008) and Valla et al. (2012).

However, three exhumation events in such a small area seem rather unlikely, in particular if the shortening of the Aar massif and associated rock uplift is assumed to be almost uniform for the last ~8 Ma (e.g. von Hagke et al., 2014; Bernet et al., 2001; Schmid et al., 1996). Therefore, active tectonics may not be responsible for the shown exhumation events. It has been assumed that major climate changes during the Late Miocene/Pliocene led to accelerated erosion and exhumation (Willett et al., 2006; Kuhlemann et al., 2002; Cederbom et al., 2004, 2011), however, it turned out that the influence of climate changes is probably below the limit of detection (von Hagke et al., 2012, 2014). Therefore, the inconsistency in previous studies and their suggested exhumation models may mainly arise because of a strong dependency on sampled elevation (Fig. 2.6) and its individual cooling histories may rather be a result of long-term steady-state exhumation (at least since 8 Ma).

It may be possible that a perturbation of near surface isotherms influences the cooling histories of rocks and, therefore, the distribution of thermochronological ages at surface, although the exhumation is uniform. Generally, it is assumed that such a long-wavelength topographic feature like the Aar massif perturbs near surface isotherms (Stüwe et al., 1994). In this case, near surface isotherms may increase in elevation with the topographic elevation along the NW-SE gradient. However, near surface isotherms may also be perturbed by a pronounced topography with a high relief. Consequently, the isotherms are probably widely spaced below mountains and squeezed below major valleys (Fig. 2.9). Accordingly, at constant exhumation, samples may always record decreasing cooling rates below ridges (cooling path A) and increasing cooling rates below valleys (cooling path C). The idealized uniform cooling paths do not, however, include any variations of surface temperature, because cooling rates may increase with decreasing elevation anyway. The described effect can also be observed in the cooling events of the tT-models (Fig. 2.6). Therefore, the elevation-dependent thermal histories of the samples from this study (Fig. 2.6) may be caused by the topographic perturbation of near surface isotherms and eventually indicating that a kind of paleorelief was formed at an early stage during exhumation of the Aar massif. Note that HeFTy-derived tT-paths can not resolve cooling below the temperature of the PRZ (~35°C) and PAZ (~60°C), respectively, because the corresponding thermochronometers do not provide any information about this. Therefore, modelled cooling paths may run almost horizontally during youngest times (CW15, 41 and CGP233, 234).

Nevertheless, the age-elevation trend of AFT and AHe ages (Fig. 2.7) reveal an increased occurrence of young ages at lower elevations, which is assumed to be the consequence of localized effective glacial erosion resulting in increasing relief. Similarly, MTLs of samples

from the same elevation range (Fig. 2.8) indicate a long stay within the PAZ followed by rapid cooling within the last ~2 Ma (Fig. 2.6). In contrast, the cooling path of the lowest sample CGP241 does not reveal intensified cooling within the last 2 Ma and corresponding MTLs are not shortened. This indicates that a possible impact of effective glacial erosion seems to have been concentrated on a distinct elevation range. Therefore, the cooling paths of samples CW48, CGP235 and 236 may support the assumption of accelerated cooling, because of increasing exhumation rates responding to effective glacial erosion. A perturbation of near surface isotherms may have intensified the impact of glacial erosion on the thermal history, resulting in very rapid cooling within the last 2 Ma.

In conclusion, the sample location seems to be crucial for the record of exhumation history; the lower the sampled elevation the younger the cooling event. Although the exhumation is assumed to be uniform since ~8 Ma with a rate of ~0.5 km/Ma, the age of recorded cooling events in tT-models decrease with the elevation. Presumably this effect occurs, because of a perturbation of near surface isotherms below high-relief topography that affects the spacing between isotherms (wide space below mountains, small space below valleys). However, according to the age-elevation trend, increasing relief in terms of effective glacial erosion probably led to young AFT and AHe ages at lower elevations. This effect can also be observed in tT-paths of samples from the same elevations.

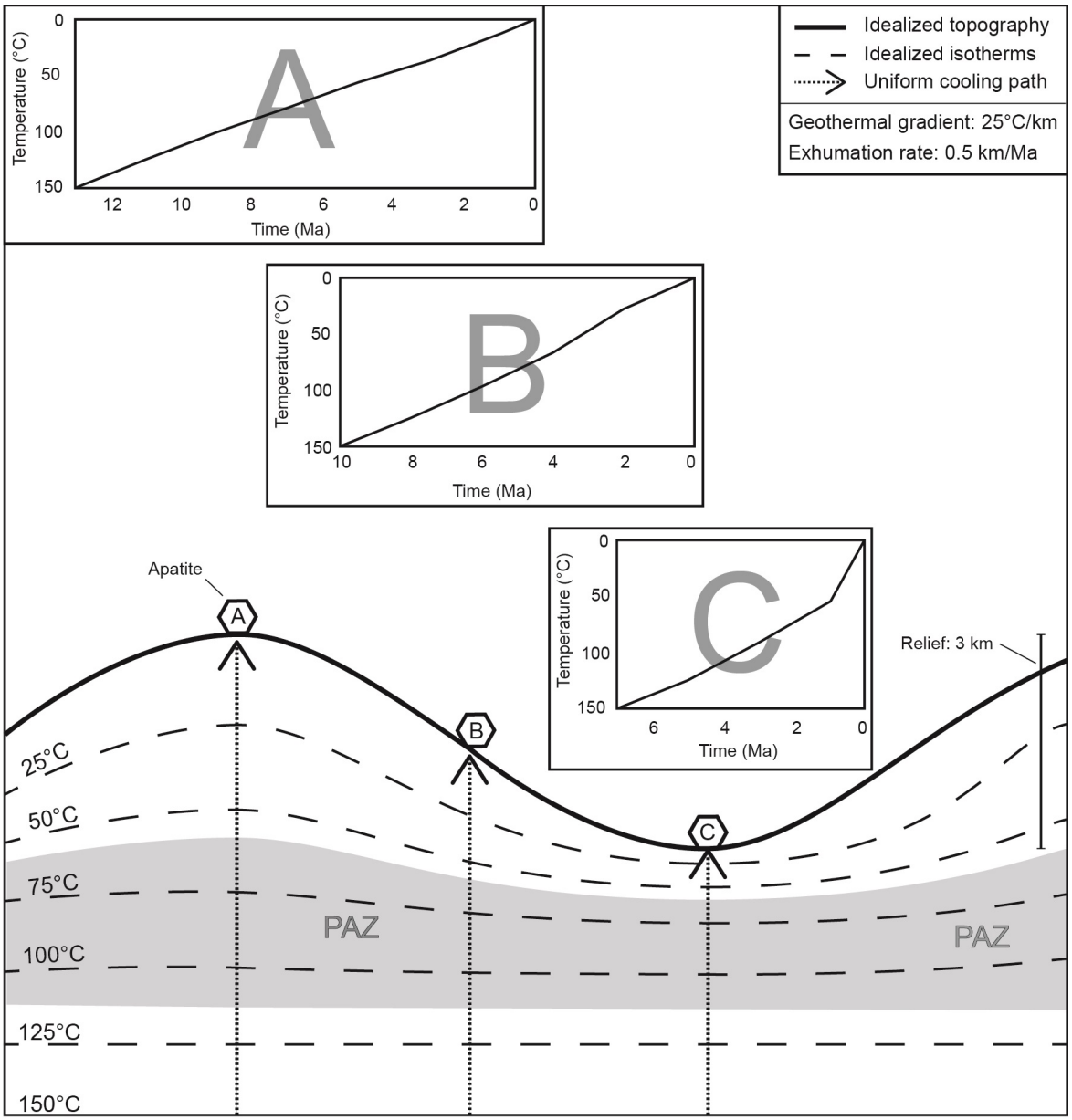

Figure 2.9: Schematic figure about the perturbation on near surface isotherms below a high-relief topography. Input parameter were chosen similar to the situation described here, relief of 3 km, exhumation rate of 0.5 km/Ma and a geothermal gradient of 25°C/km, which is a commonly used value in the Central and Western Alps (e.g. Vernon et al., 2008). A, B and C represent elevation-dependent cooling paths of apatites at constant uniform exhumation, whose cooling rates increase with decreasing elevation. At a depth of 5 - 6 km, the isotherms run horizontally and are not perturbed by the topography.

2.6.3 Overlapping AFT and AHe ages

Figure 2.7 particularly demonstrates that the AHe ages are not remarkably younger than the AFT ages. Vernon et al. (2009a) also presented conflicting AFT and AHe ages from this study area (five AHe ages from Vernon et al. (2009a), which are displayed in Fig. 2.3 and 2.7) and explained older AHe ages compared to AFT ages by U-Th zoning with concentrated U and Th in the internal parts of the grains, which may have led to overestimated AHe ages (e.g. Meesters and Dunai, 2002). As these samples do not show any U-Th zoning, this condition is not met by these samples. A thermochronological study in the southernmost part of the Aar massif also reveals overlapping AHe and AFT ages (Valla et al., 2012). Their "too old" AHe ages yield high effective Uranium concentrations (eU = [U conc.] + 0.235·[Th conc.] after Flowers et al. (2009)) of 80 – 210 ppm that may have led to higher AHe closure temperatures (e.g. Flowers et al., 2009; Gautheron et al., 2009). Accordingly, they recommend to consider the radiation damage effect on apatite He retention for thermal history modelling (e.g. Gautheron et al., 2009), although the samples cooled rapidly. However, the AHe samples presented here, demonstrate firstly, that the U and Th concentrations vary independently of the cooling age and, secondly, that only three samples yield U and Th concentrations in the range of 80 – 210 ppm like the samples from Valla et al. (2012). These high eU grains also include the few AHe ages that are younger than corresponding AFT ages, whereas all other samples yield normal eU concentrations of 30 – 50 ppm (Tab. 2.5). Therefore, the "too old" AHe ages are not a consequence of parent isotope zonation and/or radiation damage.

Possibly the dated AFT ages are biased by unusual annealing kinetics. Measured D_{par} values of all samples are almost identical, yielding low D_{par} values of 1.0 to 1.4 µm (Tab. 2.4). Low D_{par} values are usually interpreted to represent F- or OH-apatite with a relatively low closure temperature (Donelick et al., 2005). The unknown influence of other anions or cations may have an impact on AFT annealing kinetics and therefore on the AFT ages (e.g. Barbarand et al., 2003; Spiegel et al., 2007). Consequently, it is probable that a combination of both, the low closure temperature of the AFT thermochronometer and the rapid exhumation that may not be reported by the AHe system (unknown behavior of U and Th), led to overlapping AFT and AHe ages.

2.7 Conclusions

The spatial distribution of pre-Alpine ZFT ages (ZFT ages >80 Ma) of the Aar massif suggest that at the very northern boundary along the massif rocks of the former ZFT PAZ from the Alpine orogeny are outcropping. During the initial shortening of the Aar massif due to collision of the Adriatic indenter with the European continent, internal northwest parts of the massif were eventually overthrust onto the rocks of the ZFT PAZ, which may explain an early cooling event between 27 - 19 Ma. However, the main phase of exhumation of the Aar massif began at ~17 Ma, which is almost synchronously to other external massifs in the Western Alps (e.g. Mont Blanc and Aiguilles Rouges massifs). At 13 - 12 Ma the exhumation was further intensified in the SE parts of the Aar massif. The onset of exhumation was probably rapid, because of a widespread distribution of similar cooling ages, although the exhumation rates may have increased from the NW to the SE. Due to outcropping rocks that originate from different depths, it is suggested that the exhumation rates varied during the main phase of exhumation.

AFT and AHe ages reveal that since Late Miocene the entire Aar massif has been exhumed with an uniform rate of ~0.5 km/Ma. The cooling ages slightly decrease along a NW-SE gradient through the massif, presumably a consequence of spatially variable exhumation rates during the main phase of exhumation. However, contradictory to previous studies, the elevation-dependent thermal models of the thermochronological data show that there did not occur phases of accelerated exhumation within the last ~8 - 2 Ma. Different timing as well as different pace of cooling events in the thermal models may be rather a relict of a perturbation of near surface isotherms below a high-relief topography than phases of accelerated exhumation. A perturbation of near surface isotherms imply slow cooling below ridges and rapid cooling below valleys.

Nevertheless, focused effective glacial erosion during the Pleistocene glaciations caused accelerated exhumation within glacial valleys. Therefore, the age-elevation relationship reveals an increased occurrence of young AFT and AHe ages at lower elevations.

2.8 Appendix

The relative frequency of fission track length distributions from AFT and ZFT measurements (Fig. 2.10).

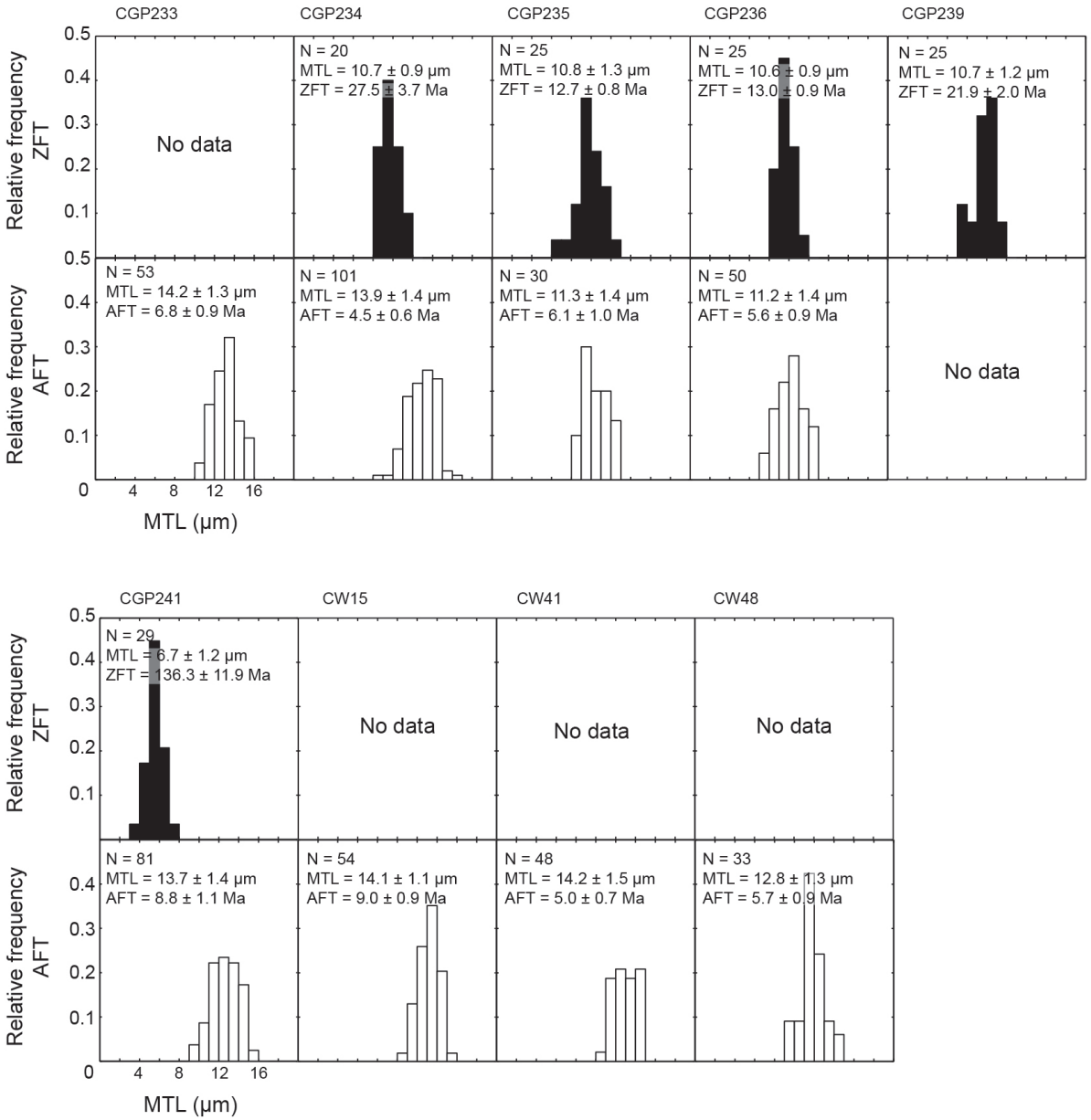

Figure 2.10: AFT and ZFT mean track lengths (MTL).

References

Albrecht, J. (1994), 'Geologic units of the Aar massif and their pre-Alpine roch associations: a critical review', *Schweiz. Mineral. Petrogr. Mitt.* **74**, 5–27.

Barbarand, J., Carter, A., Wood, I. and Hurford, T. (2003), 'Compositional and structural control of fission-track annealing in apatite', *Chemical Geology* **198**(1-2), 107–137.

Bernet, M., Zattin, M., Garver, J. I., Brandon, M. T. and Vance, J. A. (2001), 'Steady-state exhumation of the European Alps', *Geology* **29**(1), 35.

Boutoux, A., Bellahsen, N., Nanni, U., Pik, R., Verlaguet, A., Rolland, Y. and Lacombe, O. (2016), 'Thermal and structural evolution of the external Western Alps: Insights from (U–Th–Sm)/He thermochronology and RSCM thermometry in the Aiguilles Rouges/Mont Blanc massifs', *Tectonophysics* **683**, 109–123.

Brandon, M. T., Roden-Tice, M. K. and Garver, J. I. (1998), 'Late Cenozoic exhumation of the Cascadia accretionary wedge in the Olympic Mountains, northwest Washington State', *Geological Society of America Bulletin* **110**(8), 985–1009.

Calais, E., Nocquet, J.-M., Jouanne, F. and Tardy, M. (2002), 'Current strain regime in the Western Alps from continuous Global Positioning System measurements, 1996-2001', *Geology* **30**, 651–654.

Cederbom, C. E., Sinclair, H. D., Schlunegger, F. and Rahn, M. K. (2004), 'Climate-induced rebound and exhumation of the European Alps', *Geology* **32**(8), 709.

Cederbom, C. E., van der Beek, P., Schlunegger, F., Sinclair, H. D. and Oncken, O. (2011), 'Rapid extensive erosion of the North Alpine foreland basin at 5-4 Ma', *Basin Research* **23**(5), 528–550.

Challandes, N., Marquer, D. and Villa, I. M. (2008), 'P-T-t modelling, fluid circulation, and 39Ar-40Ar and Rb-Sr mica ages in the Aar Massif shear zones (Swiss Alps)', *Swiss Journal of Geosciences* **101**(2), 269–288.

Champagnac, J.-D., Schlunegger, F., Norton, K., von Blanckenburg, F., Abbühl, L. M. and Schwab, M. (2009), 'Erosion-driven uplift of the modern Central Alps', *Tectonophysics* **474**(1-2), 236–249.

Dodson, M. H. (1973), 'Closure temperature in cooling geochronological and petrological systems', *Contributions to Mineralogy and Petrology* **40**(3), 259–274.

Donelick, R. A., O'Sullivan, P. B. and Ketcham, R. A. (2005), 'Apatite Fission-Track Analysis', *Reviews in Mineralogy and Geochemistry* **58**, 49–94.

Dunkl, I. (2002), 'Trackkey: a Windows program for calculation and graphical presentation of fission track data', *Computers & Geosciences* **28**(1), 3–12.

Ehlers, T. A. and Farley, K. A. (2003), 'Apatite (U–Th)/He thermochronometry: Methods and applications to problems in tectonic and surface processes', *Earth and Planetary Science Letters* **206**(1-2), 1–14.

Farley, K. A. (2000), 'Helium diffusion from apatite: General behavior as illustrated by Durango fluorapatite', *Journal of Geophysical Research* **105**(B2), 2903.

Farley, K. A. (2002), '(U-Th)/He Dating: Techniques, Calibrations, and Applications', *Reviews in Mineralogy and Geochemistry* **47**(1), 819–844.

Farley, K. A., Wolf, R. A. and Silver, L. T. (1996), 'The effects of long alpha-stopping distances on (UTh)/He ages', *Geochimica et Cosmochimica Acta* **60**(21), 4223–4229.

Flowers, R. M., Ketcham, R. A., Shuster, D. L. and Farley, K. A. (2009), 'Apatite (U–Th)/He thermochronometry using a radiation damage accumulation and annealing model', *Geochimica et Cosmochimica Acta* **73**(8), 2347–2365.

Galbraith, R. F. (2005), *Statistics for Fission Track Analysis*, Chapman and Hall, New York.

Galbraith, R. F. and Laslett, G. M. (1993), 'Statistical models for mixed fission track ages', *Nuclear Tracks and Radiation Measurements* **21**(4), 459–470.

Gallagher, K., Brown, R. and Johnson, C. (1998), 'Fission Track Analysis and its applications to geological problems', *Annual Review of Earth and Planetary Sciences* **26**(1), 519–572.

Gautheron, C., Tassan-Got, L., Barbarand, J. and Pagel, M. (2009), 'Effect of alpha-damage annealing on apatite (U–Th)/He thermochronology', *Chemical Geology* **266**(3-4), 157–170.

Gleadow, A. (1981), 'Fission-track dating methods: What are the real alternatives?', *Nuclear Tracks* **5**(1-2), 3–14.

Glotzbach, C., Bernet, M. and van der Beek, P. (2011b), 'Detrital thermochronology records changing source areas and steady exhumation in the Western European Alps', *Geology* **39**(3), 239–242.

Glotzbach, C., Reinecker, J., Danišík, M., Rahn, M., Frisch, W. and Spiegel, C. (2008), 'Neogene exhumation history of the Mont Blanc massif, western Alps', *Tectonics* **27**(4).

Glotzbach, C., Reinecker, J., Danišík, M., Rahn, M., Frisch, W. and Spiegel, C. (2010), 'Thermal history of the central Gotthard and Aar massifs, European Alps: Evidence for steady state, long-term exhumation', *Journal of Geophysical Research* **115**(F3).

Glotzbach, C., van der Beek, P. and Spiegel, C. (2011a), 'Episodic exhumation and relief growth in the Mont Blanc massif, Western Alps from numerical modelling of thermochronology data', *Earth and Planetary Science Letters* **304**(3-4), 417–430.

Green, P., Duddy, I., Gleadow, A., Tingate, P. and Laslett, G. (1986), 'Thermal annealing of fission tracks in apatite', *Chemical Geology: Isotope Geoscience section* **59**, 237–253.

Haeuselmann, P., Granger, D. E., Jeannin, P.-Y. and Lauritzen, S.-E. (2007), 'Abrupt glacial valley incision at 0.8 Ma dated from cave deposits in Switzerland', *Geology* **35**(2), 143–146.

Hänni, R. and Pfiffner, O. (2001), 'Evolution and internal structure of the Helvetic nappes in the Bernese Oberland', *Eclogae Geologicae Helvetiae* **94**.

Herwegh, M. and Pfiffner, O. (2005), 'Tectono-metamorphic evolution of a nappe stack: A case study of the Swiss Alps', *Tectonophysics* **404**(1-2), 55–76.

Hourigan, J. K., Reiners, P. W. and Brandon, M. T. (2005), 'U-Th zonation-dependent alpha-ejection in (U-Th)/He chronometry', *Geochimica et Cosmochimica Acta* **69**(13), 3349–3365.

Hurford, A. J. and Green, P. F. (1982), 'A users' guide to fission track dating calibration', *Earth and Planetary Science Letters* **59**(2), 343–354.

Hurford, A. J. and Green, P. F. (1983), 'The zeta age calibration of fission-track dating', *Chemical Geology* **41**, 285–317.

Ketcham, R. A. (2005), 'Forward and Inverse Modeling of Low-Temperature Thermochronometry Data', *Reviews in Mineralogy and Geochemistry* **58**(1), 275–314.

Ketcham, R. A., Carter, A., Donelick, R. A., Barbarand, J. and Hurford, A. J. (2007), 'Improved modeling of fission-track annealing in apatite', *American Mineralogist* **92**(5-6), 799–810.

Kirschner, D. L., Masson, H. and Cosca, M. A. (2003), 'An 40 Ar/ 39 Ar, Rb/Sr, and stable isotope study of micas in low-grade fold-and-thrust belt: An example from the Swiss Helvetic Alps', *Contributions to Mineralogy and Petrology* **145**(4), 460–480.

Kuhlemann, J., Frisch, W., Székely, B., Dunkl, I. and Kázmér, M. (2002), 'Post-collisional sediment budget history of the Alps: tectonic versus climatic control', *International Journal of Earth Sciences* **91**(5), 818–837.

Labhart, T. P. (1977), *Aarmassiv und Gotthardmassiv*, Gebr. Borntraeger, Berlin.

Marquer, D. and Burkhard, M. (1992), 'Fluid circulation, progressive deformation and mass-transfer processes in the upper crust: the example of basement-cover relationships in the External Crystalline Massifs, Switzerland', *Journal of Structural Geology* **14**(8/9), 1047–1057.

Meesters, A. and Dunai, T. (2002), 'Solving the production–diffusion equation for finite diffusion domains of various shapes: Part I. Implications for low-temperature (U–Th)/He thermochronology', *Chemical Geology* **186**(3-4), 333–344.

Michalski, I. and Soom, M. (1990), 'The Alpine thermo-tectonic evolution of the Aar and Gotthard massifs, Central Switzerland: fission track ages on zircon and apatite and K-Ar mica ages', *Schweiz. Mineral. Petrogr. Mitt.* (70), 373–387.

Naeser, C. W. (1967), 'The use of apatite and sphene for fission track age determinations', *Geological Society of America Bulletin* **78**(12), 1523.

Naeser, N. D., Zeitler, P. K., Naeser, C. W. and Cerveny, P. F. (1987), 'Provenance studies by fission-track dating of zircon-etching and counting procedures', *International Journal of Radiation Applications and Instrumentation. Part D. Nuclear Tracks and Radiation Measurements* **13**(2-3), 121–126.

Nocquet, J.-M. (2012), 'Present-day kinematics of the Mediterranean: A comprehensive overview of GPS results', *Tectonophysics* **579**, 220–242.

Pleuger, J., Mancktelow, N., Zwingmann, H. and Manser, M. (2012), 'K–Ar dating of synkinematic clay gouges from Neoalpine faults of the Central, Western and Eastern Alps', *Tectonophysics* **550-553**, 1–16.

Quadt, A. v. and Schaltegger, U. (1990), 'U-Pb zircon dating of the Central Aar Granite (Aar Massif, Central Alps)', *Schweiz. Mineral. Petrogr. Mitt.* **70**, 361–371.

Rahn, M. K., Brandon, M. T., Batt, G. E. and Garver, J. I. (2004), 'A zero-damage model for fission-track annealing in zircon', *American Mineralogist* **89**(4), 473–484.

Reinecker, J., Danišík, M., Schmid, C., Glotzbach, C., Rahn, M., Frisch, W. and Spiegel, C. (2008), 'Tectonic control on the late stage exhumation of the Aar Massif (Switzerland): Constraints from apatite fission track and (U-Th)/He data', *Tectonics* **27**(6), n/a.

Reiners, P. W. and Brandon, M. T. (2006), 'Using Thermochsonology to understand orogenic erosion', *Annual Review of Earth and Planetary Sciences* **34**(1), 419–466.

Rolland, Y., Cox, S. and Corsini, M. (2009), 'Constraining deformation stages in brittle–ductile shear zones from combined field mapping and 40Ar/39Ar dating', *Journal of Structural Geology* **31**(11), 1377–1394.

Schlatter, A., Schneider, D., Geiger, A. and Kahle, H.-G. (2005), 'Recent vertical movements from precise levelling in the vicinity of the city of Basel, Switzerland', *International Journal of Earth Sciences* **94**(4), 507–514.

Schmid, S. M., Fgenschuh, B., Kissling, E. and Schuster, R. (2004), 'Tectonic map and overall architecture of the Alpine orogen', *Eclogae Geologicae Helvetiae* **97**(1), 93–117.

Schmid, S. M. and Kissling, E. (2000), 'The arc of the western Alps in the light of geophysical data on deep crustal structure', *Tectonics* **19**(1), 62–85.

Schmid, S. M., Pfiffner O. A., Froitzheim N., Schönborn G. and Kissling E. (1996), 'Geophysical - geological transect and tectonic evolution of the Swiss-Italian Alps', *Tectonics* **15**, 1036–1064.

Seward, D. and Mancktelow, N. S. (1994), 'Neogene kinematics of the central and western Alps: Evidence from fission-track dating', *Geology* **22**(9), 803.

Sonney, R. and Vuataz, F.-D. (2008), 'Properties of geothermal fluids in Switzerland: A new interactive database', *Geothermics* **37**(5), 496–509.

Spiegel, C., Kohn, B., Raza, A., Rainer, T. and Gleadow, A. (2007), 'The effect of long-term low-temperature exposure on apatite fission track stability: A natural annealing experiment in the deep ocean', *Geochimica et Cosmochimica Acta* **71**(18), 4512–4537.

Steck, A. and Hunziker, J. (1994), 'The Tertiary structural and thermal evolution of the Central Alps—compressional and extensional structures in an orogenic belt', *Tectonophysics* **238**(1-4), 229–254.

Stüwe, K., White, L. and Brown, R. (1994), 'The influence of eroding topography on steady-state isotherms. Application to fission track analysis', *Earth and Planetary Science Letters* **124**(1-4), 63–74.

Tagami, T., Carter, A. and Hurford, A. J. (1996), 'Natural long-term annealing of the zircon fission-track system in Vienna Basin deep borehole samples: Constraints upon the partial annealing zone and closure temperature', *Chemical Geology* **130**(1-2), 147–157.

Trümpy, R. (1980), *Geology of Switzerland*, Wepf and Co, Basel.

Valla, P. G., Shuster, D. L. and van der Beek, P. A. (2011a), 'Significant increase in relief of the European Alps during mid-Pleistocene glaciations', *Nature Geoscience* **4**(10), 688–692.

Valla, P. G., van der Beek, P. A. and Braun, J. (2011b), 'Rethinking low-temperature thermochronology data sampling strategies for quantification of denudation and relief histories: A case study in the French western Alps', *Earth and Planetary Science Letters* **307**(3-4), 309–322.

Valla, P. G., van der Beek, P. A., Shuster, D. L., Braun, J., Herman, F., Tassan-Got, L. and Gautheron, C. (2012), 'Late Neogene exhumation and relief development of the Aar and Aiguilles Rouges massifs (Swiss Alps) from low-temperature thermochronology modeling and 4 He/ 3 He thermochronometry', *Journal of Geophysical Research: Earth Surface* **117**(F1), n/a.

van der Beek, P. A., Valla, P. G., Herman, F., Braun, J., Persano, C., Dobson, K. J. and Labrin, E. (2010), 'Inversion of thermochronological age–elevation profiles to extract independent estimates of denudation and relief history — II: Application to the French Western Alps', *Earth and Planetary Science Letters* **296**(1-2), 9–22.

Vernon, A. J., van der Beek, P. A. and Sinclair, H. D. (2009b), 'Spatial correlation between long-term exhumation rates and present-day forcing parameters in the western European Alps', *Geology* **37**(9), 859–862.

Vernon, A. J., van der Beek, P. A., Sinclair, H. D., Persano, C., Foeken, J. and Stuart, F. M. (2009a), 'Variable late Neogene exhumation of the central European Alps: Low-temperature thermochronology from the Aar Massif, Switzerland, and the Lepontine Dome, Italy', *Tectonics* **28**(5).

Vernon, A., van der Beek, P., Sinclair, H. and Rahn, M. (2008), 'Increase in late Neogene denudation of the European Alps confirmed by analysis of a fission-track thermochronology database', *Earth and Planetary Science Letters* **270**(3-4), 316–329.

von Hagke, C., Cederbom, C. E., Oncken, O., Stöckli, D. F., Rahn, M. K. and Schlunegger, F. (2012), 'Linking the northern Alps with their foreland: The latest exhumation history resolved by low-temperature thermochronology', *Tectonics* **31**(5), n/a–n/a.

von Hagke, C., Oncken, O., Ortner, H., Cederbom, C. E. and Aichholzer, S. (2014), 'Late Miocene to present deformation and erosion of the Central Alps — Evidence for steady state ', *Tectonophysics* **632**, 250–260.

Wagner, G. (1968), 'Fission track dating of apatites', *Earth and Planetary Science Letters* **4**(5), 411–415.

Wagner, G. and van den Haute, P. (1992), *Fission-track Dating*, Kluwer, Dordrecht.

Willett, S. D., Schlunegger, F. and Picotti, V. (2006), 'Messinian climate change and erosional destruction of the central European Alps', *Geology* **34**(8), 613.

Wittmann, H., von Blanckenburg, F., Kruesmann, T., Norton, K. P. and Kubik, P. W. (2007), 'Relation between rock uplift and denudation from cosmogenic nuclides in river sediment in the Central Alps of Switzerland', *Journal of Geophysical Research* **112**(F4).

Wolf, R., Farley, K. and Silver, L. (1996), 'Helium diffusion and low-temperature thermochronometry of apatite', *Geochimica et Cosmochimica Acta* **60**(21), 4231–4240.

Zaun, P. E. and Wagner, G. A. (1985), 'Fission-track stability in zircons under geological conditions', *Nuclear Tracks and Radiation Measurements (1982)* **10**(3), 303–307.

Zeitler, P. K., Herczeg, A. L., McDougall, I. and Honda, M. (1987), 'U-Th-He dating of apatite: A potential thermochronometer', *Geochimica et Cosmochimica Acta* **51**(10), 2865–2868.

3 Maximum glacial erosion around the equilibrium line altitude of glaciers: New insights from low-temperature thermochronology

3.1 Abstract

The topography of the European Alps, like other mountain ranges, was strongly affected by Pleistocene glaciations. It is known that significant valley incision must have occurred during the Pleistocene glaciations, but the inner-Alpine valley evolution remains difficult to resolve. Here we use low temperature thermochronology to identify the spatial distribution of glacial erosion in three main valleys that incise into the Aar massif of the Swiss Alps. New and published thermochronometric data provide a high spatial sample density (69 cooling ages), in which the youngest thermochronological ages do not appear at the lowest point, but at mean elevations of major valleys. The resulting age-elevation trend is crescentic, a typical feature of headward propagation of glacial erosion. The coincidence of the youngest ages and the equilibrium line altitude (ELA) of former glaciations emphasizes that especially along the ELA the removal was particularly intense.

3.2 Introduction

High relief areas like the European Alps obtained their characteristic topography from the interaction between erosion and tectonics, at which glacial erosion has been playing a dominant role since the Pleistocene (Egholm et al., 2009; Haeuselmann et al., 2007; Herman et al., 2013; Robl et al., 2015). The topographic evolution of high mountainous areas at all latitudes (such as Himalayas, Andes and Alps) was perturbed by the onset of Pleistocene glaciations, while having a strong effect on the erosional history (e.g. Herman et al., 2013). As a consequence, characteristic geomorphic forms of glacial erosion can be found in every mountain range, where past or present glaciers prevailed, e.g. U-shaped valleys, hanging valleys or cirques. Glacial erosion is assumed to be responsible for effective glacial valley carving and cirque retreat (e.g. Penck, 1905; MacGregor et al., 2000) in addition to a focus of the erosional strength at or around the equilibrium line altitude of glaciers (ELA) (e.g. Egholm et al., 2009; Robl et al., 2015). Through broadening and deepening of valley floors and removal of ridges and peaks, the glacial erosion may fundamentally reshape the pre-glacial topography (e.g. Shuster et al., 2011; Sternai et al., 2012). As an example, Pleistocene glaciations in the European Alps resulted in an increase of local relief and a decrease of mean elevation (e.g. Valla et al., 2011; Sternai et al., 2012; Fox et al., 2015; Pedersen et al., 2014). The onset of enhanced glacial erosion and reshaping of the Alpine topography can be dated to ~0.8 -1 Ma, based on (i) modelling of thermochronological data (Glotzbach et al., 2011a; Valla et al., 2011) and (ii) cosmogenic nuclide dating of cave sediments (Haeuselmann et al., 2007). Although the beginning of extensive glaciation is known (e.g. Haeuselmann et al., 2007; Schlüchter, 2004), there is still a lack of understanding about the local to regional extent of Alpine glacial erosion and the relative contribution of fluvial and glacial erosion on the present shape of mountainous areas.

In this study we quantify the spatial distribution of glacial erosion during the Pleistocene glaciations using thermochronometric data. Glacial erosion may lead to strong lateral variations in exhumation rates and as a result to a perturbation of thermochronological ages, identifiable in the thermochronological age and elevation relation (Densmore et al., 2007; Shuster et al., 2011). Here we identified such a distinct trend in apatite fission track (AFT) and apatite (U-Th-Sm)/He (AHe) data from three major valleys, Urbachtal, Haslital and Gadmental in the Central Alps in Switzerland (Fig. 3.1).

Geologically, this area is part of the external Aar massif, where crystalline basement rocks are outcropping (e.g. Albrecht, 1994). They were uplifted and exhumed in Early to Middle Miocene times as a consequence of convergence between the European and African continent followed by subsequent nappe stacking and crustal thickening (e.g. Schmid et al., 1996). The study area reveals similar zircon fission track ages of ~12 Ma, indicating rapid

initial exhumation of the massif (e.g. Michalski and Soom, 1990; Glotzbach et al., 2010). Detrital apatite fission track (AFT) as well as AFT derived surface cooling ages yield nearly constant exhumation rates of ~0.5 - 0.7 km/Ma since rapid initial exhumation of the massif (e.g. Vernon et al., 2009, 2008; Glotzbach et al., 2011b). These exhumation rates are in the same order as present-day erosion and rock uplift rates (0.5 - 0.7 mm/a), suggesting that the majority of recent uplift in the Western and Central Alps is the isostatic response to erosion (Wittmann et al., 2007; Champagnac et al., 2009; Schlatter et al., 2005).

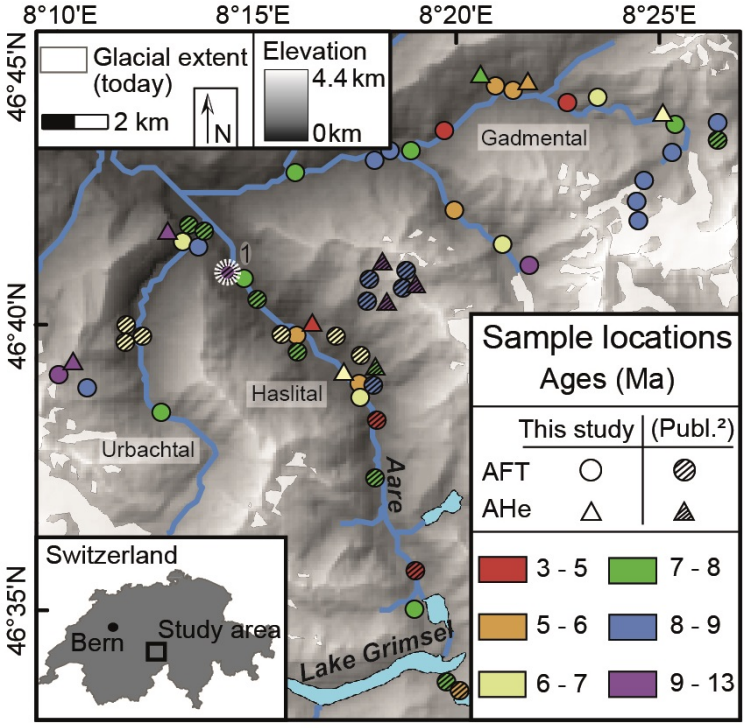

Figure 3.1: Study area with AFT ages and topography based on 90 m SRTM data (USGS, 2006). The main valley running NW-SE following the course of the Aare river is the Haslital, whereas the Urbachtal and the Gadmental are tributary valleys to the west and east. [1]This sample of >12 Ma is excluded from our interpretation, because of conflicting age relations with nearby samples at similar elevations. [2]Published samples are from Michalski and Soom (1990), Vernon et al. (2008, 2009) and M. Rahn (unpubl.).

3.3 Methods

In this study we applied apatite fission track (AFT) on 34 samples and apatite (U-Th-Sm)/He dating (AHe) on 11 samples. The samples derive from bedrocks spatially distributed over the study area. They cover a wide range of elevations (650 – 4100 m) (Fig. 3.2A), which is useful to identify potential elevation-dependencies of thermochronological ages. Where it was possible, confined track lengths were measured to model time-temperature histories (Fig. 3.5 in the Appendix, and see chapter 2). Previous AHe analyses revealed strong zoning of actinides in the apatite crystals from the study area (Vernon et al., 2009), which may influence the interplay between diffusion and ejection of He-particles and may lead to age discrepancies (e.g. Meesters and Dunai, 2002). Our applied thermal modelling is therefore based solely on the AFT data.

Except for one sample, KAW2207 from Michalski and Soom (1990), all samples from the study area were used for an interpolation of an AFT age map (Fig. 3.2B). We excluded this sample, because nearby samples yield consistently younger ages (Fig. 3.1). In total more than 500 AFT ages were used for the interpolation in MATLAB, whereas the vast majority of samples are published AFT ages from outside the study area. In a first step, at each AFT sample location a corresponding zero-age depth was estimated based on a closure temperature of 120°C and individual geothermal gradients. The geothermal gradients were calculated with Fourier's law and the global heat flow database (http://www.heatflow.und.edu/) that reveal heat flow variations between 50 and 60 mW/m^2 in this area. In a second step, based on the zero-age depth, above positioned isolines of same AFT ages were linearly interpolated in a 3D matrix from 0 to 5000 m elevation and a horizontal resolution of 90 m (according to the SRTM). In a third step, the intersection of the age matrix with the DEM resulted in an elevation-corrected AFT age map (details are also described in Glotzbach et al. (2013)). Areas with presumably apatite-free lithologies (e.g. limestones) were excluded.

The dominant cooling ages of the calculated AFT age map (Fig. 3.2B) are between 7 - 8 Ma, resulting in a mean long-term exhumation rate of ~0.5 mm/a. The long-term exhumation rate was calculated with AGE2EDOT (developed by M. Brandon and summarized in Ehlers et al. (2005)), which provides erosion rates due to thermal parameters and corresponding cooling ages. This exhumation rate was used to model surface AFT ages of the study area with PECUBE (cf. Fig. 3.4 in the Appendix) that models surface cooling ages in response to their time-temperature histories (Braun, 2003; Braun et al., 2012). In a first model, a steady-state topography was assumed, and in a second model, the topography changed at 1 Ma from a pre-glacial to the present-day topography. The theoretical pre-glacial topography is a smoothed version of the recent topography calculated by assigning each cell the mean elevation within a ~5 x 5 km square. The smoothed topography was modified by considering

a change in flow direction from the “paleo”-Aare river (Haeuselmann, 2002), crossing the Brünig Pass in the north until Pliocene (Fig. 3.3B). Cave research at Lake Thun (at ~560 m) revealed that the groundwater level was lowered about 1000 m during the Pleistocene (Haeuselmann, 2002), which gives us a minimal elevation of 1500 m for the western border of our hypothesized pre-glacial topography. The resulting pre-glacial topography is characterized by elevations spanning from 1300 to 3500 m, a smaller local relief and a slightly higher mean elevation (2200 m) compared to the recent topography (local relief: 3500 m, mean elevation: 2100 m) (e.g. Sternai et al., 2012). The difference between both modelled surface AFT age maps is used as a proxy for the impact of glacial erosion (pure vertical incision) on surface AFT ages. Any details, according to the samples’ location and used AFT dating methods are described in chapter 2. Required thermal parameters in our PECUBE and AGE2EDOT models are explained in the Appendix from this chapter.

3.4 Results

The thermochronological ages from this study and the published ages are displayed against their corresponding elevation in Figure 3.2A. It is striking that the AHe ages are almost as old as the AFT samples or even older, although in general the AHe system should have a lower closure temperature (e.g. Flowers et al., 2009). Internal zoning of U and Th was the explanation for the observed crossover of AHe and AFT ages within the dataset obtained by Vernon et al. (2009). We could not find any hints for strong internal zoning in our AFT mounts and prints, and therefore we suggest that other mechanisms might also have contributed to this crossover in ages (such as very rapid cooling). Nevertheless, the thermochronological ages show a significant trend with elevation, which differs from a simple uniform trend achieved with constant exhumation and no change in topography. The youngest ages of 4-6 Ma are present at an elevation range of ~1000 – 1600 m and older ages of ~8 Ma between ~600 – 800 m. It is conspicuous that the young AFT ages appear at almost the same elevation as the mean ELA of the maximal ice dilatations during the glaciations. We assume that the position of the ELA during the Last Glacial Maximum (LGM) at 1300 – 1600 m (Ivy-Ochs et al., 2008) can be adopted as a mean ELA for every major glaciation during the Pleistocene. It has been shown for the French Alps that a calculated mean Pleistocene ELA only slightly differs from the ELA during the LGM (e.g. van der Beek and Bourbon, 2008). A slope-elevation analyses discloses slope angles >30° at the ELA level, which are peak values apart from steeper hillslopes around the cirques and arêtes (>3500 m). Maximum hillslope angles at the position of the former ELA are also indicated for other parts of the Alps (e.g. van der Beek and Bourbon, 2008; Robl et al., 2015). Measured confined track lengths vary from 11.3 $\pm$ 1.4 µm to 14.2 $\pm$ 1.3 µm, whereby shorter track lengths are concentrated on the Haslital, indicating a long stay in the partial annealing zone (PAZ) that caused a shortening of tracks (e.g. Gallagher et al., 1998) (Fig. 3.5 in the Appendix).

The spatial distribution of the thermochronological ages is shown in the fission track age map (Fig. 3.2B). Only those interpolated ages within a 2 km radius around samples' locations are shown, because with greater distance the error of the interpolated ages may increase immeasurable. The age map reveals that the youngest ages are located in major valleys, approximately midway up a glaciated valley.

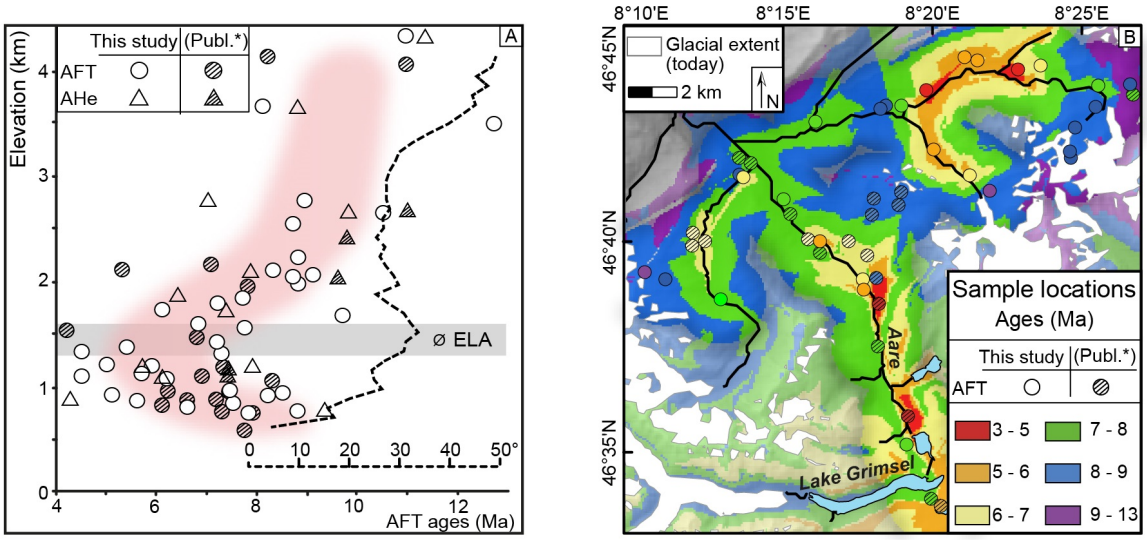

Figure 3.2: **(A)** Diagram showing the relation between AFT and AHe ages and sample elevation. Mean AFT ages at each elevation and their corresponding mean errors are highlighted in red. The ØELA refers to the mean ELA of the LGM (Ivy-Ochs et al., 2008). The dashed line shows mean slope values within 90 m bins from the SRTM data dependent on the elevation. **(B)** Interpolated AFT age map with sample locations and ages. Those areas that comprise lithologies without apatite were not interpolated, and pale areas are outside a 2 km buffer around the sample points, where the interpolation may be inaccurate. *Published samples are from Michalski and Soom (1990); Vernon et al. (2008, 2009) and M. Rahn (unpubl.).

3.5 Discussion

The spatial distribution of AFT and AHe ages and the distinct relation of ages with elevation indicate a spatially non-uniform cooling of rocks. The consistent crescentic age-elevation trend over the whole study area (three differently oriented valleys) suggests the absence of a tectonic influence. Fluid circulation could have not influenced the observed age pattern, because known geothermal fluids are relatively low in temperature (<30°C) and are located outside the areas with the youngest observed ages (Sonney and Vuataz, 2008). Instead, the significant connection of young ages at a certain elevation range (~1000 – 1600 m), which approximates the Pleistocene ELA (Ivy-Ochs et al., 2008), clearly indicates that focused glacial erosion caused this age pattern. The same elevation range is nowadays characterized by the steepest hillslopes, which were interpreted as a relict of accelerated glacial erosion (Robl et al., 2015).

A non-appearance of youngest ages at the lowest point in valleys that is linked to temporary very effective glacial erosion, will only be possible if isotherms approximately follow the pre-glacial topography prior to the glaciations. The study area is located at the northern border of the Aar massif, which extends in SW-NE direction forming a long-wavelength topographic feature perturbing near surface isotherms (Stüwe et al., 1994). As a result isotherm elevations increase towards the southeast as well as the isoage surfaces (Fig. 3.3A). The suggested southeastward propagation of glacial erosion would then cause a non-uniform age-elevation distribution.

We applied 3D thermal-kinematic modelling to investigate if the observed age pattern is just the consequence of a simple increase in local relief. Both models (steady-state and altered topography) provide AFT ages from ~5 Ma in valleys to 11 Ma on ridges (Fig. 3.4 in the Appendix). Deepening of valleys results generally in ~3 to 15% younger ages compared to a scenario with steady-state topography (Fig. 3.3B). The maximum theoretical age difference can be found in the northwestern study area, where we modified the pre-glacial topography to an elevation of 1500 m in accordance with the study of Haeuselmann et al. (2007). The observed deepening is primarily depending on the amount of incision, nevertheless also on the width of the valley. Therefore, the effect is intensified in larger and wider valleys such as the major valley of the Aare river (Fig. 3.3B). This may explain why the increased cooling associated with focused valley incision at ~1 Ma is visible in measured apatite fission track lengths distributions (and derived time-temperature paths) in the Haslital, but is absent in the smaller Gadmental (Fig. 3.5 in the Appendix). This hypothesis correlates to surface models reconstructing the dimensions of glacial erosion based on the underlying topography, whose results demonstrate a high sensitivity of the dimensions of glacial erosion towards the underlying topography (e.g. Pedersen et al., 2014; Herman et al., 2015).

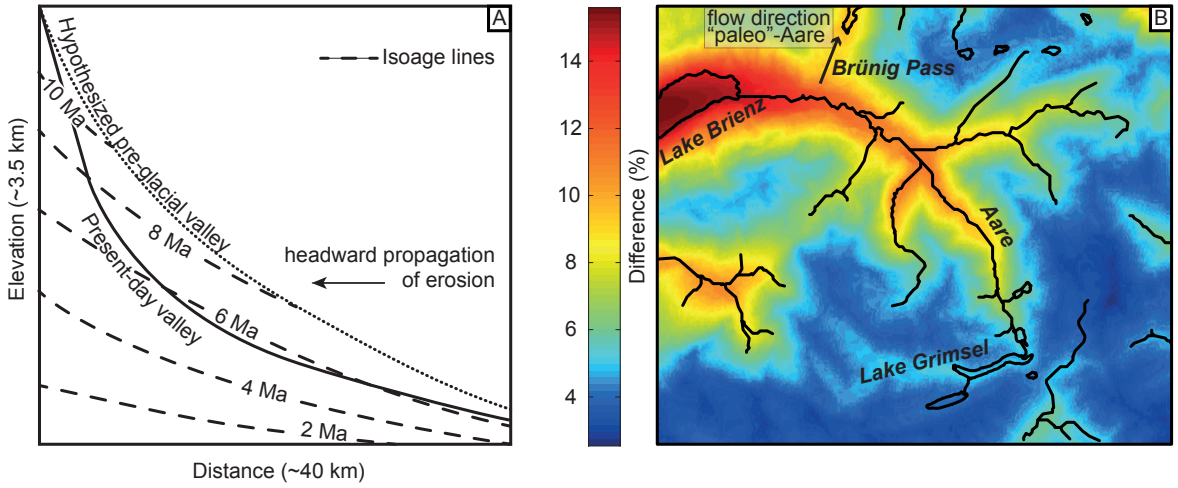

Figure 3.3: (A) Schematic evolution of an Alpine valley during the glaciations. Surfaces of equal AFT ages referred to here as isoage lines, following the courses of isotherms. **(B)** AFT age difference in percent between a topographic steady-state and a steady increase in relief (incising into a smooth pre-glacial topography). Larger differences correspond to younger AFT ages.

The simple modelling fails to predict the very focused area of young ages at elevations around the Pleistocene ELA. Our assumed pre-glacial topography and/or simple steady incision thus can not explain the observed age pattern, however, suggesting that valley evolution was more complex with major erosion at an intermediate range of elevation. Hence, the data require that major valleys, for instance the present Haslital, did not exist in the present form before the onset of major glaciations, which is in accordance with speleological investigations (Haeuselmann et al., 2007). Instead, cooling of rocks must have been less dramatic at the confluence of Haslital, Gadmental and Urbachtal indicated by older thermochronological ages and, therefore, contradicting both surface age models (Fig. 3.2B, 3.3B and Fig. 3.4. in the Appendix).

The youngest ages appearing at or near the ELA leads to the conclusion that the position of the ELA stands for the level with the most effective glacial erosion (Fig. 3.2A). The observed age distribution is very comparable to other studies in which a non-uniform thermochronological age distribution results from valley incision and headward propagation of erosion (e.g. Shuster et al., 2011; Valla et al., 2011). A lowering and rising of the ELA due to many glacial advances and retreats during the Pleistocene caused focused erosion on a wide elevation range that resulted in incision and back-cutting of the glaciated valleys. The position of the present-day ELA still plays an important role in the spatial distribution of glacial erosion below recent glaciations, because most of the sediments are removed nearby the present-day ELA (Ehlers et al., 2015).

The exact sequence of the Pleistocene glacial erosion in the study area, however, remains

a question of debate. Studies in other settings suggest that the first glaciation is mainly responsible for the valley evolution and any following glaciations only enhanced geomorphic leftovers of previous ones (e.g. Shuster, 2005; van der Beek and Bourbon, 2008).

3.6 Conclusions

This study reveals a spatially non-uniform cooling within a basement block, which can not be associated with tectonics, because of a similar age-elevation pattern consistent over the whole study area. A long-term tectonic steady-state was followed by ELA-focused glacial valley incision that produced a non-uniform age distribution. The youngest thermochronological ages appear at a certain elevation range, characterized by the steepest slopes, and approximating the position of the former mean Pleistocene ELA.

It is shown that the effect of glacial erosion on the thermochronological age distribution is depending on the amount of incision and also on the morphology like the width of valleys. Therefore, the current appearance of Alpine valleys is mainly the consequence of glacial erosion and may differ completely from the pre-glacial appearance.

3.7 Appendix

3.7.1 Thermal-kinematic modelling of AFT ages

The 3D thermal-kinematic modeling with PECUBE (Figure 3.4) is based on a mean long-term exhumation rate (0.53 mm/a) that was calculated with AGE2EDOT (Ehlers et al., 2005). Both programs underlie the same thermal parameters:

Thermal parameters:	
Layer depth	35 km
Thermal diffusivity	25 km^2/Ma
Internal heat production	1°C/Ma
Surface temperature	2°C
Temperature at base of layer	700°C
Atmospheric lapse rate	4.6 °C/km
Sea level temperature	12°C

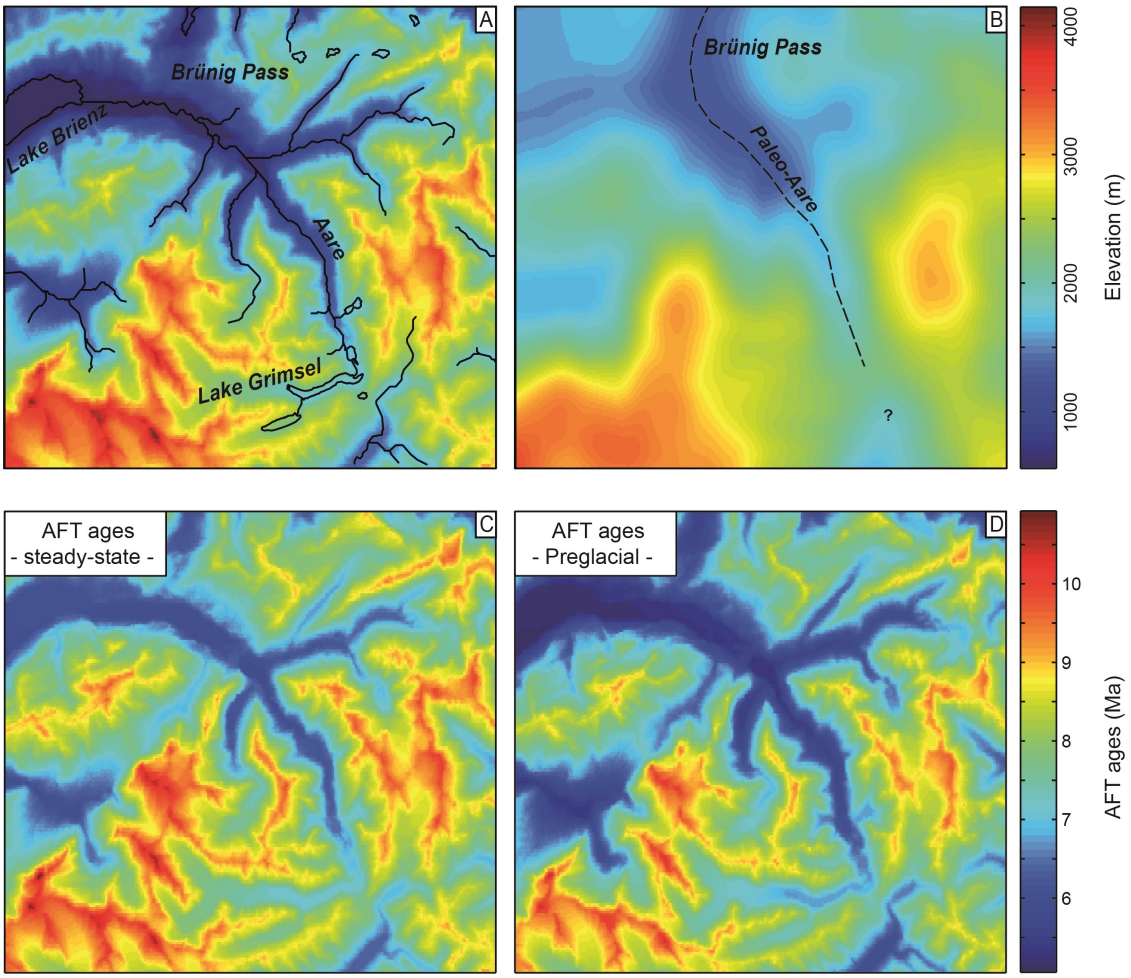

Figure 3.4: **(A)** Recent topography, which was used for steady-state calculation. **(B)** Calculated pre-glacial topography with the Paleo-Aare flowing across the Brünig Pass. **(C)** AFT ages that were estimated with PECUBE, while exhuming a steady-state topography. **(D)** AFT ages estimated with PECUBE, while exhuming the pre-glacial topography.

3.7.2 Thermal modelling

Confined track lengths were measured to model time-temperature histories (Fig. 3.5 and Tab. 2.4 in chapter 2). Previous AHe analyses revealed strong U/Th zoning in apatites from the study area (Vernon et al., 2009), and therefore our modelling is based solely on the AFT data. The inverse thermal modelling was carried out with HeFTy v.1.8.3 (Ketcham, 2005) and the AFT annealing model from Ketcham et al. (2007). Each model is based on mean track lengths and ends at a fixed recent surface temperature of ~7 °C (Fig. 3.5). Further details are described in the section 2.3.3 in chapter 2.

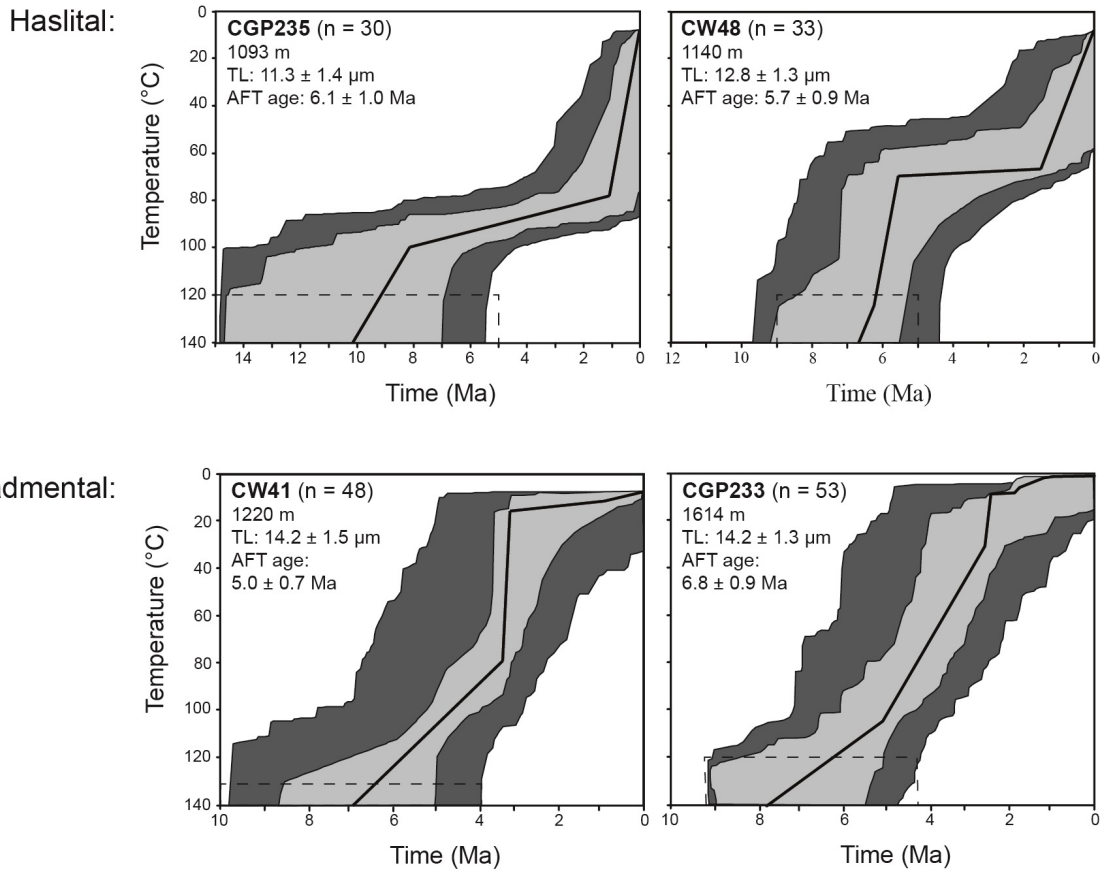

Figure 3.5: HeFTy (Ketcham, 2005) derived time-temperature paths for samples CGP235 and CW48 from the Haslital, and samples CW41 and CGP233 from the Gadmental. Displayed are a best-fit model (black line), acceptable paths (dark grey area) and the good paths (light grey area) (good path and acceptable paths correspond to values of the goodness of fit (GOF) of 0.5 and 0.05). The dashed lines mark the constrain boxes.

References

Albrecht, J. (1994), 'Geologic units of the Aar massif and their pre-Alpine roch associations: a critical review', *Schweiz. Mineral. Petrogr. Mitt.* **74**, 5–27.

Braun, J. (2003), 'Pecube: a new finite-element code to solve the 3D heat transport equation including the effects of a time-varying, finite amplitude surface topography', *Computers & Geosciences* **29**(6), 787–794.

Braun, J., van der Beek, P., Valla, P., Robert, X., Herman, F., Glotzbach, C., Pedersen, V., Perry, C., Simon-Labric, T. and Prigent, C. (2012), 'Quantifying rates of landscape evolution and tectonic processes by thermochronology and numerical modeling of crustal heat transport using PECUBE', *Tectonophysics* **524-525**, 1–28.

Champagnac, J.-D., Schlunegger, F., Norton, K., von Blanckenburg, F., Abbühl, L. M. and Schwab, M. (2009), 'Erosion-driven uplift of the modern Central Alps', *Tectonophysics* **474**(1-2), 236–249.

Densmore, M. S., Ehlers, T. A. and Woodsworth, G. J. (2007), 'Effect of Alpine glaciation on thermochronometer age-elevation profiles', *Geophysical Research Letters* **34**(2).

Egholm, D. L., Nielsen, S. B., Pedersen, V. K. and Lesemann, J.-E. (2009), 'Glacial effects limiting mountain height', *Nature* **460**(7257), 884–887.

Ehlers, T. A., Szameitat, A., Enkelmann, E., Yanites, B. J. and Woodsworth, G. J. (2015), 'Identifying spatial variations in glacial catchment erosion with detrital thermochronology', *Journal of Geophysical Research: Earth Surface* **120**(6), 1023–1039.

Ehlers, T., Chaudhri, T., Kumar, S., Fuller, C., Willett, S., Ketcham, R. A., Brandon, M. T., Belton, D. X., Kohn, B. P., Gleadow, A. J. W., Dunai, T. J. and Fu, F. Q. (2005), 'Computational tools for low-temperature thermochronometer interpretation', *Reviews in Mineralogy and Geochemistry* **58**, 589–622.

Flowers, R. M., Ketcham, R. A., Shuster, D. L. and Farley, K. A. (2009), 'Apatite (U–Th)/He thermochronometry using a radiation damage accumulation and annealing model', *Geochimica et Cosmochimica Acta* **73**(8), 2347–2365.

Fox, M., Herman, F., Kissling, E. and Willett, S. D. (2015), 'Rapid exhumation in the Western Alps driven by slab detachment and glacial erosion', *Geology* **43**, 379–382.

Gallagher, K., Brown, R. and Johnson, C. (1998), 'Fission Track Analysis and its Applications to Geological Problems', *Annual Review of Earth and Planetary Sciences* **26**(1), 519–572.

Glotzbach, C., Bernet, M. and van der Beek, P. (2011b), 'Detrital thermochronology records changing source areas and steady exhumation in the Western European Alps', *Geology* **39**(3), 239–242.

Glotzbach, C., Reinecker, J., Danišík, M., Rahn, M., Frisch, W. and Spiegel, C. (2010), 'Thermal history of the central Gotthard and Aar massifs, European Alps: Evidence for steady state, long-term exhumation', *Journal of Geophysical Research* **115**(F3).

Glotzbach, C., van der Beek, P., Carcaillet, J. and Delunel, R. (2013), 'Deciphering the driving forces of erosion rates on millennial to million-year timescales in glacially impacted landscapes: An example from the Western Alps', *Journal of Geophysical Research: Earth Surface* **118**(3), 1491–1515.

Glotzbach, C., van der Beek, P. and Spiegel, C. (2011a), 'Episodic exhumation and relief growth in the Mont Blanc massif, Western Alps from numerical modelling of thermochronology data', *Earth and Planetary Science Letters* **304**(3-4), 417–430.

Haeuselmann, P. (2002), *Cave Genesis and its relationship to surface processes: Investigations in the Siebenhengste region (BE, Switzerland)*, Unidruckerei Fribourg, Freiburg.

Haeuselmann, P., Granger, D. E., Jeannin, P.-Y. and Lauritzen, S.-E. (2007), 'Abrupt glacial valley incision at 0.8 Ma dated from cave deposits in Switzerland', *Geology* **35**(2), 143–146.

Herman, F., Beyssac, O., Brughelli, M., Lane, S. N., Leprince, S., Adatte, T., Lin, J. Y. Y., Avouac, J.-P. and Cox, S. C. (2015), 'Erosion by an Alpine glacier', *Science* **350**(6257), 193–195.

Herman, F., Seward, D., Valla, P. G., Carter, A., Kohn, B., Willett, S. D. and Ehlers, T. A. (2013), 'Worldwide acceleration of mountain erosion under a cooling climate', *Nature* **504**(7480), 423–426.

Ivy-Ochs, S., Kerschner, H., Reuther, A., Preusser, F., Heine, K., Maisch, M., Kubik, P. W. and Schlüchter, C. (2008), 'Chronology of the last glacial cycle in the European Alps', *Journal of Quarternary Science* **23**, 559–573.

Ketcham, R. A. (2005), 'Forward and Inverse Modeling of Low-Temperature Thermochronometry Data', *Reviews in Mineralogy and Geochemistry* **58**(1), 275–314.

Ketcham, R. A., Carter, A., Donelick, R. A., Barbarand, J. and Hurford, A. J. (2007), 'Improved modeling of fission-track annealing in apatite', *American Mineralogist* **92**(5-6), 799–810.

MacGregor, K., Anderson, R., Anderson, S. and Waddington, E. (2000), 'Numerical simulations of glacial-valley longitudinal profile evolution', *Geology* **28**(11), 1031.

Meesters, A. and Dunai, T. (2002), 'Solving the production–diffusion equation for finite diffusion domains of various shapes: Part I. Implications for low-temperature (U–Th)/He thermochronology', *Chemical Geology* **186**(3-4), 333–344.

Michalski, I. and Soom, M. (1990), 'The Alpine thermo-tectonic evolution of the Aar and Gotthard massifs, Central Switzerland: fission track ages on zircon and apatite and K-Ar mica ages', *Schweiz. Mineral. Petrogr. Mitt.* (70), 373–387.

Pedersen, V. K., Huismans, R. S., Herman, F. and Egholm, D. L. (2014), 'Controls of initial topography on temporal and spatial patterns of glacial erosion', *Geomorphology* **223**, 96–116.

Penck, A. (1905), 'Glacial Feautures in the Surface of the Alps', *The Journal of Geology* **13**(1), 1–19.

Robl, J., Prasicek, G., Hergarten, S. and Stüwe, K. (2015), 'Alpine topography in the light of tectonic uplift and glaciation', *Global and Planetary Change* **127**, 34–49.

Schlatter, A., Schneider, D., Geiger, A. and Kahle, H.-G. (2005), 'Recent vertical movements from precise levelling in the vicinity of the city of Basel, Switzerland', *International Journal of Earth Sciences* **94**(4), 507–514.

Schlüchter, C. (2004), The Swiss glacial record: a schematic summary, *in* P. L. Gibbard and Ehlers J., eds, 'Quaternary Glaciations: Extent and Chronology Part I: Europe', Elsevier, London.

Schmid, S. M., Pfiffner O. A., Froitzheim N., Schönborn G. and Kissling E. (1996), 'Geophysical - geological transect and tectonic evolution of the Swiss-Italian Alps', *Tectonics* **15**, 1036–1064.

Shuster, D. L. (2005), 'Rapid Glacial Erosion at 1.8 Ma Revealed by 4He/3He Thermochronometry', *Science* **310**(5754), 1668–1670.

Shuster, D. L., Cuffey, K. M., Sanders, J. W. and Balco, G. (2011), 'Thermochronometry Reveals Headward Propagation of Erosion in an Alpine Landscape', *Science* **332**(6025), 84–88.

Sonney, R. and Vuataz, F.-D. (2008), 'Properties of geothermal fluids in Switzerland: A new interactive database', *Geothermics* **37**(5), 496–509.

Sternai, P., Herman, F., Champagnac, J.-D., Fox, M., Salcher, B. and Willett, S. D. (2012), 'Pre-glacial topography of the European Alps', *Geology* **40**(12), 1067–1070.

Stüwe, K., White, L. and Brown, R. (1994), 'The influence of eroding topography on steady-state isotherms. Application to fission track analysis', *Earth and Planetary Science Letters* **124**(1-4), 63–74.

Valla, P. G., van der Beek, P. A. and Braun, J. (2011), 'Rethinking low-temperature thermochronology data sampling strategies for quantification of denudation and relief histories: A case study in the French western Alps', *Earth and Planetary Science Letters* **307**(3-4), 309–322.

van der Beek, P. and Bourbon, P. (2008), 'A quantification of the glacial imprint on relief development in the French western Alps', *Geomorphology* **97**(1-2), 52–72.

Vernon, A. J., van der Beek, P. A., Sinclair, H. D., Persano, C., Foeken, J. and Stuart, F. M. (2009), 'Variable late Neogene exhumation of the central European Alps: Low-temperature thermochronology from the Aar Massif, Switzerland, and the Lepontine Dome, Italy', *Tectonics* **28**(5).

Vernon, A., van der Beek, P., Sinclair, H. and Rahn, M. (2008), 'Increase in late Neogene denudation of the European Alps confirmed by analysis of a fission-track thermochronology database', *Earth and Planetary Science Letters* **270**(3-4), 316–329.

Wittmann, H., von Blanckenburg, F., Kruesmann, T., Norton, K. P. and Kubik, P. W. (2007), 'Relation between rock uplift and denudation from cosmogenic nuclides in river sediment in the Central Alps of Switzerland', *Journal of Geophysical Research* **112**(F4).

4 Non-uniform erosion in Alpine catchments lead to bias in cosmogenically derived denudation rates

4.1 Abstract

The estimation of spatially and temporally averaged catchment-wide denudation rates in an Alpine setting remains a challenge due to an often non-representative sediment load, because of highly variable erosion processes. Here we present a new approach of combining detrital thermochronology and ^{10}Be concentrations of fluvial sediment. This approach takes into account spatial variations in erosion and estimates correct catchment-wide denudation rates. Detrital thermochronology provides the elevation range of which the sediments are sourced from. The provenance is used to improve catchment-wide denudation estimates of seven stream sediment samples from the Central Alps (Switzerland). Developed erosion probability maps indicate two peak elevations, 900 - 1600 m and 2800 - 3400 m, at which the erosion in this study area is at its maximum. According to geomorphic analysis, glacial erosion at the equilibrium line of altitude (ELA) below present-day glaciers and fluvial erosion around the former ELAs of the maximal extent of glaciers during the Pleistocene mainly control the provenance of present-day stream sediments. Corresponding denudation rates show that glacial erosion is more effective than fluvial erosion. Local geomorphic characteristics and the residence time of sediments within the catchment constrain if the analysed stream sediments derive either from fluvial or from glacial erosion. This new approach, therefore, provides a method to estimate reliable catchment-wide denudation rates in a setting not really suitable for this technique. Additionally, the distribution and the effectiveness of erosional processes in the catchments can be identified.

4.2 Introduction

Estimating catchment-wide denudation rates with in-situ produced cosmogenic ^{10}Be is a widely applied technique in partly glaciated mountain belts such as the Alps (e.g. Wittmann et al., 2007; Norton and Vanacker, 2009; Norton et al., 2010, 2011; Glotzbach et al., 2013). Measured in-situ produced ^{10}Be concentrations in quartz of fluvial sediment are supposed to represent the average denudation rates of the sample's upstream catchment. This method relies on the pioneer work about nuclide production rates by Lal (1991) and the enhancement of using fluvial sediments (e.g. Brown et al., 1995; Bierman and Steig, 1996; Granger et al., 1996). The calculation of catchment-wide denudation rates is based on the primary assumption that sediments are naturally transported by the fluvial network and mixed homogeneously in the sediment load. Therefore, quartz grains of stream sediment samples are assumed to represent the spatially averaged ^{10}Be content from the entire catchment area (Bierman and Steig, 1996; von Blanckenburg, 2005). The denudation rates refer to the time the quartz spent in the uppermost few meters below the surface, the depth that is typically reached by the majority of cosmogenic rays, because this is assumed to be much longer than the time the quartz grain is transported by the fluvial network (Bierman and Steig, 1996). Catchment-wide denudation rates can integrate a timescale of 10^2 to 10^4 years in areas with denudation rates of ~ 6 mm/a to 0.06 mm/a (von Blanckenburg, 2005).

The attenuation of cosmic rays and hence the in-situ production of cosmogenic nuclides at surface depends on latitude and elevation (Lal, 1991; Stone, 2000), whereas a shielding due to topography, glaciers and snow reduces the nuclide production (e.g. Dunne et al., 1999; Dunai, 2010). Consequently, if the majority of sediments within the fluvial sample contains of previous shielded material, the assumption of spatially and temporally averaged ^{10}Be concentrations in stream sediments may be invalid and the measured nuclide concentration will yield overestimated denudation rates (e.g. Kober et al., 2012; Delunel et al., 2014). Erosion processes that abruptly contribute a large amount of (possibly previously shielded) sediments into the fluvial system (e.g. glacial erosion, debris-flows) may lead to stream sediment samples that are not representative for the catchment. Estimating catchment-wide denudation rates in highly glaciated, mountainous areas, where an increased incidence of the above mentioned processes can occur, may therefore lead to problems in the determination of accurate denudation rates (e.g. Niemi et al., 2005; Binnie et al., 2006; Delunel et al., 2010, 2014; Savi et al., 2014, 2015). Generally, there is a possibility to avoid the effect of non-representative sediments by choosing catchments of reasonable size ($\geq$ 100 km²), because with increasing catchment size the sediments are better mixed (e.g. Niemi et al., 2005; Binnie et al., 2006; Wittmann et al., 2007; Savi et al., 2014). Another option is to decipher different sediment supply mechanisms and the origin of sediments within the studied catchment by

measuring in-situ produced ^{10}Be nuclide concentrations on various detrital materials and/or in additional upstream fluvial material (e.g. Delunel et al., 2014; Savi et al., 2014).
Here, we present a new approach to accurately estimate catchment-wide denudation rates in a high mountain setting by combining the ^{10}Be nuclide concentration in quartz with the thermochronological age distribution in apatites from the same stream sediment samples. The detrital thermochronological ages of the apatites are used to determine the provenance and the spatial variations of the erosional pattern in the catchments, as already successfully applied in various studies (e.g. Brewer et al., 2003; Ruhl and Hodges, 2005; Stock et al., 2006; Vermeesch, 2007; McPhillips and Brandon, 2010; Avdeev et al., 2011; Tranel et al., 2011; Glotzbach et al., 2013; Ehlers et al., 2015; Fox et al., 2015). The provenance of apatites is transferred into an erosion probability map, which in turn is considered for the calculation of cosmogenic ^{10}Be-derived catchment-wide denudation rates.
The fluvial samples in this study derive from seven valleys, comprising different catchment sizes in the Bernese Alps in Switzerland. The study area is characterized by a high local relief (peaks up to ~ 4000 m) and several glaciers (e.g. Aare glaciers) (Fig. 4.1 and 4.2). Almost everywhere in the Central Alps the landscape finds itself in a transient geomorphic state (e.g. Hinderer et al., 2013; Schlunegger and Norton, 2013) and recent surface processes contributes to achieve a new geomorphic steady-state (e.g. Hinderer, 2001; Wittmann et al., 2007; Champagnac et al., 2009; Norton et al., 2010, 2011; Glotzbach et al., 2013). Therefore, on catchment scale, hillslope processes are still related to the erosive effects of glaciers from the last glacial maximum (LGM) constrained by the position of the equilibrium line of altitude (ELA), especially from the LGM glaciers. Schlunegger and Norton (2013) and Salcher et al. (2014) suggest that the landscape below the ELA of the LGM is dominated by fluvial processes and, instead, the landscape above the ELA of the LGM is dominated by the impact of glacial erosion of the present and past. Both mechanisms have been suggested to control catchment-wide denudation rates in the Alps.
The complex interaction of fluvial and glacial processes and in-frequently occurring large mass wasting processes may cause temporal and spatial variations in erosion that may lead to non-representative sediments (e.g. Wittmann et al., 2007; Kober et al., 2012). The presented new approach is supposed to be capable to unravel spatial variations in erosion rates, accurately estimate denudation rates and identify the importance of the different erosional regimes and processes (e.g. glacial erosion, frost-cracking).

4.3 Study area

4.3.1 Tectonic evolution

A convergence between the European and African continent resulted in nappe stacking, crustal thickening and finally in tectonic uplift of the Alps (since Eocene, 34 Ma) (e.g. Schmid et al., 2004). Geologically, the Alps can be divided into three major tectonic units; Helvetic, Penninic, and Austroalpine - South Alpine unit (e.g. Schmid et al., 1996). The Helvetic and the Austroalpine - South Alpine units represent the European and Adriatic plate, respectively, while the Penninic unit comprises the sedimentary cover of the Briançonnais micro-continent with its surrounding ocean basins (e.g. Schmid et al., 1996, 2004).
The Helvetic unit, which is the dominating unit in the study area (Fig. 4.1), consists of basement rocks (e.g. Aar massif and Gotthard massif) and a mainly Mesozoic-Cenozoic sedimentary cover (mostly limestone and minor sandstone). This study focuses on the Aar massif, which outcrops in Switzerland. The basement rocks of the Aar massif are composed of a Variscan granite that intruded during the Variscan orogeny into Pre-Variscan basement units (e.g. Schaltegger, 1990; Albrecht, 1994). Prior the doming and exhumation of the Aar massif, the Helvetic nappes (Mesozoic-Cenozoic sedimentary cover) were thrust towards the north. During doming, the overlying Helvetic nappes and the parautochthonous unit built an antiformal stack that forms the near-vertical north faces of Eiger, Mönch and Jungfrau (Fig. 4.2) (e.g. Herwegh and Pfiffner, 2005; Pfiffner, 2009).
The recent topography of the Alps is the result of the interaction between Neogene to present-day uplift and erosional processes (e.g. Pfiffner and Kühni, 2001; Vernon et al., 2008; Valla et al., 2010; Glotzbach et al., 2011), with a dominant role of major Quaternary glaciations (e.g. Kelly et al., 2006; Haeuselmann et al., 2007). The Swiss Alps are assumed to be no longer tectonically active (e.g. Champagnac et al., 2009) and the recent uplift derived from repeated precise levelling (e.g. Calais et al., 2002; Schlatter et al., 2005) correlates well with ^{10}Be-derived denudation rates (Wittmann et al., 2007).

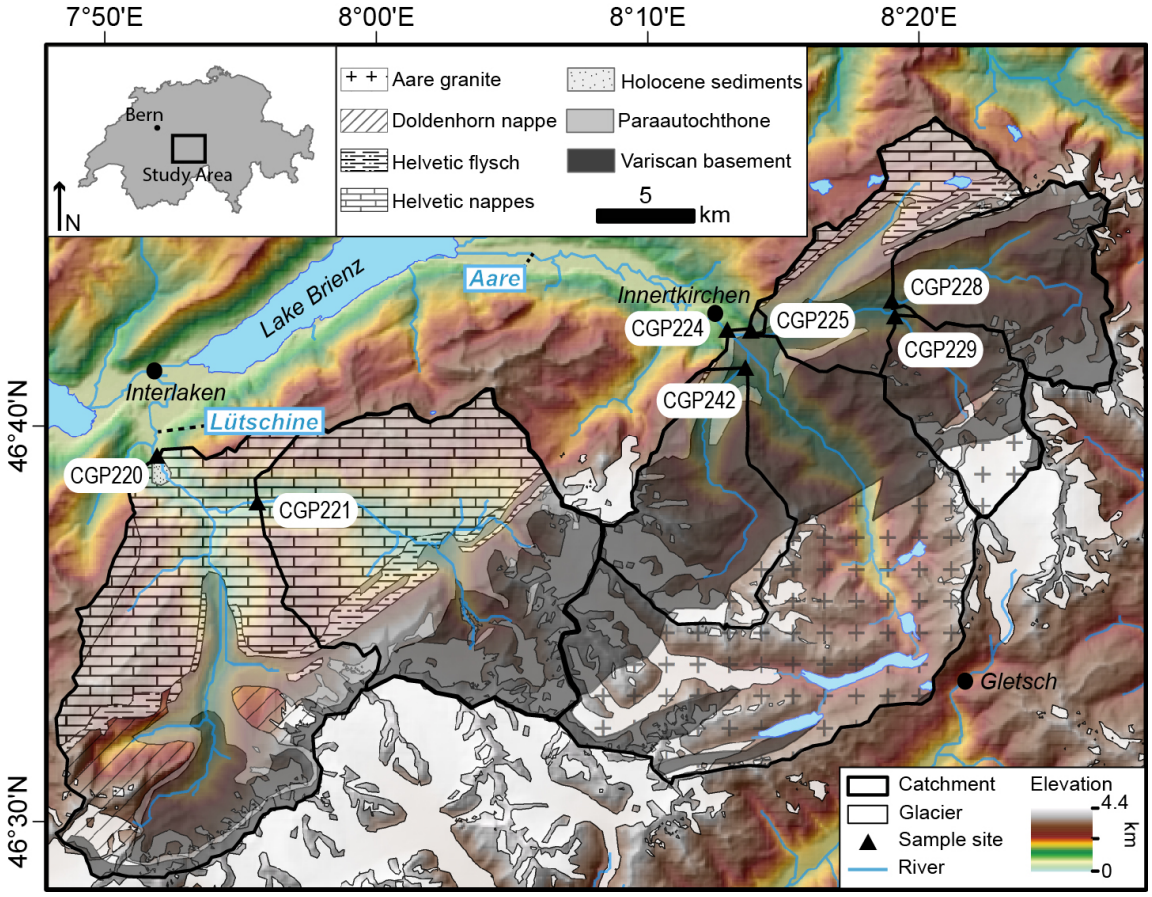

Figure 4.1: Topographic map of the study area overlain by the geologic setting (Tectonic map of Switzerland, 1: 500 000), based on 90 m SRTM data. The stream sediment samples (CGPXXX) from the drainage areas of the Lütschine (west) and the Aare (east) are presented with their corresponding catchments.

4.3.2 Geomorphic setting

The study area is part of the Central Alps in Switzerland and compromises the Berner Oberland, which is a high mountain area (up to 4000 m) southeast of Bern (Fig. 4.1). The higher valleys are glaciated and are home to the biggest glaciers in Europe, e.g. the Aare Glaciers and Aletsch Glaciers (Fig. 4.2). The sampled streams (Fig. 4.1), the Aare and the Lütschine, have their sources in the study area and both flowing into Lake Brienz in the north.

Most of the present-day geomorphic features in the Alps resulted from processes related to multiple Quaternary glaciations (e.g. van der Beek and Bourbon, 2008; Sternai et al., 2012). The present transient geomorphic state that affects the erosional processes is supposed to be a consequence of the last glacial maximum (LGM) (e.g. Ivy-Ochs et al., 2008; Schlunegger and Norton, 2013). The last glacial period took place between the interglacials Eem and Holocene about 115 to 11 ka ago (Schlüchter, 2004) and had its maximum ice dilatation

between 24 to 21 ka. During that period the ice spread towards the foreland (Ivy-Ochs et al., 2008). The deglaciation started 21 ka ago and had been completed since 18 ka in the inner Alpine valleys (e.g. Kelly et al., 2006; Dielforder and Hetzel, 2014). After the LGM, several temporary glacial readvances took place, but they have never reached the foreland again (e.g. Ivy-Ochs et al., 2006; Schimmelpfennig et al., 2014). The leftovers of moraines, which can be found in the main valleys of the study area, are attached to these post-LGM glacial readvances (Hantke and Wagner, 2005). The youngest glacial advance occurred during the Little Ice Age (LIA), which took place between the 14^{th} and 19^{th} Century AD (e.g. Holzhauser et al., 2005), but the ice extent of the LIA remained behind post-LGM glacial readvances (Ivy-Ochs et al., 2006; Schimmelpfennig et al., 2014).

During the ice ages the dominant mechanism of denudation changed from fluvial to glacial. The efficiency of denudation was strengthened and increased the local relief by valley widening and overdeepening of valley floors (e.g. Whipple and Tucker, 1999; Haeuselmann et al., 2007). Therefore, with the ice retreat, several topographic features of Quaternary glaciations became visible, e.g. trough valleys, hanging valleys, moraines, roches moutonées or cirques (recently glaciated or not) (e.g. Wagner, 2002; Hantke and Wagner, 2005). Visible glacial striations from the LGM and LIA glaciers reveal areas that were unaffected by erosion over several 10 ka. Steep sidewalls, arêtes and flat valley floors of glacial trough valleys can clearly be seen on the slope map from the study area (Fig. 4.2).

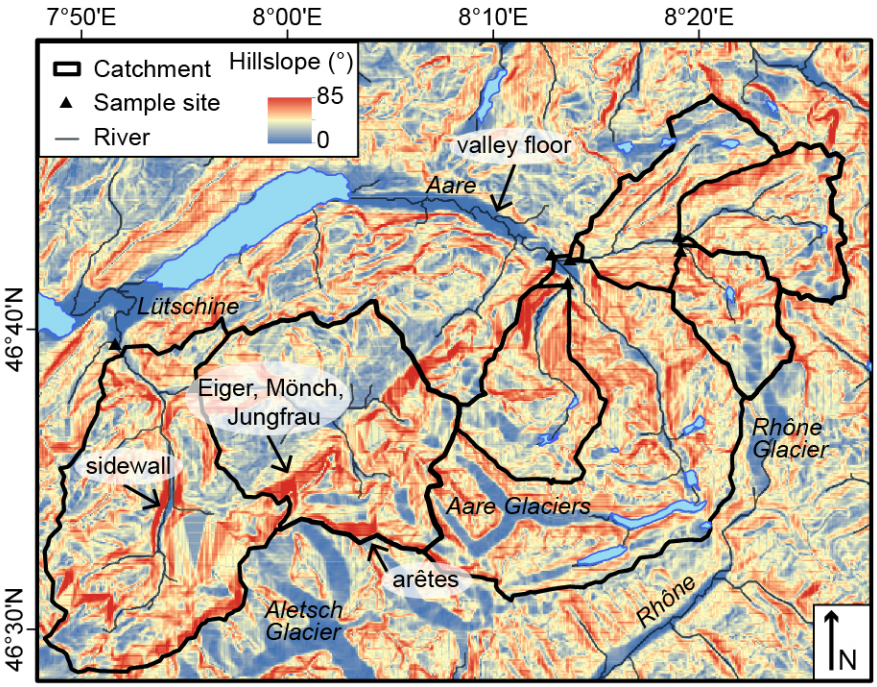

Figure 4.2: Slope map of the study area that was calculated in ArcGIS (90 m resolution) indicating characteristics of extensive glaciations.

4.4 Methods

Stream sediment samples were used to estimate cosmogenic ^{10}Be concentrations on the one hand and their apatite fission track (AFT) age distributions on the other hand. In combination with a surface AFT age map (interpolation details are described in chapter 3) we determined the provenance of detrital apatites. In small catchments AFT ages may solely vary with elevation (e.g. Brewer et al., 2003), but larger catchments like in this study are characterized by spatial differences in long-term exhumation rates. This circumstance requires to interpolate a dense AFT age grid (e.g. Glotzbach et al., 2013) instead of using the basin hypsometry for provenance analysis (increasing elevation = increasing AFT ages), as already applied in several studies (e.g. Ruhl and Hodges, 2005; Vermeesch, 2007; Avdeev et al., 2011).
The estimation of the position where the apatite grains were eroded from was resolved by a statistical comparison of measured AFT age cumulative density functions (CDF) with modelled CDFs based on interpolated surface AFT ages. The statistical comparison of CDFs was applied to approximate iteratively from uniform to non-uniform the distribution of erosion in the catchments. A similar approach was already successfully used to quantify the distribution of erosion within catchments in similar settings in the Sierra Nevada, the Alps and also in the Himalaya (e.g. Brewer et al., 2003; Ruhl and Hodges, 2005; Stock et al., 2006; Vermeesch, 2007; McPhillips and Brandon, 2010; Avdeev et al., 2011; Tranel et al., 2011; Glotzbach et al., 2013; Ehlers et al., 2015; Fox et al., 2015). In a final step, the provenances of sampled stream sediments were used to re-calculate catchment-wide denudation rates and to create erosion maps.

Table 4.1: Geomorphic data

Sample	Sample altitude (m a.s.l.)	UTM coordinates X(m)	UTM coordinates Y(m)	Area (cryst.*) (km²)	Mean elevation (m)	Relief (m)	Mean hillslope (°)	Glaciated (%)
CGP220	599	413473	5167209	364 (87)	2666	3460	28	12
CGP221	690	418169	5165267	178 (50)	2795	3327	26	15
CGP224/ CW6	720	440169	5173359	461 (386)	2304	3532	28	17
CGP225	640	440944	5173055	171 (116)	2136	2791	28	16
CGP228	934	448372	5174584	66 (56)	2125	2424	29	16
CGP229	933	448147	5173961	45 (45)	2494	2395	27	36
CGP242	791	440805	5171439	70 (59)	2414	2809	29	23

*Area with outcropping lithologies containing quartz and apatite (Variscan basement, Aar granite, Parautochthone)

4.4.1 Sampling

The fluvial sediment samples, 2-3 kg each, derive from active channels or sand bars. Five samples were collected from the Aare river and their tributary catchments and two samples derive from the Lütschine river and sub-catchment (Fig. 4.1). The samples were taken at elevations of 599 – 934 m and upstream catchment sizes vary between 45 – 461 km² (Tab. 4.1 and Fig. 4.1). Every catchment was nearly completely covered by ice during the Pleistocene glacial advances (e.g. Coutterand, 2010) and is still partially glaciated. The Aare drainage basin mainly consists of crystalline lithologies with apatite- and quartz-bearing rocks, whereas the drainage area of the Lütschine is predominantly covered by limestones from the Helvetic unit, presumably free from apatite and quartz (Fig. 4.1).
The loose stream sediment samples were sieved to a grain size fraction <500 µm and apatite and quartz were separated using standard gravimetric and magnetic techniques. In the particular case of sample CGP224 and CW6, we took two different samples at the same location in the years 2010 and 2013. Sample CGP224 did not contain enough measureable ^{10}Be, that is why another sample (CW6) needed to be taken. Therefore, we counted the apatites from the original sample CGP224 from 2010 and measured the ^{10}Be content of the sample CW6 from 2013. In order to simplify, we will only name the sample CGP224 in the following text.

4.4.2 Detrital thermochronology

4.4.2.1 Analytical procedure

For fission track dating, the apatites were mounted in Araldite2020 and etched with 5M HNO_3 at 20°C for 20 s. After irradiation with thermal neutrons at the FRM-II reactor facility in Garching (TU München), the mica external detectors were etched to reveal induced tracks using 40% HF at 20°C for 30 min. A sufficient reproduction of the AFT age distribution within the detrital samples was ensured by counting 50 to 100 grains per sample. The fission track analyses was carried out using an Olympus BX51 microscope. The dating of the apatites is based on the external detector method (Naeser, 1967; Gleadow, 1981) and the zeta calibration approach (Hurford and Green, 1982, 1983).

4.4.2.2 Iterative formation of erosion probability maps

The calculation of catchments' individual erosion probability maps is based on measured AFT age distributions, their 1σ error and an interpolated AFT age map (cf. Fig. 4.10 in the Appendix). The AFT age map provides a surface AFT age for each cell within the samples'

upstream catchment area (grid resolution 90 m). The corresponding interpolation error was calculated by bootstrapping of the input dataset of the interpolation, which consists of >500 published AFT ages from the European Alps (cf. Vernon et al., 2008). The resulting statistics were again interpolated on a map (cf. Fig. 4.11 in the Appendix), at which the maximum interpolation error (difference between observed and modelled age) is ~110%. Note that AFT ages were only interpolated for an area with outcropping crystalline lithologies (Aar granite, Variscan basement and Paraautochthone) and consequently limiting the extent of the erosion maps (Fig. 4.9).

To simplify the inversion problem, we assumed that erosional processes vary mainly with elevation and that pure lateral variations in erosion do not occur within individual catchments. The elevation range of the apatite-bearing lithologies of each catchment was sampled for every 100 m. Initially, it was assumed that every cell within the catchment erodes with the same probability, thus each cell could have contributed an apatite grain to the stream sediment sample. The calculation of ^{10}Be-derived catchment-wide denudation rates is usually based on the assumption of an uniform distribution of erosion within the catchments.

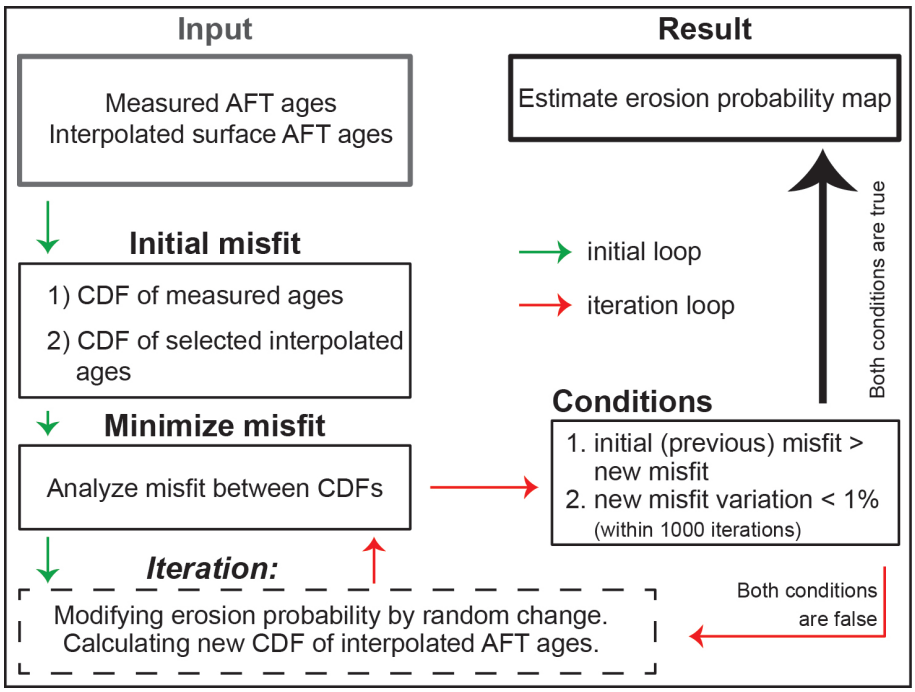

Figure 4.3: Flowchart of an iterative method to estimate an erosion probability map. The calculation starts with the determination of an initial misfit, which should be minimized through several iterations of modifying the erosion probability.

The flowchart in Figure 4.3 illustrates the following description of the procedure that was applied for every sample. The calculation began with the generation of a CDF of measured AFT ages and errors. This was obtained by calculating the cumulative sum of all single

grain age distributions (assumed to be normally distributed). The generation of a synthetic AFT dataset deviates from previously introduced approaches from Vermeesch (2007) and Glotzbach et al. (2013), by considering the interpolation error of 110%. The synthetic AFT dataset consists of as many synthetic grains as counted grains in the corresponding sample. The selection of interpolated ages depends on the erosion probability of each cell, which was uniform in the initial case and has been adjusted to fit the observed data during the inversion. Minimization of the misfit between measured and synthetic CDFs (Fig. 4.4B) was done by fitting the erosion probability within an iterative approach (Fig. 4.3). During each run, the probability of a randomly selected elevation node was changed to a random number within a normal distribution with a mean value corresponding to the previously used probability (P_e) and a standard deviation of 0.1. Based on this new probability, ages for a new synthetic CDF were selected from the interpolated age file, as explained above.

If the misfit between measured and synthetic CDFs exceeds the initial (or previous) misfit, the modified erosion probability will be discarded. If the new misfit is lower than the previous one, the new erosion probability will be taken for the next run. A penalty function (PF) was used to smooth the resulting elevation-dependent erosion curve:

$$PF = a \cdot sum(P_e') + b \cdot sum(P_e''), \tag{4.1}$$

where a and b are dimensionless weighting coefficients. These coefficients were set to values between 0.0001 and 0.003, resulting in smooth erosion probability vs. elevation curves (Fig. 4.4A). The inversion ran until the difference between new misfits was lower than 1% within 1000 repetitions. Minimizing the misfits of our samples required 10 000 to 17 000 repetitions of the inversion.

The new erosion probability of every thousandth iteration was plotted against the corresponding elevation (Fig. 4.4A). The erosion probability of the lowest misfit was then used to interpolate an erosion probability map of the catchment.

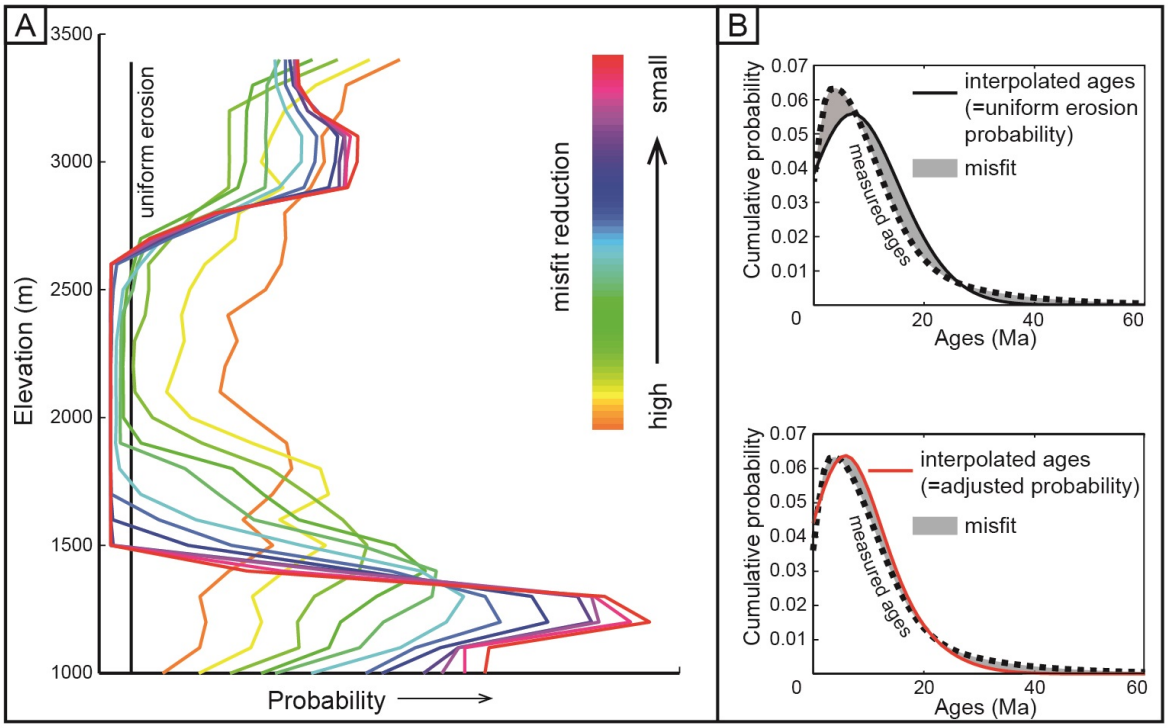

Figure 4.4: **(A, B)** An example of how the misfit is minimized from 0.24 (black lines = uniform erosion) to 0.15 (red lines = adjusted probability) for sample CGP228 (Tab. 4.1). The misfit is the difference between measured and interpolated AFT ages. **(A)** Every line represents a modified erosion probability and the corresponding elevation after thousand model iterations. **(B)** The CDF plots demonstrate the misfit between the unchanged CDF of measured ages (dashed lines) and initial synthetic CDF of interpolated ages (uniform erosion = black line) as well as the final misfit between measured ages and the synthetic CDF based on the adjusted erosion probability (red line).

4.4.3 ^{10}Be catchment-wide denudation rates

4.4.3.1 Measurement of ^{10}Be

The quartz was chemically cleaned for four times with diluted HF-HNO_3 to remove the meteoric component of ^{10}Be; following the protocol of Kohl and Nishiizumi (1992). Before dissolving the samples, the purity of the quartz was checked with ICP-OES analyses. After cleaning, sample weights were reduced to 20-38 g. In the next step 0.3 g of a ”Be-carrier” (~1000 ppm Be in 2% HCl; Scharlau) was added to each sample to obtain a fixed content of the stable isotope ^{9}Be in the sample for measurability at a mass spectrometry facility (e.g. Dunai, 2010). After that, the samples plus carrier were completely dissolved in ~40% HF at 100°C. The ^{10}Be was separated with anion and cation exchange columns and precipitated as a $Be(OH)_2$ aggregate. The dried precipitation was oxidized to BeO and pressed in targets for the Tandem Accelerator Mass Spectrometry (AMS) facility of the ETH Zurich. At the ETH Zurich the measurement was normalized to the secondary standard S2007N, which is

standardized to the primary standard ICN 01-5-1 (Nishiizumi et al., 2007; Kubik and Christl, 2010).

4.4.3.2 Calculation of catchment-wide denudation rates

^{10}Be can be produced meteoric or in-situ and has a half-life of 1.387 $\pm$ 0.012 Ma (Chmeleff et al., 2010; Korschinek et al., 2010), whereas only few particles with enough energy to activate in-situ decay reactions reach the Earth's surface (Gosse and Phillips, 2001). In-situ ^{10}Be mainly results from the decay of oxygen and partly from elements like Mg, Al, Si and Ca (Lal, 1991). The decay is activated through secondary cosmic rays (Lal and Peters, 1967), mainly high-energy spallation and partly negative muon capture and fast muons. The secondary cosmic rays decrease exponential with depth from surface, as well as the production rates (Lal, 1991). The effective cosmic ray attenuation length is 160 g/cm^2 (Balco et al., 2008), which is equivalent to approximately 60 cm of rock with a density of 2.7 g/cm^3. In case of steady-state between cosmogenic nuclide production and loss through denudation and radioactive decay, the nuclide concentration is inverse proportional to the denudation rates, and can be described as (Lal, 1991):

$$c = P_0/(\lambda + \rho\epsilon/\Delta), \tag{4.2}$$

where c is the concentration of in situ-produced cosmogenic ^{10}Be (at/g$_{\text{Quartz}}$), P_0 the production rate at surface (at/g$_{\text{Quartz}}$·a), λ the ^{10}Be decay constant (1/a), ρ the rock density (g/cm^3), ϵ the denudation rate (cm/a) and Δ the mean cosmic ray attenuation length (g/cm^2).
In high-relief Alpine catchments with permanent ice cover, the cosmic rays may be shielded. Therefore, a shielding factor was included that consists of three components: topographic shielding (Dunne et al., 1999), glacier shielding and snow shielding (e.g. Schildgen et al., 2005; Wittmann et al., 2007). The topographic shielding describes the difference of cosmic ray flux between unshielded mountain peaks and highly shielded valley bottoms (Dunne et al., 1999). It relies on a raster, where each cell has a value between 0 for completely shielded against cosmic ray flux and 1 for no shielding (S^t).
The glacier shielding (S^g) is based on the assumption that below glaciers no cosmogenic nuclides are produced and previously produced nuclides will be reset to zero. There is the possibility that recently exposed quartz grains from glaciers might have a small nuclide concentration, but measured nuclide concentrations at glacier outlets are low enough to simply assume a nuclide concentration of zero (Wittmann et al., 2007; Dielforder and Hetzel, 2014). The extent of Alpine glaciers varied temporally during the last thousands of years, therefore we suppose that the recent extent reflects a good average of this variation (Hormes et al.,

2001). Hence, it is assumed that no cosmogenic nuclides are produced below recent glaciers, whose extent is provided by www.swisstopo.ch.
The snow shielding (S^s) describes the permanent snow cover, which might reduce the yearly nuclide production too (e.g. Dunai, 2010). The variable snow cover was estimated with mean snow cover values from Switzerland over the years 1983 - 2002 (Auer, 2003). The correction factor was calculated considering only a high-energy spallation production (neglecting muonic production) in the depth-dependent production rate formalism of Schaller et al. (2002). Therefore, the snow thickness from Auer (2003) and a characteristic density of old and compacted snow (~0.3 g/cm^3) were used (e.g. Roebber et al., 2003; Ware et al., 2006), following Wittmann et al. (2007).
In our study the shielding factor also accounts for the lithology, assuming that the crystalline rocks (Aar granite, Variscan basement and Parautochthone, Fig. 4.1) exclusively delivered quartz in the analysed samples (L). The product of the shielding components resulted in an individual factor for each cell S_i (cf. Delunel et al., 2010):

$$S_i = (S_i^t) \cdot (S_i^g) \cdot (S_i^s) \cdot (L_i), \tag{4.3}$$

Based on the cells' individual shielding factors, we determined a nuclide production rate for every cell and averaged it afterwards (P_s):

$$P_s = \frac{1}{n} \cdot \sum_{i=1}^{n} (P_i^{ref} \cdot S_i), \tag{4.4}$$

The production rate itself was scaled to every cells' location within each catchment (P^{ref}), following Lal (1991) and (Stone, 2000), based on a reference production rate of 4.01 at/g·a at sea level and high latitude (>60°) (Borchers et al., 2016). The nuclide production provoked by muons was considered for fast muons after Heisinger et al. (2002a) and for negative muon capture after Heisinger et al. (2002b). Results following this standard denudation rate calculation procedure are listed in Tab. 4.5.

4.4.4 Modifying catchment-wide denudation rates

Hydraulic sorting influences the stream sediment composition and should be taken into account for the interpretation of detrital thermochronological data (e.g. Malusà et al., 2016). The major parameter that controls hydraulic sorting is the mineral concentration within the bedrock. Analysed catchments cover similar bedrock lithologies, thus we assume similar apatite and quartz fertilities within the catchment area. The grain shape has a minor effect

on the settling of minerals and the size shift between quartz and apatite is small, because the mineral densities differ not too greatly (Quartz: 2.65 g/cm^3 and Apatite: 3.20 g/cm^3) (e.g. Malusà et al., 2016). We therefore assume that quartz and apatite behaved similarly during transport and have the same origin.

The sampled catchments are steep, glaciated and cover a wide range of elevations (>2400 m) (Fig. 4.1 and 4.2) and thus production of cosmogenic nuclides vary strongly (Lal, 1991; Stone, 2000). An elevation-dependent erosion variation within the catchment area may therefore significantly influence ^{10}Be-derived denudation rates. If higher elevations (high cosmogenic nuclide production rates) erode faster than lower elevations (low nuclide production rates), the resulting nuclide concentration in the stream sediment would be higher as if the erosion was focused on lower elevations. This hypothesis may apply as long as the non-uniform erosion pattern prevails for a relatively long period having a significant effect on the in-situ ^{10}Be production. In contrast, the standard ^{10}Be method described above (cf. section 4.4.3.2) underlies the assumption that the calculated denudation rate represents a long-lasting uniform distribution of erosion in the whole catchment area. Short-term non-uniform erosion events have no impact on the calculation, because averaged over many years the erosion is assumed to be uniform (e.g. von Blanckenburg, 2005). We speculate that this assumption may be invalid in Alpine settings, because of a possibly long-lasting non-uniform distribution of erosion in addition to a long-lasting non-uniform production of cosmogenic nuclides (e.g. pronounced topography, glacier and snow shielding). Therefore, both scenarios were tested on this dataset to quantify, which scenario provides the best approximation of representative denudation rates. First, the standard method was applied, at which the erosion is equally distributed within the catchment. Second, the standard method was modified by considering spatial variations in the distribution of erosion probabilities, which were derived by the iterative formation of erosion probability maps (cf. section 4.4.2.2).

Before applying the new approach of a variable distribution of erosion probabilities on a real dataset, we tested the robustness of the method with different synthetic scenarios, in which we varied the probability of erosion with the elevation. This test was based on the catchment area and the ^{10}Be concentration of the sample CGP228 (cf. Tab. 4.1 and 4.5). For this purpose, the catchment area was divided in three areas of approximately the same size (each ~22 km^2) with mean elevations of 1590 m (green area), 2170 m (red area) and 2720 m (blue area) (Fig. 4.5 and Tab. 4.2). No shielding was considered, hence the nuclide production was only scaled to elevation and latitude (Lal, 1991; Stone, 2000).

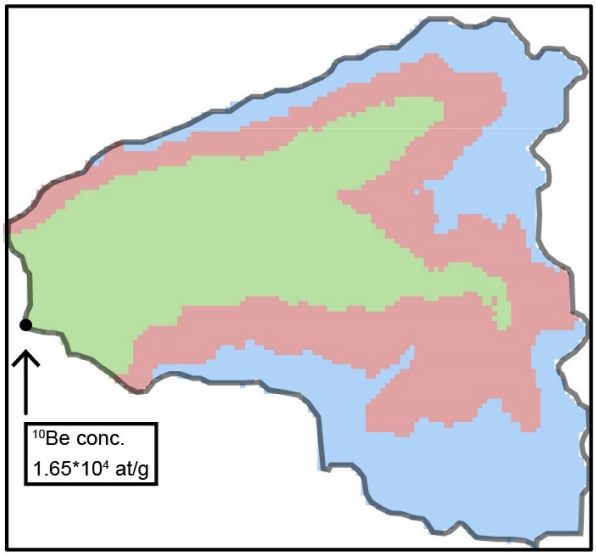

Figure 4.5: Catchment of the sample CGP228 divided into three synthetic parts: green = bottom section, red = middle section and blue = upper section.

Table 4.2: Geomorphological details and mean production rates from different mean elevations

	Area (km²)	Mean elevation (m)	Elevation range (m)	Mean production rates (at/g/yr)
	22	1590	888	15
	22	2172	460	23
	22	2720	983	34
a)	66	2153	2388	24

The different colors refer to different parts of the catchment: green = bottom section, red = middle section and blue = upper section. For comparison we also show the details from the whole catchment area a). The mean ^{10}Be production rates from relevant parts are calculated with no shielding correction.

An uniform distribution of erosion (scenario 1) yielded in a denudation rate of 0.99 mm/a (Tab. 4.3). In scenarios 2 - 4, it was assumed that the erosion occurred solely in the different sections of the catchment and the excluded areas did not contribute any quartz into the fluvial sample. As a result, derived denudation rates differed depending on which section was eroding; eroding solely the lower or higher elevations resulted in an under- or overestimation of denudation rates (scenario 2 and 4, Tab. 4.3). Focused erosion on the middle section (scenario 3), in turn, yielded in a denudation rate that is almost similar to an uniform denudation (scenario 1).

Further scenarios (scenarios 5 - 10) demonstrate varieties of the distributions of erosion

in different sections. Resulting denudation rates will differ from the uniform scenario by >10%, if either the higher or the lower section is eroding approximately twice as fast as the rest of the catchment (Tab. 4.3). These results lead to the conclusion that cosmogenically-derived denudation rates are significantly influenced by elevation.

Table 4.3: Different synthetic scenarios with varying distribution of the erosion probability

Scenarios	Distribution of erosion probability			Denudation rate (mm/ka)
1	0.33	0.33	0.33	**0.99**
2	1	0	0	**0.67**
3	0	1	0	**0.97**
4	0	0	1	**1.35**
5	0.5	0	0.5	**1.01**
6	0.4	0.2	0.4	**1.00**
7	0.5	0.25	0.25	**0.91**
8	0.25	0.5	0.25	**0.99**
9	0.17	0.33	0.5	**1.11**
10	0.5	0.33	0.17	**0.88**

Results shown here are based on measured ^{10}Be nuclide concentration and catchment area of the sample CGP228 (Fig. 4.1, Tab. 4.4). The distribution of erosion probabilities correspond to the different sections: green = bottom, red = middle and blue = top.

Using individual erosion probability maps obtained from the inversion of AFT age distributions (see section 4.4.2.2), we applied this approach to each measured ^{10}Be concentration. Mean catchment production rates were simply derived by adding the pixel-dependent normalized erosion probability as a multiplier in equation 4.4. Based on the erosion probability-weighted production rates, mean catchment-wide denudation rates were calculated (Tab. 4.5) An erosion map for each catchment was deciphered by transferring the erosion probability of each catchments' cell into an individual denudation rate, by multiplying the mean catchment-wide denudation rate with the normalized erosion probability of each cell. On the one hand, cells with an erosion probability of almost 100% (Fig. 4.7) yields denudation rates higher than the mean catchment-wide denudation rate. On the other hand, low erosion probabilities lead to lower rates than mean catchment-wide denudation rates. Therefore, if the erosion probability is not considered, the cells' mean denudation rate of the erosion maps will result in much lower rates compare to calculated mean catchment-wide denudation rates of Tab. 4.5.

Furthermore, the erosion maps include glaciated areas, because they also contribute grains to

the observed AFT age distribution (Fig. 4.9). Accordingly, there is erosion below glaciers, but no ^{10}Be nuclides production.

4.5 Results

4.5.1 Detrital thermochronology

4.5.1.1 Single-grain ages from stream sediments

Modern stream sediment samples from the study area cover single-grain ages of 1 – 75 Ma (Fig. 4.6 and Tab. 4.4), whereas interpolated surface AFT ages of the same area only vary between 4 and 15 Ma (cf. Fig. 4.6 and Fig. 4.10 in the Appendix). Nevertheless, the central ages from the detrital record range between 7.9 and 11 Ma and thus cover main parts of the interpolated ages. Given that only up to four single-grain ages per sample are older than 30 Ma, and therefore representing the period prior the Alpine evolution (e.g. Schmid et al., 1996), we assume that the big discrepancy is caused due to the high analytical uncertainty of single-grain AFT ages (e.g. Vermeesch, 2007) rather than representing apparent AFT ages from the Eocene and Paleocene. In every sample, there is an increased incidence of measured ages around 8 Ma (Fig. 4.6), which is in accordance to the mean interpolated bedrock AFT age of 7.8 Ma.

Table 4.4: Detrital apatite fission track data

Sample	# grains	ρs	Ns	ρi	Ni	ρd	Nd	P(χ^2) [%]	U [ppm]	Age range (Ma)	Central age ± 1σ (Ma)
CGP220	61	2.94	214	33.49	2439	7.6117	3257	0	60.5	**1.2 - 68.2**	**8.3 ± 0.8**
CGP221	58	3.18	189	33.56	1997	7.6031	3257	16	60.8	**2.7 - 60.7**	**8.4 ± 0.8**
CGP224	100	3.59	440	30.05	3682	7.5771	3257	0	52.8	**3.1 - 74.8**	**11.0 ± 0.9**
CGP225	52	2.67	158	23.75	1406	7.5684	3257	86	42.2	**3.2 - 58.2**	**9.8 ± 1.0**
CGP228	100	2.31	278	24.71	2975	7.5338	3257	20	43.4	**2.2 - 52.1**	**8.2 ± 0.6**
CGP229	100	3.74	392	41.65	4369	7.5252	3257	3	72.8	**2.0 - 38.2**	**7.9 ± 0.6**
CGP242	87	2.25	236	23.04	2417	7.4214	3257	28	42.1	**3.1 - 51.4**	**8.5 ± 0.7**

$\rho s(\rho i)$ is the spontaneous (induced) track density (10^5 tracks/cm^2); Ns (Ni) is the number of counted spontaneous (induced) tracks; ρd is the dosimeter track density (10^5 tracks/cm^2); Nd is the number of tracks counted on the dosimeter; P(X^2) is the probability of obtaining Chi-square value (X^2) for n degree of freedom (where n is the number of crystals minus 1); Central ages and corresponding 1σ errors are calculated following Galbraith and Laslett (1993).

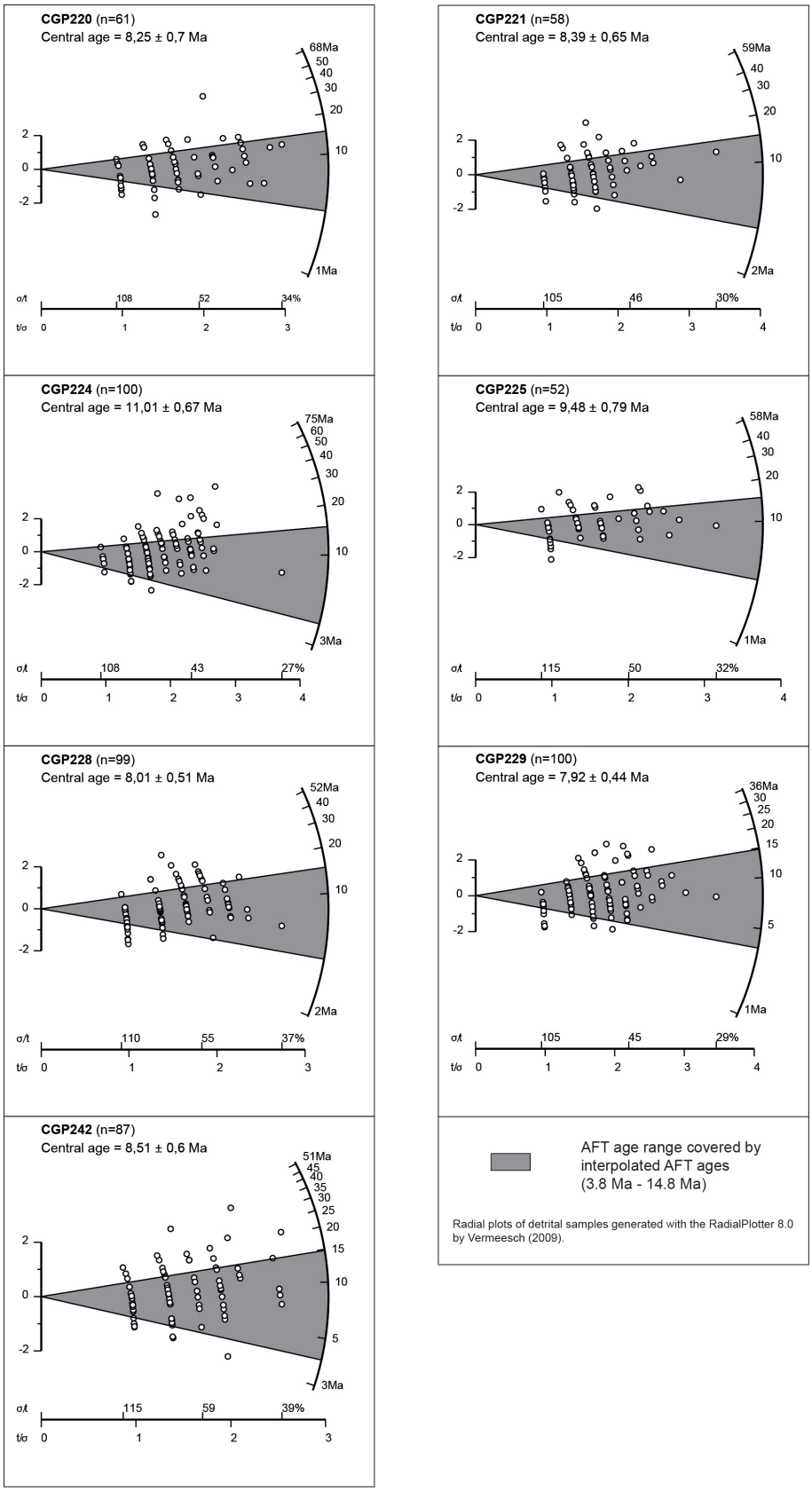

Figure 4.6: Radial plots of each detrital sample using the logarithmic transformation from Galbraith (1990) and generated with the RadialPlotter 8.0 by Vermeesch (2009). Gray area covers the age range from the interpolated AFT ages.

4.5.1.2 Erosion pattern at different elevations

Predicted erosion probabilities of samples share similar patterns although different catchments of the Lütschine river and Aare river were sampled (Fig. 4.7). Samples from larger catchments are better fitted with two erosion peaks (Fig. 4.7A). Therefore, most of the apatites originate either from an elevation between ~900 - ~1600 m or from ~2800 - ~3400 m. The probability of erosion is almost zero between both peaks, suggesting an "erosion gap" at elevations around ~1600 – 2800 m (Fig. 4.7A).

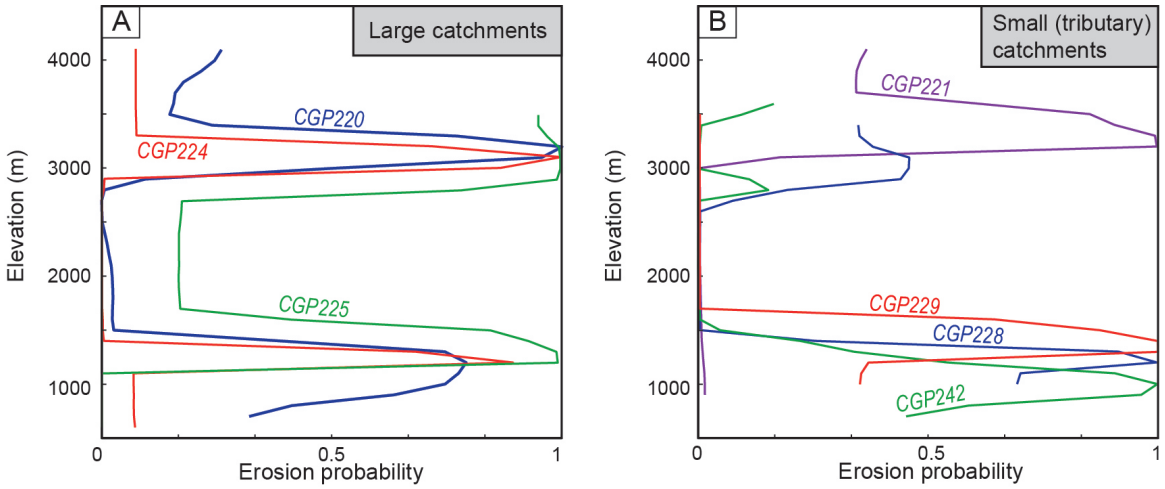

Figure 4.7: Diagrams show the erosion probability at each elevation for large **(A)** and small **(B)** catchments, based on the iterative approach at which the provenance of apatites is transformed into an erosion probability. The small catchments are sub-catchments within the comprising large catchments (Fig. 4.1).

Predicted erosion probabilities show more variations in small catchments (Fig. 4.7B). Half of the catchments also yield two erosion peaks (CGP242, CGP228) similar to Figure 4.7A. A slight difference, however, is that in both cases the erosion probability at high elevations is 20 to 50% lower compared to the low elevations (Fig. 4.7B). Instead, the inversion of the AFT data suggests for catchments CGP229 and CGP221 that erosion exclusively takes place at low elevations (between ~1300 and 1700 m) or high elevations (between ~3100 and ~3600 m). In summary, every catchment remains nearly unaffected by erosion around 2000 m. Further decreasing erosion probabilities are also found at the lowest (<1000 m) and highest (>~3300 m) parts of the catchments.

4.5.2 ^{10}Be-derived denudation rates

Measured ^{10}Be concentrations, corrected for laboratory blank (blank ratio $1.52 \cdot 10^{-15}$ ^{10}Be/^{9}Be), range from $1.34 \cdot 10^{4}$ to $1.96 \cdot 10^{4}$ at/g (Tab. 4.5). Calculated with the standard method (uniform erosion), these cosmogenic nuclide concentrations yield mean production rates from 13.58 to 16.66 at/g·a. Corresponding denudation rates are between 0.54 $\pm$ 0.1 mm/a and 0.92 $\pm$ 0.3 mm/a with the highest and lowest rates in catchments CGP229 and CGP221. Thus, the denudation rates cover a time period between the last ~1000 years, estimated for a mean cosmic ray attenuation length of ~160 g/cm^2 and a density of 2.7 g/cm^3 (e.g. Balco et al., 2008). According to the newly introduced and unscaled ^{10}Be production rate of Borchers et al. (2016), resulting mean catchment-wide production and denudation rates are about ~9% lower than rates based on the previously used production rate of Balco et al. (2008).
In contrast, production rates that were corrected for the erosion probability distributions are in most cases lower (between 4 – 38%) than rates calculated with the standard method (Tab. 4.5). The only exception is catchment CGP224, where the difference is negligible and CGP221, where production rates are about 23% higher than estimated with the standard method. Resulting denudation rates decreases in six out of seven cases compared to an uniform erosion pattern. The dispersion in denudation rates also decreases; catchments CGP225, 228, 229 and 242 result in similar denudation rates of 0.48 – 0.52 mm/a (Tab. 4.4).
In the particular case of sample CGP224, we compare the apatite composition of fluvial sediment from 2010 with the ^{10}Be concentration of a stream sediment sample from 2013. We suggest that this circumstance has an insignificant effect on the analysed sample composition, because it is assumed that the residence time of sediments is longer than three years in catchments of this size with three different oriented tributary valleys (catchment area: 364 km^2). This hypothesis is supported by a study from Kober et al. (2012) in the same study area. Between 2010 and 2013, the Aare catchment experienced several debris-flow events, which indeed significantly perturbed ^{10}Be concentrations of stream sediment samples from the Aare river (Kober et al., 2012). However, in contrast to the location of samples CW6 and CGP224, the fluvial sediment in the study of Kober et al. (2012) derives from a position further upstream, closer to the sediment outlets from the debris-flows, and its catchment has no connection to tributary valleys. The study by Kober et al. (2012) covers the time period prior and after debris-flow events. The measured denudation rate prior the debris-flows represents an undisturbed rate of homogeneously-mixed sediments and yields a denudation of ~0.9 mm/a, which is higher than the rate of the sample CW6 with 0.78 mm/a. Accordingly, several debris-flow events did not impact the sediment composition of the sample CW6 and, therefore, it may be probable that our hypothesis is true and three years may have no significant effect on this sample.

Table 4.5: Cosmogenic nuclide data

	Weight quartz (g)	^{10}Be conc. (10^4 at/g) a)	Mean shielding b)	Standard method			Corrected rates e)			Long-term exhumation rate (mm/a) f)
				Mean production rates (at/g*a) c)	Denudation rate (mm/a)	Internal error (mm/a) d)	Mean production rates (at/g*a)	Denudation rate (mm/a)	Internal error (mm/a)	
CGP 220	20.4	1.96	0.53	16.64	0.62	0.2	10.17	0.61	0.2	0.50
CGP 221	26.6	1.34	0.45	16.66	0.92	0.3	21.59	1.15	0.4	0.47
CW6	34.6	1.49	0.67	15.98	0.79	0.1	15.38	0.78	0.1	0.54
CGP 225	33.7	1.80	0.67	14.18	0.59	0.1	10.75	0.52	0.1	0.53
CGP 228	38.5	1.65	0.71	15.26	0.68	0.1	10.75	0.52	0.1	0.55
CGP 229	37.6	1.92	0.53	13.58	0.54	0.1	11.93	0.48	0.1	0.53
CGP 242	26.0	1.64	0.61	15.66	0.71	0.2	10.17	0.50	0.1	0.52

a) ^{10}Be concentration is corrected for the laboratory blank (blank ratio $1.52 \cdot 10^{-15}$ ^{10}Be/^{9}Be).
b) Mean shielding includes the topographic shielding (Dunne et al., 1999), glacier shielding (Schildgen et al., 2005), snow shielding (Wittmann et al., 2007) and a lithology factor.
c) Pixel-averaged production rates, according to the standard calculation method.
d) The internal error will be adequate, if the samples derive from the same study area. For a supraregional comparison an external error will be necessary (Balco et al., 2008).
e) Standard method adjusted to normalized erosion probability.
f) Mean long-term exhumation rates calculated in AGE2EDOT (Ehlers et al., 2005), based on mean AFT ages of every catchment.

Finally, it should be emphasized that the denudation rates do not correlate with any geomorphic parameter (such as mean hillslope, relief, mean elevation and size of glaciated areas); neither if we compare the rates based on the standard method nor the corrected rates with the geomorphic parameter.

4.6 Discussion

The method to derive accurate estimates of catchment-wide denudation rates with in-situ produced ^{10}Be may reach its limits in a complex geomorphic setting like the Central Alps (e.g. Kober et al., 2012; Delunel et al., 2014; Savi et al., 2014). Hence, our presented approach is supposed to extend these limits, while taking into account any deviations from the assumed uniform erosion pattern. A successful implementation of the presented approach depends on two main factors. First, the accuracy of the provenance analyses and second, if the resulting erosion pattern is explicable with naturally-occurring landscape-forming processes.

The provenance analyses are based on AFT dating. The radial plots in Figure 4.6 demonstrate that ~30% of measured ages are not covered by the interpolated age range on which the provenance analyses are based on, whereas we observe an increased occurrence of old ages ($>$14.8 Ma) compared to young ages ($<$3.8 Ma). Besides analytical discrepancies within the AFT dating (e.g. Vermeesch, 2007), elevation ranges that are underrepresented in measured AFT ages may be a potential difficulty (Fig. 4.8); especially with increasing elevation the sample quantity decreases. Hence, peak regions may yield older AFT ages than resolved by the interpolated age map. Nevertheless, the elevation range of $>$3000 m reflects only a small proportion from the total catchment area (Fig. 4.8). The interpolation is based on measured AFT ages from surroundings of the Aar massif anyway; therefore a lack of data at a specific elevation range in this area may not have a negative effect on the accuracy of interpolation and may not be decisive for the determination of the distribution of erosion. Irrespective whether or not every measured age could be traced back precisely, interestingly, the elevation-dependent erosion probabilities show a comparable distribution beyond different valleys (Fig. 4.7). The similarity of the results over the entire study area is our main argument for an acceptable reproducibility of our provenance data.

Therefore, in the following, the provenance of apatites is tested for potential decisive naturally-occurring landscape-forming processes as well as its impact on developed erosion maps and corresponding corrected mean catchment-wide denudation rates. The bedrock strength is suggested to be mainly responsible for the topographic expression (e.g. Korup and Schlunegger, 2007; Robl et al., 2015), but because of similar crystalline rocks in this area, the effect is assumed to be negligible for the used methods.

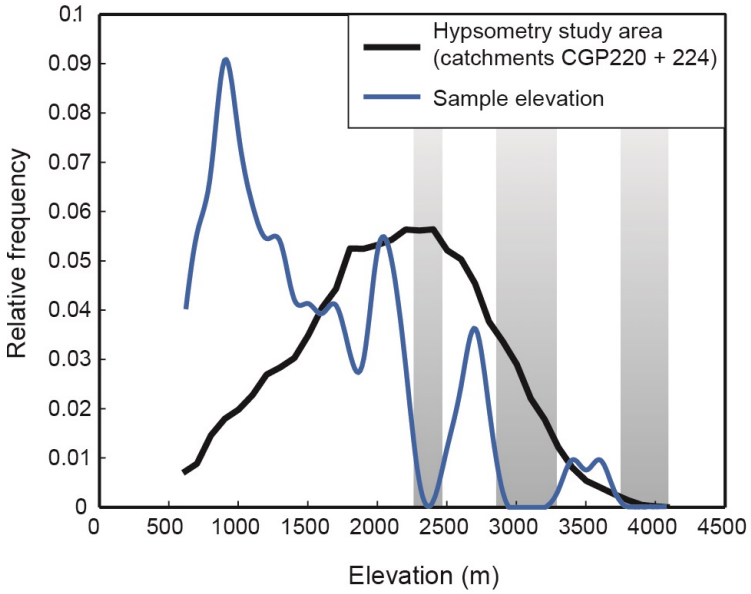

Figure 4.8: Relative frequency of elevations of catchment areas from samples CGP220 and 224 (black line) and the relative frequency of elevation ranges that were sampled for AFT (blue line). Gray boxes mark gaps in sampled elevation ranges (2250-2450 m, 2850-3200 m, 4000-4500 m) and reflecting a lack of measured AFT ages from higher elevations.

4.6.1 Controls on the erosion pattern

Supraregional, the development of orogens is affected by an interplay between tectonic deformation, surface uplift, climate and exhumation and each tries to achieve the steady-state (e.g. Willett, 1999; Willett and Brandon, 2002). Regionally in the Central Alps, the erosion pattern is controlled by geomorphic mechanisms that still compensate relics of the erosive effects of Pleistocene glaciations (e.g. Norton et al., 2010; Schlunegger and Norton, 2013). Therefore, it is likely that a non-uniform distribution of erosion is driven by processes that balance a local non-steady-state.

Our results emphasize two peak elevations that are considered as main sources of apatites and accordingly with relatively high erosion (Fig. 4.7). Corresponding erosion maps reveal highest denudation rates at elevation ranges that are characterized by maximum erosion probabilities (Fig. 4.9). Catchments CGP220, 224 and 225 show a nearly symmetrical erosion pattern (Fig. 4.7) resulting in almost the same denudation rates of 0.7 mm/a at high and low elevations in catchment CGP225 (Fig. 4.9). In contrast, the erosion maps of catchments CGP220 and 224 reveal lower denudation rates at low elevations than at high elevations; 0.4 - 0.7 mm/a and 0.9 - 1.2 mm/a, respectively. Erosion in the small catchments is focused either on low elevations in catchments CGP228 (~0.75 mm/a), 229 (~0.6 mm/a) and 242 (~0.75 mm/a) or on high elevations in catchment CGP221 (~1.3 mm/a) (Fig. 4.9).

The erosion peak at high elevations (2800 – 3500 m) is located around the position of the

equilibrium line of altitude (ELA) of present-day glaciers, which is at ~2900 m (Zemp et al., 2007). Temperature conditions are here in the permafrost area. In the study area the mean 0°C isotherm is at ~2345 m, based on data about mean annual air temperatures (MAAT) from weather stations in Lauterbrunnen (797 m) of 8.7°C and Jungfraujoch (3580 m) of -6.5°C, which are located in the study area, and an atmospheric lapse rate of 0.56 °C/100 m (Rolland, 2003). Therefore, these high elevations are characterized by glaciers, snow fields and nunataks from the LGM. Chemical weathering and soil production is nearly non-existent on the few bare rocks in this area (e.g. Schlunegger and Norton, 2013). Furthermore, continuous air temperatures below the freezing point lead to permafrost and prevent the exposed rocks (nunataks) from increased erosion through frost-cracking, because no or only less liquid water is available (e.g. Hales and Roering, 2007). We hypothesize that at these elevations the accelerated glacial erosion below the glaciers at the present-day ELA is mainly responsible for the erosion peak. This result is in accordance with the distribution of glacial erosion below a glacier in the Coast Mountains in Canada (Ehlers et al., 2015) and global glacial erosion models of Alpine glaciers (Herman and Braun, 2011).

However, the erosion peak at low elevations (900 - 1700 m) encloses the position of the ELA during LGM (1300 – 1600 m) (Ivy-Ochs et al., 2008). This elevation range yields maximal hillslope angles (>30°), which otherwise only exist around the arêtes (Robl et al., 2015). The oversteepened slopes are relics of increased glacial erosion during major Pleistocene glaciations around the ELA of most extensive glacial advances (e.g. Egholm et al., 2009; Herman and Braun, 2011; Schlunegger and Norton, 2013; Robl et al., 2015). The idea of a strong glacial impact around the lowest extent of Quaternary ELAs is corroborated with the increased occurrence of young interpolated surface AFT ages ($\leq$ 5 Ma)(Fig. 4.10 in the Appendix), which is assumed to be due to focused glacial erosion that led to accelerated exhumation of bedrock (chapter 3). Hence, we suggest that this Holocene erosion peak at this elevation range is caused by effective fluvial incision of oversteepened slopes or hanging valleys. Consequently, the intensified fluvial erosion at this elevation range is still responding to the impact of the Pleistocene glaciations.

Based on our data we conclude that two distinct erosion processes control the erosion in Alpine valleys; fluvial incision of oversteepened slopes at lower elevations and effective glacial erosion at the present-day ELA at higher elevations. Due to similar erosion probabilities at both elevations (Fig. 4.7), it can be deduced that both processes are approximately equally important. This result is in accordance with studies from Schlunegger and Norton (2013) and Salcher et al. (2014), who suggested that both mechanisms control catchment-wide denudation rates. The advantage of the presented approach is that we are able to constrain the local extent of each erosion regime.

Previous studies found that frost-cracking processes play a primary role in the production of

sediments in mountainous areas (e.g. Delunel et al., 2010; Anderson et al., 2013; Savi et al., 2015). Highest frost-cracking intensities are associated with positive MAATs close to 0°C, where liquid water is available and rock temperatures are between -3 and -8°C (e.g. Anderson et al., 2013; Savi et al., 2015). Below 0°C, permafrost would prevent the rocks to erode. According to these results, the sediment production by frost-cracking should have highest intensities at or below an elevation of ~2345 m, which is exactly the elevation range, where every catchment seems to be nearly unaffected by erosion (Fig. 4.7). Therefore, either frost-cracking is not a primary sediment producer in our study area or the precision/resolution of our data is not high enough to resolve the effect of frost-cracking.

4.6.1.1 Local erosion processes at catchment scale

According to our thermochronological data, sediments from larger catchments (CGP220, 224 and 225) derive from low elevations by fluvial erosion and from high elevations by glacial erosion. On the contrary, samples CGP228, 229 and 242 originate almost exclusively from effective incision of oversteepenend slopes triggered by fluvial erosion. At first glance, the observed mismatch is surprisingly, because the latter are sub-catchments of analysed larger catchments. Consequently, the sediment compositions differ from the composition of samples that were taken more downstream; and more specific, sediments from high elevations represent a large proportion in a stream sediment composition further downstream.
We hypothesize that local geomorphic conditions may have an influence on sediment delivery and emphasize the role of pro-glacial lakes for studying sediment provenance and pathways. These lakes have a big influence on sedimentation processes and may trap a large proportion of sediments (e.g. Anselmetti et al., 2007), especially the glacial sediments originating from high elevations. Larger catchments have a few active connections between glaciers and streams, whereby glacial sediments are directly delivered into the fluvial network. Instead, in the catchment of sample CGP229 the source area of glacial sediments and the basin outlet is completely disconnected by a pro-glacial lake, explaining why stream sediments exclusively derive from low elevations (Fig. 4.7 and 4.9). In catchments CGP228 and 242 active tributary connections from small glaciated areas towards the sample points exist (Fig. 4.9), resulting in low erosion probabilities at high elevations (Fig. 4.7). Therefore, the coincidence of pro-glacial lakes and focused erosion on low elevations supports the accuracy of the presented approach.
On the contrary, these lakes are not older than the maximal extent of LIA glaciers (max. 200 years ago), because the position of the recent glacial lakes was covered through the LIA glaciers (e.g. Hantke and Wagner, 2005; Schimmelpfennig et al., 2014). Hence, the lakes as sediment traps have not been active for a long time (at maximal glacial extent between

the 14th and 19th century AD) and glacial sediments could have passed unimpeded into the fluvial system. This may explain the strong erosion signal at high elevations in the largest catchments CGP220, 224 and 225, where sediments have longer residence times in the hydrological network compare to the smaller ones. Especially the intensity of erosion at high elevations in the catchment CGP225 and corresponding sub-catchments CGP228 and 229 may differ, because catchments CGP228 and 229 may represent the situation younger than the LIA (<200 years), whereas CGP225 may integrate over a longer period of time indicated by an increased input of glacial sediments. Consequently, in addition to the existence of pro-glacial lakes, the residence time of sediments also influences the sediment composition in analysed fluvial sediment.

Conversely, sediments in the sub-catchment CGP221 derive exclusively from the highest areas, where glacial erosion dominates. This catchment is characterized by two glaciers (Grindelwald Glaciers) and both are not connected to any pro-glacial lake, as in catchments CGP228, 229 and 242. However, on top of one of the Grindelwald glaciers a lake has been regularly formed since 2005, which has no over-ground drainage. Consequently, the water is flowing through the ice producing repetitive glacial lake outbursts (e.g. Werder et al., 2010), which may explain the distribution of erosion in this catchment. Due to the outbursts, large volumes of glacial sediments are delivered abruptly and rapidly into the fluvial system and may amount to the largest proportion in the stream sediment as well as resulting into highest denudation rates.

Our results appear to contradict the former assumption that short-term changes in the distribution of erosion do not have any impact on catchment-wide denudation rates, as these usually cover a longer time span (e.g. von Blanckenburg, 2005; Foster and Anderson, 2016). This is true in low-relief areas, but due to a pronounced topography with a strong elevation-dependent cosmogenic nuclide production, short- and long-term variations in erosion rates bias cosmogenically-derived denudation rates. Hence, the mean cosmic ray attenuation length below the surface may not simply equated with the time span that it takes to erode the bedrocks, like it was previously assumed (e.g. von Blanckenburg, 2005).

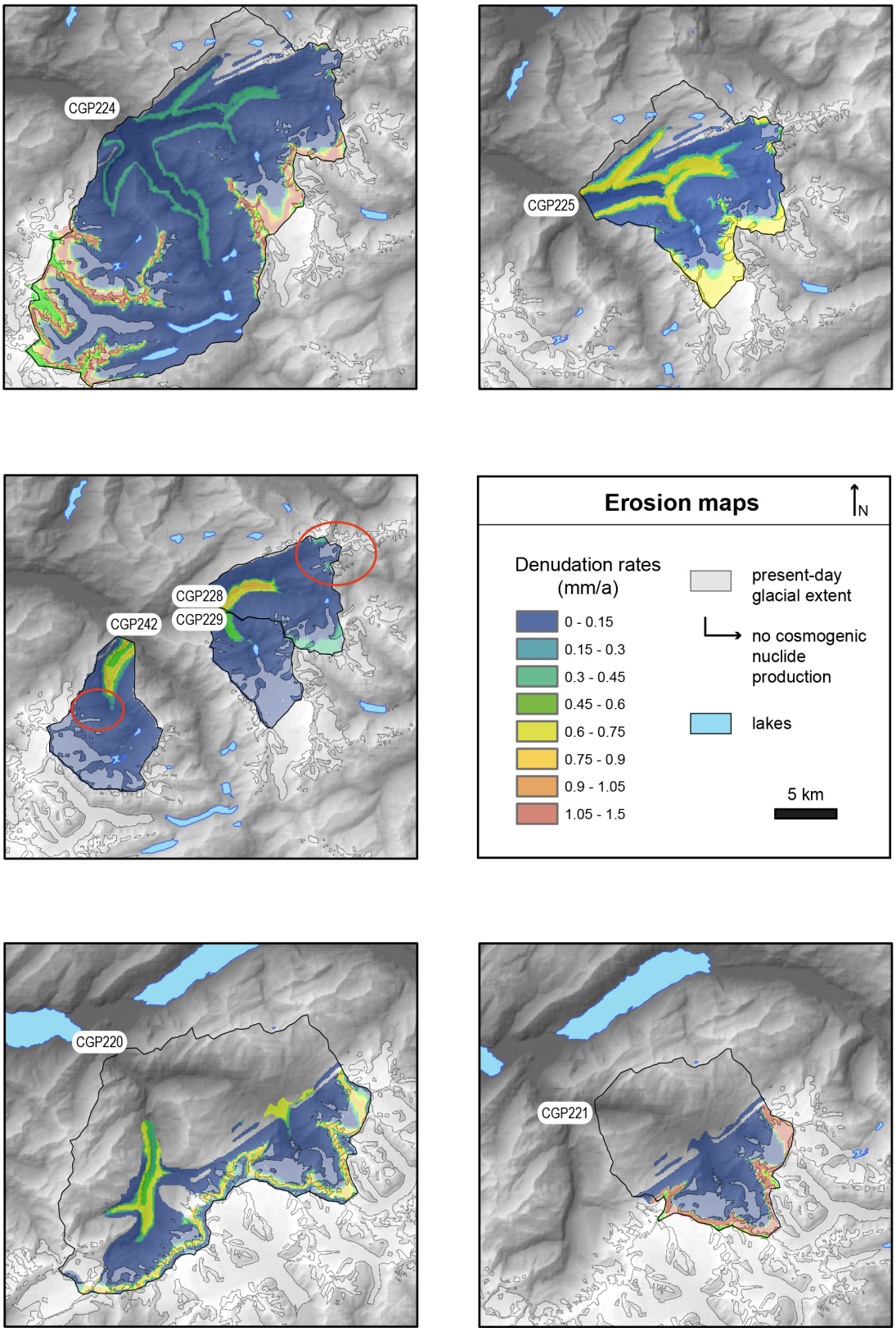

Figure 4.9: Erosion maps of each studied catchment with denudation rates between 0 and 1.5 mm/a. Red circles mark the areas in catchments CGP228 and 242, where glacial sediments are produced and are transported towards the basin outlet without being trapped in a glacial lake.

4.6.2 Erosion pattern-weighted denudation rates

The influence of the erosion pattern on catchment-wide denudation rates depends on which erosion process dominates in the catchment. Prevailing fluvial erosion (at low elevations) leads to lower denudation rates (CGP228, 229 and 242), compared to those assuming uniform erosion (Tab. 4.5). These catchments erode at ~0.5 mm/a, which is similar to pure fluvial catchments elsewhere in the European Alps (Norton et al., 2011). However, strengthened input of glacial sediments into the hydrological system results in catchment-wide denudation rates of 1.15 mm/a (CGP221) and, locally, to rates up to ~1.4 mm/a (Fig. 4.9). This sample yields the lowest ^{10}Be concentration; therefore, even without correction the denudation rates would be highest in this catchment (Tab. 4.5).
The distribution of erosion in the large catchments CGP220 and 224 is almost symmetrically distributed with a little focus on higher elevations, and therefore the correction has only a negligible influence on denudation rates ($<$2%). Instead, the symmetrical distribution in catchment CGP225 results in lower denudation rates ($<$12%), because of a larger proportion of erosion within the zone of fluvial erosion at lower elevations. Consequently, if the catchments are large enough ($>$300 km^2), it will be possible to estimate representative denudation rates in an Alpine setting, because the correction with erosion probabilities does not affect the denudation rates, confirming Niemi et al. (2005); Binnie et al. (2006); Wittmann et al. (2007) and Savi et al. (2015).
Finally, we can summarize that the corrected denudation rates are in the same order as rates from adjacent Alpine valleys (e.g. Wittmann et al., 2007; Delunel et al., 2010; Norton et al., 2010, 2011; Glotzbach et al., 2013; Delunel et al., 2014); low rates of ~0.5 mm/a in response to fluvial erosion and high rates of $>$0.7 mm/a characterized by rapid erosion as a consequence of glaciations. According to the work from Wittmann et al. (2007), ^{10}Be-derived catchment-wide denudation rates balance present-day rock uplift. Recent geodetic uplift in the study area ranges between ~0.5 mm/a and ~0.9 mm/a (e.g. Schlatter et al., 2005), which fits to our denudation rates. Furthermore, most of the cosmogenic nuclide derived denudation rates almost achieve similar values compared to long-term exhumation rates (~0.53 mm/a) that are based on thermochronological ages (Tab. 4.5). Instead, denudation rates of catchments with a proven larger glacial inheritance exceed long-term exhumation rates (CGP220, 221 and 224) in which the latter is predominantly controlled by tectonics rather than by climate change. This result is in accordance with a study about the Western Alps from Glotzbach et al. (2013). However, denudation rates of fluvial landscapes are linked to geomorphic parameters such as hillslope angles, which are influenced by tectonics (e.g. Ouimet et al., 2009; DiBiase et al., 2010), in contrast glacial erosion perturbs this connection (e.g. Norton et al., 2010; Glotzbach et al., 2013).

4.6.3 Future potential

The presented approach is based on the local provenance of apatite grains in stream sediments. Hence, it can only be used if adequate bedrock AFT ages are available, which allow a detailed overview over the spatial distribution of ages. This, of course, is the main limiting factor of the application from the presented approach. Note that the provenance analyses here are based on the assumption that the AFT ages mainly vary with elevation with only minor lateral variations within the catchment. Therefore, this approach may need further adjustment in study areas that are characterized by active tectonics causing spatially variable local rock uplift. A precise resolution of locally varying exhumation rates is inevitable. However, testing the proposed provenance of sediments with an independent provenance method, for example with zircon fission track or (U-Th-Sm)/He at apatites or zircons may be helpful. New data about sediment sources may support the robustness of the approach, as well as confirming a negligible influence of locally varying active tectonics.
Nevertheless, in high mountain areas where denudation rates vary independently of geomorphic parameter and a non-uniform distribution of erosion is expected, it is an efficient alternative to quantify distinct erosion processes. Here the denudation rates can be transferred into representative rates for each catchment, representing either fluvial erosion or glacial erosion or both. The distinct areas at which the erosion is focused on lead us to the conclusion that the corrected rates provide a realistic reflection of erosion processes in mountainous areas. We suggest that the adjusted denudation rates are a better approximation on erosion processes in an Alpine setting compare to denudation rates calculated with the standard method, especially if the deviations are greater than the error ($>10\%$). Constraining erosion processes at catchment scale might also be interesting for a broad readership, as for example glacial erosion influence the height of mountain ranges and is therefore an important factor during landscape evolution (e.g. Egholm et al., 2009).

4.7 Conclusions

The quantification of source elevations from apatite grains based on detrital thermochronology provides new insights into the dominating erosion processes in an Alpine catchment. Results suggest that main sources of sediments are two sharp elevation ranges, at ~900 m to ~1600 m and at ~2800 m to ~3400 m. At high elevations glacial erosion below the present-day ELA is designated as a main sediment producer. Accelerated fluvial erosion at oversteepened hillslopes around the position of former ELAs from Pleistocene glaciations is identified as a main sediment producer at lower elevations. These results are used to improve the calculation of catchment-wide denudation rates based on ^{10}Be concentrations from the same samples.

Our data demonstrate that the denudation rates depend on the prevailing erosion processes, fluvial or glacial erosion. Prevailing fluvial erosion yield mean catchment-wide denudation rates of ~0.5 mm/a. In contrast, effective glacial erosion provides denudation rates up to 1.4 mm/a.

The presented approach at which detrital thermochronology is combined with cosmogenic nuclide measurements helps to understand the spatial variations of characteristic erosion processes in a mountain setting. It improves the calculation of catchment-wide denudation rates in Alpine catchments, where the common assumption that ^{10}Be concentrations in stream sediments represents spatially and temporally averaged values may be invalid.

4.8 Appendix

The interpolated surface apatite fission track (AFT) ages were used to define the origin of stream sediments by comparing the AFT age composition of stream sediments with the surface age map. For methodological details of the interpolation, please refer to chapter 3.

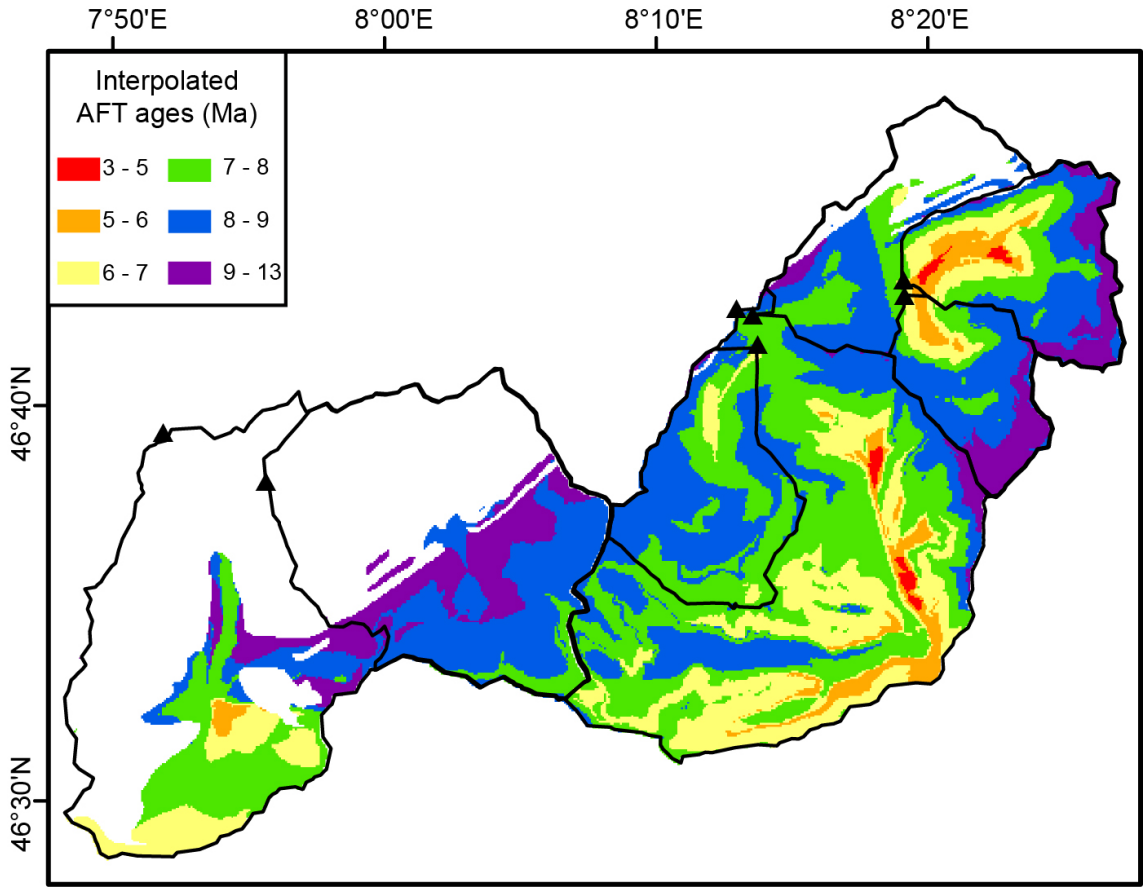

Figure 4.10: Interpolated surface AFT ages, which are based on published bedrock AFT ages from the Alps (grid resolution 90 m).

The error map, corresponding to the AFT age map (Fig. 4.10), is calculated by bootstrapping of the input dataset (cf. section 4.4.2.2). The largest errors occur, where the age discrepancies between observed and modelled ages are highest.

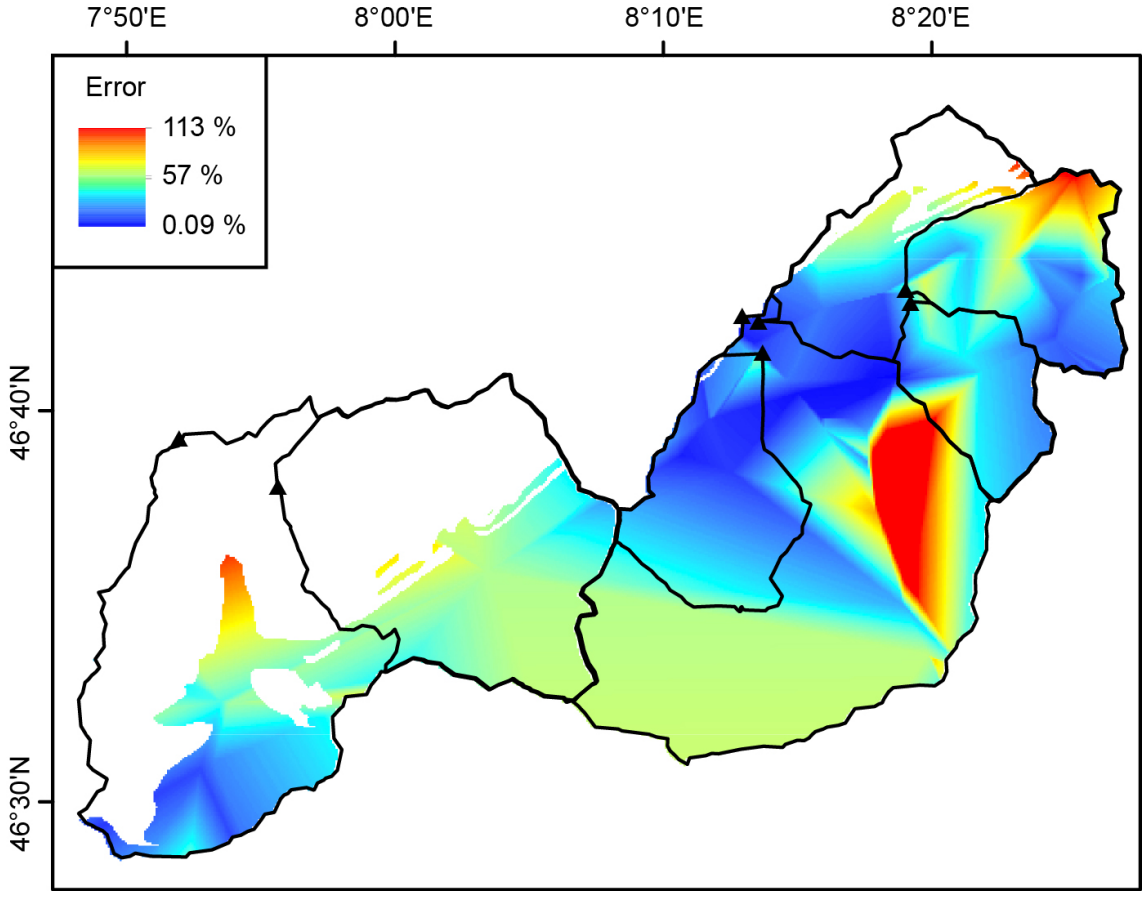

Figure 4.11: Error map of interpolated surface AFT age map (grid resolution 90 m).

References

Albrecht, J. (1994), 'Geologic units of the Aar massif and their pre-Alpine roch associations: a critical review', *Schweiz. Mineral. Petrogr. Mitt.* **74**, 5–27.

Anderson, R. S., Anderson, S. P. and Tucker, G. E. (2013), 'Rock damage and regolith transport by frost: An example of climate modulation of the geomorphology of the critical zone', *Earth Surface Processes and Landforms* **38**(3), 299–316.

Anselmetti, F. S., Bühler, R., Finger, D., Girardclos, S., Lancini, A., Rellstab, C. and Sturm, M. (2007), 'Effects of Alpine hydropower dams on particle transport and lacustrine sedimentation', *Aquatic Sciences* **69**(2), 179–198.

Auer, M. (2003), 'Regionalisierung von Schneeparametern - Eine Methode zur Darstellung von Schneeparametern im Relief, M.S. thesis'.

Avdeev, B., Niemi, N. A. and Clark, M. K. (2011), 'Doing more with less: Bayesian estimation of erosion models with detrital thermochronometric data', *Earth and Planetary Science Letters* **305**(3-4), 385–395.

Balco, G., Stone, J. O., Lifton, N. A. and Dunai, T. J. (2008), 'A complete and easily accessible means of calculating surface exposure ages or erosion rates from 10Be and 26Al measurements', *Quat. Geochronol.* **3**, 174–195.

Bierman, P. and Steig, E. J. (1996), 'Estimating rates of denudation using cosmogenic isotope abundances in sediment', *Earth Surface Processes and Landforms* **21**, 125–139.

Binnie, S., Phillips, W., Summerfield, M. and Keithfifield, L. (2006), 'Sediment mixing and basin-wide cosmogenic nuclide analysis in rapidly eroding mountainous environments', *Quaternary Geochronology* **1**(1), 4–14.

Borchers, B., Marrero, S., Balco, G., Caffee, M., Goehring, B., Lifton, N., Nishiizumi, K., Phillips, F., Schaefer, J. and Stone, J. (2016), 'Geological calibration of spallation production rates in the CRONUS-Earth project', *Quaternary Geochronology* **31**, 188–198.

Brewer, I. D., Burbank, D. W. and Hodges, K. V. (2003), 'Modelling detrital cooling-age populations: Insights from two Himalayan catchments', *Basin Research* **15**(3), 305–320.

Brown, E. T., Stallard, R. F., Larsen, M. C., Raisbeck, G. M. and Yiou, F. (1995), 'Denudation rates determined from the accumulation of in situ-produced 10Be in the Luquillo Experimental Forest, Puerto Rico', *Earth and Planetary Science Letters* **129**, 193–202.

Calais, E., Nocquet, J.-M., Jouanne, F. and Tardy, M. (2002), 'Current strain regime in the Western Alps from continuous Global Positioning System measurements, 1996-2001', *Geology* **30**, 651–654.

Champagnac, J.-D., Schlunegger, F., Norton, K., von Blanckenburg, F., Abbühl, L. M. and Schwab, M. (2009), 'Erosion-driven uplift of the modern Central Alps', *Tectonophysics* **474**(1-2), 236–249.

Chmeleff, J., von Blanckenburg, F., Kossert, K. and Jakob, D. (2010), 'Determination of the 10Be half-life by multicollector ICP-MS and liquid scintillation counting', *Nuclear Instruments and Methods in Physics Research Section B: Beam Interactions with Materials and Atoms* **268**(2), 192–199.

Coutterand, S. (2010), *Etude Géomorphologique des flux glaciaires dans les Alpes nord-occidentales au Pléistocène récent*, l'Université de Savoie, Le Bourget du Lac.

Delunel, R., van der Beek, P. A., Bourlès, D. L., Carcaillet, J. and Schlunegger, F. (2014), 'Transient sediment supply in a high-altitude Alpine environment evidenced through a 10 Be budget of the Etages catchment (French Western Alps)', *Earth Surface Processes and Landforms* **39**(7), 890–899.

Delunel, R., van der Beek, P. A., Carcaillet, J., Bourlès, D. L. and Valla, P. G. (2010), 'Frost-cracking control on catchment denudation rates: Insights from in situ produced 10Be concentrations in stream sediments (Ecrins–Pelvoux massif, French Western Alps)', *Earth and Planetary Science Letters* **293**(1-2), 72–83.

DiBiase, R. A., Whipple, K. X., Heimsath, A. M. and Ouimet, W. B. (2010), 'Landscape form and millennial erosion rates in the San Gabriel Mountains, CA', *Earth and Planetary Science Letters* **289**(1-2), 134–144.

Dielforder, A. and Hetzel, R. (2014), 'The deglaciation history of the Simplon region (southern Swiss Alps) constrained by 10Be exposure dating of ice-molded bedrock surfaces', *Quaternary Science Reviews* **84**, 26–38.

Dunai, T. J. (2010), *Cosmogenic Nuclides: Principles, Concepts and Applications in the Earth Surface Sciences*, Cambridge University Press, New York.

Dunne, J., Elmore, D. and Muzikar, P. (1999), 'Scaling factors for the rates of production of cosmogenic nuclides for geometric shielding and attenuation at depth on sloped surfaces', *Geomorphology* (27), 3–11.

Egholm, D. L., Nielsen, S. B., Pedersen, V. K. and Lesemann, J.-E. (2009), 'Glacial effects limiting mountain height', *Nature* **460**(7257), 884–887.

Ehlers, T. A., Szameitat, A., Enkelmann, E., Yanites, B. J. and Woodsworth, G. J. (2015), 'Identifying spatial variations in glacial catchment erosion with detrital thermochronology', *Journal of Geophysical Research: Earth Surface* **120**(6), 1023–1039.

Ehlers, T., Chaudhri, T., Kumar, S., Fuller, C., Willett, S., Ketcham, R. A., Brandon, M. T., Belton, D. X., Kohn, B. P., Gleadow, A. J. W., Dunai, T. J. and Fu, F. Q. (2005), 'Computational tools for low-temperature thermochronometer interpretation', *Reviews in Mineralogy and Geochemistry* **58**, 589–622.

Foster, M. A. and Anderson, R. S. (2016), 'Assessing the effect of a major storm on 10BE concentrations and inferred basin-averaged denudation rates', *Quaternary Geochronology* **34**, 58–68.

Fox, M., Leith, K., Bodin, T., Balco, G. and Shuster, D. L. (2015), 'Rate of fluvial incision in the Central Alps constrained through joint inversion of detrital 10Be and thermochronometric data', *Earth and Planetary Science Letters* **411**, 27–36.

Galbraith, R. F. (1990), 'The radial plot: Graphical assessment of spread in ages', *International Journal of Radiation Applications and Instrumentation. Part D. Nuclear Tracks and Radiation Measurements* **17**(3), 207–214.

Galbraith, R. F. and Laslett, G. M. (1993), 'Statistical models for mixed fission track ages', *Nuclear Tracks and Radiation Measurements* **21**(4), 459–470.

Gleadow, A. (1981), 'Fission-track dating methods: What are the real alternatives?', *Nuclear Tracks* **5**(1-2), 3–14.

Glotzbach, C., Bernet, M. and van der Beek, P. (2011), 'Detrital thermochronology records changing source areas and steady exhumation in the Western European Alps', *Geology* **39**(3), 239–242.

Glotzbach, C., van der Beek, P., Carcaillet, J. and Delunel, R. (2013), 'Deciphering the driving forces of erosion rates on millennial to million-year timescales in glacially impacted landscapes: An example from the Western Alps', *Journal of Geophysical Research: Earth Surface* **118**(3), 1491–1515.

Gosse, J. C. and Phillips, F. M. (2001), 'Terrestrial in situ cosmogenic nuclides: theory and application', *Quaternary Science Reviews* **20**, 1475–1560.

Granger, D. E., Kirchner, J. W. and Finkel, R. (1996), 'Spatially Averaged Long-Term Erosion Rates Measured from In Situ-Produced Cosmogenic Nuclides in Alluvial Sediment', *Journal of Geology* **104**, 249–257.

Haeuselmann, P., Granger, D. E., Jeannin, P.-Y. and Lauritzen, S.-E. (2007), 'Abrupt glacial valley incision at 0.8 Ma dated from cave deposits in Switzerland', *Geology* **35**(2), 143–146.

Hales, T. C. and Roering, J. J. (2007), 'Climatic controls on frost cracking and implications for the evolution of bedrock landscapes', *Journal of Geophysical Research* **112**(F2).

Hantke, R. and Wagner, G. (2005), 'Eiszeitliche und nacheiszeitliche Gletscherstände im Berner Oberland, erster Teil: östliches Oberland bis zur Kander', *Mitteilungen der Naturforschenden Gesellschaft in Bern* **62**.

Heisinger, B., Lal, D., Jull, A., Kubik, P., Ivy-Ochs, S., Knie, K. and Nolte, E. (2002b), 'Production of selected cosmogenic radionuclides by muons: 2. Capture of negative muons', *Earth and Planetary Science Letters* (200), 357–369.

Heisinger, B., Lal, D., Jull, A., Kubik, P., Ivy-Ochs, S., Neumaier, S., Knie, K., Lazarev, V. and Nolte, E. (2002a), 'Production of selected cosmogenic radionuclides by muons 1. Fast muons', *Earth and Planetary Science Letters* (200), 345–355.

Herman, F. and Braun, J. (2011), 'Glacial hydrology and erosion patterns: A mechanism for carving glacial valleys', *Earth and Planetary Science Letters* **310**(3-4).

Herwegh, M. and Pfiffner, O. (2005), 'Tectono-metamorphic evolution of a nappe stack: A case study of the Swiss Alps', *Tectonophysics* **404**(1-2), 55–76.

Hinderer, M. (2001), 'Late Quarternary denudation of the Alps, valley and lake fillings and modern river loads', *Geodin. Acta* **14**, 231–263.

Hinderer, M., Kastowski, M., Kamelger, A., Bartolini, C. and Schlunegger, F. (2013), 'River loads and modern denudation of the Alps — A review', *Earth-Science Reviews* **118**, 11–44.

Holzhauser, H., Magny, M. J. and Zumbühl, H. J. (2005), 'Glacier and lake-level variations in west-central Europe over the last 3500 years', *The Holocene* **15**(6), 789–801.

Hormes, A., Müller, B. and Schlüchter, C. (2001), 'The Alps with little ice: evidence for eight Holocene phases of reduced glacier extent in the Central Swiss Alps', *The Holocene* **11**(3), 255–265.

Hurford, A. J. and Green, P. F. (1982), 'A users' guide to fission track dating calibration', *Earth and Planetary Science Letters* **59**(2), 343–354.

Hurford, A. J. and Green, P. F. (1983), 'The zeta age calibration of fission-track dating', *Chemical Geology* **41**, 285–317.

Ivy-Ochs, S., Kerschner, H., Reuther, A., Maisch, M., Sailer, R., Schaefer, J., Kubik, P. W., Synal, H.-A. and Schlüchter, C. (2006), 'The timing of glacier advances in the northern European Alps based on surface exposure dating with cosmogenic 10Be, 26Al, 36Cl, and 21Ne', **415**, 43–60.

Ivy-Ochs, S., Kerschner, H., Reuther, A., Preusser, F., Heine, K., Maisch, M., Kubik, P. W. and Schlüchter, C. (2008), 'Chronology of the last glacial cycle in the European Alps', *Journal of Quarternary Science* **23**, 559–573.

Kelly, M., Ivy-Ochs, S., Kubik, P., von Blanckenburg, F. and Schlüchter, C. (2006), 'Chronology of deglaciation based on 10 Be dates of glacial erosional features in the Grimsel Pass region, central Swiss Alps', *Boreas* **35**(4), 634–643.

Kober, F., Hippe, K., Salcher, B., Ivy-Ochs, S., Kubik, P. W., Wacker, L. and Hahlen, N. (2012), 'Debris-flow-dependent variation of cosmogenically derived catchment-wide denudation rates', *Geology* **40**(10), 935–938.

Kohl, C. and Nishiizumi, K. (1992), 'Chemical isolation of quartz for measurement of in-situ -produced cosmogenic nuclides', *Geochimica et Cosmochimica Acta* **56**(9), 3583–3587.

Korschinek, G., Bergmaier, A., Faestermann, T., Gerstmann, U., Knie, K., Rugel, G., Wallner, A., Dillmann, I., Dollinger, G., von Gostomski, C. L., Kossert, K., Maiti, M., Poutivtsev, M. and Remmert, A. (2010), 'A new value for the half-life of 10Be by Heavy-Ion Elastic Recoil Detection and liquid scintillation counting', *Nuclear Instruments and Methods in Physics Research Section B: Beam Interactions with Materials and Atoms* **268**(2), 187–191.

Korup, O. and Schlunegger, F. (2007), 'Bedrock landsliding, river incision, and transience of geomorphic hillslope-channel coupling: Evidence from inner gorges in the Swiss Alps', *Journal of Geophysical Research* **112**(F3).

Kubik, P. W. and Christl, M. (2010), '10Be and 26Al measurements at the Zurich 6MV Tandem AMS facility', *Nuclear Instruments and Methods in Physics Research Section B: Beam Interactions with Materials and Atoms* **268**(7-8), 880–883.

Lal, D. (1991), 'Cosmic ray labeling of erosion surfaces: In situ nuclide production rates and erosion models', *Earth and Planetary Science Letters* **104**, 424–439.

Lal, D. and Peters, B. (1967), Cosmic ray-produced radioactivity on the Earth, *in* S. Fluegge, ed., 'Handbuch der Physik', Springer Verlag, Berlin, pp. 551–612.

Malusà, M. G., Resentini, A. and Garzanti, E. (2016), 'Hydraulic sorting and mineral fertility bias in detrital geochronology', *Gondwana Research* **31**, 1–19.

McPhillips, D. and Brandon, M. T. (2010), 'Using tracer thermochronology to measure modern relief change in the Sierra Nevada, California', *Earth and Planetary Science Letters* **296**(3-4), 373–383.

Naeser, C. W. (1967), 'The use of apatite and sphene for fission track age determinations', *Geological Society of America Bulletin* **78**(12), 1523.

Niemi, N. A., Oskin, M., Burbank, D. W., Heimsath, A. M. and Gabet, E. J. (2005), 'Effects of bedrock landslides on cosmogenically determined erosion rates', *Earth and Planetary Science Letters* **237**(3-4), 480–498.

Nishiizumi, K., Imamura, M., Caffee, M. W., Southon, J. R., Finkel, R. C. and McAninch, J. (2007), 'Absolute calibration of 10Be AMS standards', *Nuclear Instruments and Methods in Physics Research Section B: Beam Interactions with Materials and Atoms* **258**(2), 403–413.

Norton, K. P., Blanckenburg, F., DiBiase, R., Schlunegger, F. and Kubik, P. W. (2011), 'Cosmogenic 10Be-derived denudation rates of the Eastern and Southern European Alps', *International Journal of Earth Sciences* **100**(5), 1163–1179.

Norton, K. P. and Vanacker, V. (2009), 'Effects of terrain smoothing on topographic shielding correction factors for cosmogenic nuclide-derived estimates of basin-averaged denudation rates', *Earth Surface Processes and Landforms* **34**(1), 145–154.

Norton, K. P., von Blanckenburg, F. and Kubik, P. W. (2010), 'Cosmogenic nuclide-derived rates of diffusive and episodic erosion in the glacially sculpted upper Rhone Valley, Swiss Alps', *Earth Surface Processes and Landforms* .

Ouimet, W. B., Whipple, K. X. and Granger, D. E. (2009), 'Beyond threshold hillslopes: Channel adjustment to base-level fall in tectonically active mountain ranges', *Geology* **37**(7), 579–582.

Pfiffner, O. A. (2009), *Geologie der Alpen*, Vol. 8416, 2 edn, Haupt, Bern and Stuttgart and Wien.

Pfiffner, O. A. and Kühni, A. (2001), 'The relief of the Swiss Alps and adjacent areas and its relation to lithology and structure: topographic analysis from a 250-m DEM', *Geomorphology* (41), 285–307.

Robl, J., Prasicek, G., Hergarten, S. and Stüwe, K. (2015), 'Alpine topography in the light of tectonic uplift and glaciation', *Global and Planetary Change* **127**, 34–49.

Roebber, P., Bruening, S., Schultz, D. and Cortinas Jr., J. (2003), 'Improving snowfall forecasting by diagnosing snow density', *Weather Forecasting* **18**, 264–287.

Rolland, C. (2003), 'Spatial and Seasonal Variations of Air Temperature Lapse Rates in Alpine Regions', *Journal of Climate* **16**(7), 1032–1046.

Ruhl, K. W. and Hodges, K. V. (2005), 'The use of detrital mineral cooling ages to evaluate steady state assumptions in active orogens: An example from the central Nepalese Himalaya', *Tectonics* **24**(4).

Salcher, B. C., Kober, F., Kissling, E. and Willett, S. D. (2014), 'Glacial impact on short-wavelength topography and long-lasting effects on the denudation of a deglaciated mountain range', *Global and Planetary Change* **115**, 59–70.

Savi, S., Delunel, R. and Schlunegger, F. (2015), 'Efficiency of frost-cracking processes through space and time: An example from the eastern Italian Alps', *Geomorphology* **232**, 248–260.

Savi, S., Norton, K., Picotti, V., Brardinoni, F., Akçar, N., Kubik, P., Delunel, R. and Schlunegger, F. (2014), 'Effects of sediment mixing on 10Be concentrations in the Zielbach catchment, central-eastern Italian Alps', *Quaternary Geochronology* **19**, 148–162.

Schaller, M., von Blanckenburg, F., Veldkamp, A., Tebbens, L. A., Hovius, N. and Kubik, P. W. (2002), 'A 30 000 yr record of erosion rates from cosmogenic 10Be in Middle European river terraces', *Earth and Planetary Science Letters* **204**(1-2), 307–320.

Schaltegger, U. (1990), 'The Central Aar Granite: Highly differentiated calc-alkaline magmatism in the Aar massif (Central Alps, Switzerland)', *Eur. J. Mineral.* **2**, 245–259.

Schildgen, T., Phillips, W. and Purves, R. (2005), 'Simulation of snow shielding corrections for cosmogenic nuclide surface exposure studies', *Geomorphology* **64**(1-2), 67–85.

Schimmelpfennig, I., Schaefer, J. M., Akçar, N., Koffman, T., Ivy-Ochs, S., Schwartz, R., Finkel, R. C., Zimmerman, S. and Schlüchter, C. (2014), 'A chronology of Holocene and Little Ice Age glacier culminations of the Steingletscher, Central Alps, Switzerland, based on high-sensitivity beryllium-10 moraine dating', *Earth and Planetary Science Letters* **393**, 220–230.

Schlatter, A., Schneider, D., Geiger, A. and Kahle, H.-G. (2005), 'Recent vertical movements from precise levelling in the vicinity of the city of Basel, Switzerland', *International Journal of Earth Sciences* **94**(4), 507–514.

Schlüchter, C. (2004), The Swiss glacial record: a schematic summary, *in* P. L. Gibbard and Ehlers J., eds, 'Quaternary Glaciations: Extent and Chronology Part I: Europe', Elsevier, London.

Schlunegger, F. and Norton, K. P. (2013), 'Water versus ice: The competing roles of modern climate and Pleistocene glacial erosion in the Central Alps of Switzerland', *Tectonophysics* **602**, 370–381.

Schmid, S. M., Fgenschuh, B., Kissling, E. and Schuster, R. (2004), 'Tectonic map and overall architecture of the Alpine orogen', *Eclogae Geologicae Helvetiae* **97**(1), 93–117.

Schmid, S. M., Pfiffner O. A., Froitzheim N., Schönborn G. and Kissling E. (1996), 'Geophysical - geological transect and tectonic evolution of the Swiss-Italian Alps', *Tectonics* **15**, 1036–1064.

Sternai, P., Herman, F., Champagnac, J.-D., Fox, M., Salcher, B. and Willett, S. D. (2012), 'Pre-glacial topography of the European Alps', *Geology* **40**(12), 1067–1070.

Stock, G. M., Ehlers, T. A. and Farley, K. A. (2006), 'Where does sediment come from? Quantifying catchment erosion with detrital apatite (U-Th)/He thermochronometry', *Geology* **34**(9), 725.

Stone, J. O. (2000), 'Air pressure and cosmogenic isotope production', *Journal of Geophysical Research* **105**(B10), 23,753.

Tranel, L. M., Spotila, J. A., Kowalewski, M. J. and Waller, C. M. (2011), 'Spatial variation of erosion in a small, glaciated basin in the Teton Range, Wyoming, based on detrital apatite (U-Th)/He thermochronology', *Basin Research* **23**(5), 571–590.

Valla, P. G., van der Beek, P. A. and Carcaillet, J. (2010), 'Dating bedrock gorge incision in the French Western Alps (Ecrins-Pelvoux massif) using cosmogenic 10 Be', *Terra Nova* **22**(1), 18–25.

van der Beek, P. and Bourbon, P. (2008), 'A quantification of the glacial imprint on relief development in the French western Alps', *Geomorphology* **97**(1-2), 52–72.

Vermeesch, P. (2007), 'Quantitative geomorphology of the White Mountains (California) using detrital apatite fission track thermochronology', *Journal of Geophysical Research* **112**(F3).

Vermeesch, P. (2009), 'RadialPlotter: A Java application for fission track, luminescence and other radial plots', *Radiation Measurements* **44**(4), 409–410.

Vernon, A., van der Beek, P., Sinclair, H. and Rahn, M. (2008), 'Increase in late Neogene denudation of the European Alps confirmed by analysis of a fission-track thermochronology database', *Earth and Planetary Science Letters* **270**(3-4), 316–329.

von Blanckenburg, F. (2005), 'The control mechanisms of erosion and weathering at basin scale from cosmogenic nuclides in river sediment', *Earth and Planetary Science Letters* **237**(3-4), 462–479.

Wagner, G. (2002), 'Die Eiszeitlandschaft im Gebiet Oberes Aaretal–Thunersee', *Jb. Thuner- u. Brienzersee* pp. 11–41.

Ware, E. C., Schultz, D. M., Brooks, H. E., Roebber, P. J. and Bruening, S. L. (2006), 'Improving Snowfall Forecasting by Accounting for the Climatological Variability of Snow Density', *Weather and Forecasting* **21**(1), 94–103.

Werder, M. A., Bauder, A., Funk, M. and Keusen, H.-R. (2010), 'Hazard assessment investigations in connection with the formation of a lake on the tongue of Unterer Grindelwaldgletscher, Bernese Alps, Switzerland', *Natural Hazards and Earth System Science* **10**(2), 227–237.

Whipple, K. X. and Tucker, G. E. (1999), 'Dynamics of the stream-power river incision model: Implications for height limits of mountain ranges, landscape response timescales, and research needs', *Journal of Geophysical Research* **104**(B8), 17,661.

Willett, S. D. (1999), 'Orogeny and orography: The effects of erosion on the structure of mountain belts', *Journal of Geophysical Research* **104**(B12), 28957.

Willett, S. D. and Brandon, M. T. (2002), 'On steady states in mountain belts', *Geology* **30**(2), 175.

Wittmann, H., von Blanckenburg, F., Kruesmann, T., Norton, K. P. and Kubik, P. W. (2007), 'Relation between rock uplift and denudation from cosmogenic nuclides in river sediment in the Central Alps of Switzerland', *Journal of Geophysical Research* **112**(F4).

Zemp, M., Hoelzle, M. and Haeberli, W. (2007), 'Distributed modelling of the regional climatic equilibrium line altitude of glaciers in the European Alps', *Global and Planetary Change* **56**(1-2), 83–100.

5 Summary and conclusions

The main aim of this thesis was to reconstruct the landscape evolution over several glacial and interglacial cycles in the Aar massif in the Central Alps of Switzerland. Detailed discussions of each topic are described in the corresponding chapters. In order to provide a comprehensive overview of this thesis, this chapter includes a short summary of the discussed sections. The results are discussed in terms of their initial objectives (cf. Objectives and background).

5.1 The exhumation history of the Aar massif - tectonics or climate changes ?

During the collision between the Adriatic indenter and the European continent, the Aar massif has begun to shorten. At the very northwest boundary of the massif, rocks yield pre-Alpine ZFT ages (>80 Ma) with shortened fission track lengths that suggest that this part of the massif may have not been deeply buried and may represent the former ZFT PAZ of the Alpine orogeny. Contemporaneously with the shortening, internal parts of the massif may have been overthrust onto the autochthonous rocks within the ZFT PAZ, indicated by an early cooling event at 27 - 19 Ma. Nevertheless, the main phase of exhumation of the Aar massif that caused the onset of exposure, began at 17 Ma, which is almost simultaneously with other external massif of the Western Alps (e.g. Boutoux et al., 2016). This exhumation was rapidly, leading to similar ZFT cooling ages, and was intensified at 13 - 12 Ma. Due to slightly decreasing ZFT ages from the NW to the SE through the massif coinciding with increasing metamorphic grades (Marquer and Burkhard, 1992; Albrecht, 1994; Herwegh and Pfiffner, 2005), the exhumation rates probably increased towards the SE during main exhumation of the massif. According to previously published studies, the onset of main exhumation of the Aar massif is assumed to be the result of exhumation above frontal crustal ramps within the Central Alpine pro-wedge geometry (e.g. Glotzbach et al., 2010; Boutoux et al., 2016).
The dense dataset of AFT and AHe ages reveal an uniform exhumation rate of 0.5 km/Ma since the Late Miocene, confirming detrital thermochronological investigations as well as uniform shortening rates of the Aar massif (Bernet et al., 2001; Glotzbach et al., 2011; Boutoux et al., 2016). Therefore, climatic or tectonic induced exhumation pulses within the Late Miocene/Pliocene are not identified, however, the intensified glacial erosion within the last 2 Ma had an observable impact on the thermochronological age distribution. Effective glacial valley incision led to accelerated exhumation in the valleys and, therefore, to an increased incidence of young AFT and AHe cooling ages at low elevations. Nevertheless, the impact of effective glacial erosion can only be detected for a distinct elevation range and high elevations seem to be nearly unaffected by glacial erosion during the Pleistocene. The

spatial distribution of the AFT and AHe cooling ages yield slightly decreasing ages towards the SE, but this is assumed to be still influenced by spatially variable exhumation rates during the main phase of exhumation of the Aar massif.
Thermal models that are based on these three thermochronometers indeed reveal different time periods with accelerated cooling since the Late Miocene. However, these are strongly elevation-dependent, which suggests that these are rather influenced by perturbed near surface isotherms below a high-relief topography than by different exhumation pulses. A perturbation of near surface isotherms is adopted to result into decreasing cooling rates below ridges and increasing cooling rates below valleys due to widely spaced isotherms and squeezed isotherms below ridges and valleys, respectively. Consequently, previous studies may have produced contradicting exhumation history models, because of a strong dependency on sampled elevation due to a perturbation of near surface isotherms.

5.2 The landscape evolution of inner-Alpine valleys during the glaciations

The glacial erosion during the Pleistocene induced spatially non-uniform cooling in the inner-Alpine valleys. The spatial distribution of thermochronological surface cooling ages and a corresponding AFT age map reveal that the glacial erosion was most effective at a distinct elevation range. The youngest cooling ages do not appear at the lowest point of the valley, instead, they occur at mean elevations between 1000 - 1600 m. This is suggested to be the consequence of focused glacial erosion at this elevation range, because it also does not coincide with numerical models that produced cooling ages in response to steady-state exhumation. The effective glacial erosion caused accelerated cooling of rocks due to increasing exhumation rates balancing the removal at surface. The elevation range coincides with the position of the ELA (= equilibrium line of altitude) of LGM (= Last Glacial Maximum) glaciers, which is assumed to be almost at the same position during every extensive Pleistocene glaciation (e.g. van der Beek and Bourbon, 2008). Therefore, these results lead to the conclusion that glacial erosion during the extensive glaciations of the Pleistocene was concentrated on the position of the ELA.

In addition to this hypothesis, the area around the former ELAs is nowadays characterized by the steepest hillslopes, as a relict of accelerated glacial erosion (e.g. Robl et al., 2015). Consequently, the current appearance of the European Alps is markedly influenced by the impact of effective glacial erosion.

According to a long-term steady-state exhumation, it is assumed that near surface isotherms are adjusted onto the the overlaying topography (e.g. Stüwe et al., 1994). Hence, the isotherms roughly follow the Alpine ridge and valley profile. Focused glacial erosion at mean elevations, therefore, leads to young cooling ages due to increasing local relief. The dimensions of this effect are influenced by the morphology prior the glaciations; the wider the valley the larger the impact.

5.3 The distribution of erosion in the present-day interglacial

The provenance of stream sediments in Alpine catchments demonstrates that the fluvial sediments originate from two distinct elevation ranges, either from 900 - 1600 m or from 2800 - 3400 m, while around 2000 m the erosion is nearly non-existent. It is probable that at high elevations the sediments are produced by glacial erosion, whereas fluvial erosion dominates at low elevations. On the one hand, the present-day ELA is positioned at ~2900 m (e.g. Zemp et al., 2007), suggesting that effective glacial erosion below the ELA (e.g. Herman and Braun, 2008; Egholm et al., 2009; Ehlers et al., 2015; Schlunegger and Norton, 2013) leads to accelerated sediment production.

On the other hand, the low erosion peak coincides with the position of former ELAs of the extensive Pleistocene glaciations. Besides steep hillslope angles at this elevation range, the stream courses demonstrate an increasing occurrence of knickpoints (Fig. 5.1). On the contrary, at high elevations, the stream courses are almost flat, which proves that fluvial erosion is nearly non-existent at these high elevations. However, steep hillslopes as a consequence of effective glacial erosion along former ELAs may be counterbalanced by accelerated fluvial erosion. In summary, glacial erosion below present-day glaciers and relics of previously effective glacial erosion during the Pleistocene still play a decisive role for the Alpine landscape evolution.

Cosmogenic produced ^{10}Be-derived catchment-wide denudation rates are adjusted to the spatial distribution of erosion based on the provenance analyses. These fitted catchment-wide denudation rates reveal that glacial erosion is more effective than fluvial erosion. Glacial erosion yields in denudation rates of $>$1 mm/a, whereas fluvial erosion results in denudation rates of ~0.5 mm/a, which is in accordance to long-term exhumation rates.

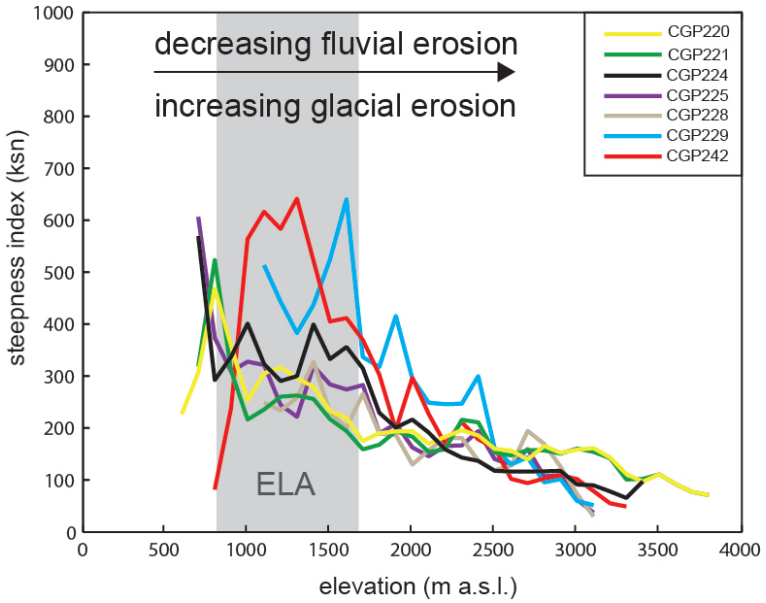

Figure 5.1: Mean ksn values of all streams within the corresponding catchment composited into mean values of bins of 100 m elevation. The ksn "steepness index" expresses the slope differences in relation to the size of catchment area. It is based upon Flint's law (Hack, 1957; Flint, 1974) and useful to identify knickzones in stream courses, which are sections of a stream course that are steeper than their surrounding segments (e.g. Whipple and Tucker, 1999). Therefore, high ksn values express the increasing occurrence of knickzones.

5.4 Conclusions

The first cooling of rocks in the Aar massif has begun at 27 Ma, contemporaneously with the onset of overall shortening within the massif. Presumably, internal thrusting caused first early cooling events. However, the main exhumation of the Aar massif that led to the exposure of crystalline rocks began at 17 Ma and lasted until 13 - 12 Ma. The exhumation was rapid with increasing rates from the NW to the SE. Since Late Miocene, the massif has been exhumed uniformly with 0.5 km/Ma, without evidence for accelerated exhumation associated with tectonics or climatic changes, except for the last 2 Ma. The global cooling in the Pleistocene caused effective glacial valley incision that led to accelerated exhumation at a distinct elevation range, which was not at the valley bottom. The elevation range coincided with the position of the equilibrium line of altitude (ELA) of the largest Pleistocene glaciations, which leads to the conclusion that the glacial erosion was particularly effective at the ELA. Presumably, around the ELA, the erosion propagated headwards and caused high valley incision rates. The dimensions of this effect were influenced by the pre-glacial topography, so that the glacial erosion became more effective in wide valleys.
As a relict of effective glacial erosion, the position of the former ELAs of Pleistocene glaciers is nowadays characterized by the steepest hillslope angles. Consequently, during the present-day interglacial, the fluvial erosion is focused on this elevation range, whereas glacial erosion is focused on the ELA of present-day glaciers. Therefore, these two elevation ranges mainly control the provenance of present-day stream sediments, while nowadays the glacial erosion is at least twice as effective as the fluvial erosion. Hence, the glacial erosion of past and present glaciers affect remarkably the present-day shape of inner Alpine valleys. The present-day fluvial erosion is still responding to the large impact of Pleistocene glaciations in order to achieve a geomorphic steady-state and its rates are in the same order as long-term exhumation rates. Accordingly, glacial erosion has a major impact on the Alpine landscape evolution leading to accelerated exhumation, whereas fluvial erosion is balanced by the exhumation.

References

Albrecht, J. (1994), 'Geologic units of the Aar massif and their pre-Alpine roch associations: a critical review', *Schweiz. Mineral. Petrogr. Mitt.* **74**, 5–27.

Bernet, M., Zattin, M., Garver, J. I., Brandon, M. T. and Vance, J. A. (2001), 'Steady-state exhumation of the European Alps', *Geology* **29**(1), 35.

Boutoux, A., Bellahsen, N., Nanni, U., Pik, R., Verlaguet, A., Rolland, Y. and Lacombe, O. (2016), 'Thermal and structural evolution of the external Western Alps: Insights from (U–Th–Sm)/He thermochronology and RSCM thermometry in the Aiguilles Rouges/Mont Blanc massifs', *Tectonophysics* **683**, 109–123.

Egholm, D. L., Nielsen, S. B., Pedersen, V. K. and Lesemann, J.-E. (2009), 'Glacial effects limiting mountain height', *Nature* **460**(7257), 884–887.

Ehlers, T. A., Szameitat, A., Enkelmann, E., Yanites, B. J. and Woodsworth, G. J. (2015), 'Identifying spatial variations in glacial catchment erosion with detrital thermochronology', *Journal of Geophysical Research: Earth Surface* **120**(6), 1023–1039.

Flint, J. J. (1974), 'Stream Gradient as a function of order, magnitude and discharge', *Water Resour. Res.* **10**, 969–973.

Glotzbach, C., Braun, J. and van der Beek, P. (2015), 'A Fourier approach for estimating and correcting the topographic perturbation of low-temperature thermochronological data', *Tectonophysics* **649**, 115–129.

Glotzbach, C., Reinecker, J., Danišík, M., Rahn, M., Frisch, W. and Spiegel, C. (2010), 'Thermal history of the central Gotthard and Aar massifs, European Alps: Evidence for steady state, long-term exhumation', *Journal of Geophysical Research* **115**(F3).

Glotzbach, C., van der Beek, P. and Spiegel, C. (2011), 'Episodic exhumation and relief growth in the Mont Blanc massif, Western Alps from numerical modelling of thermochronology data', *Earth and Planetary Science Letters* **304**(3-4), 417–430.

Hack, J. T. (1957), 'Studies of longitudinal stream profiles in Virginia and Maryland', *U.S. Geological Survey Paper* **294**(97).

Herman, F. and Braun, J. (2008), 'Evolution of the glacial landscape of the Southern Alps of New Zealand: Insights from a glacial erosion model', *Journal of Geophysical Research* **113**(F2).

Herwegh, M. and Pfiffner, O. (2005), 'Tectono-metamorphic evolution of a nappe stack: A case study of the Swiss Alps', *Tectonophysics* **404**(1-2), 55–76.

Marquer, D. and Burkhard, M. (1992), 'Fluid circulation, progressive deformation and mass-transfer processes in the upper crust: the example of basement-cover relationships in the External Crystalline Massifs, Switzerland', *Journal of Structural Geology* **14**(8/9), 1047–1057.

Robl, J., Prasicek, G., Hergarten, S. and Stüwe, K. (2015), 'Alpine topography in the light of tectonic uplift and glaciation', *Global and Planetary Change* **127**, 34–49.

Schlunegger, F. and Norton, K. P. (2013), 'Water versus ice: The competing roles of modern climate and Pleistocene glacial erosion in the Central Alps of Switzerland', *Tectonophysics* **602**, 370–381.

Stüwe, K., White, L. and Brown, R. (1994), 'The influence of eroding topography on steady-state isotherms. Application to fission track analysis', *Earth and Planetary Science Letters* **124**(1-4), 63–74.

van der Beek, P. and Bourbon, P. (2008), 'A quantification of the glacial imprint on relief development in the French western Alps', *Geomorphology* **97**(1-2), 52–72.

Whipple, K. X. and Tucker, G. E. (1999), 'Dynamics of the stream-power river incision model: Implications for height limits of mountain ranges, landscape response timescales, and research needs', *Journal of Geophysical Research* **104**(B8), 17,661.

Zemp, M., Hoelzle, M. and Haeberli, W. (2007), 'Distributed modelling of the regional climatic equilibrium line altitude of glaciers in the European Alps', *Global and Planetary Change* **56**(1-2), 83–100.

Acknowledgements/Danksagung

Während der langen Reise zu dieser Dissertation, die im Rahmen des DFG-geförderten Projekts: GL 724/3-1 finanziert wurde, wurde ich von zahlreichen Menschen in unterschiedlichster Weise begleitet. Bei Folgenden möchte ich mich besonders herzlich bedanken.
Mein besonderer Dank gilt Dr. Christoph Glotzbach, der mir überhaupt die Möglichkeit gegeben hat, diese Arbeit zu schreiben. Desweiteren danke ich dir insbesondere für die Unterstützung während der Geländearbeiten, am Mikroskop und dafür, dass ich immer zu dir kommen konnte und du dir immer Zeit genommen hast meine Fragen zu beantworten.
Prof. Dr. Ulrich Heimhofer danke ich, dass er sich bereit erklärt hat, diese Arbeit zu begutachten. Bei Dr. Andreas Wölfler möchte ich mich bedanken, dass er mich bei der Vorbereitung zur (U-Th-Sm)/He Analyse an Apatiten unterstützt hat und für die geduldige Beantwortung meiner Fragen, insbesondere innerhalb des letzten halben Jahres. Ein Danke auch an die Arbeitsgruppe Prof. Dr. Andrea Hampel. Dr. István Dunkl und Dr. Steve Binnie möchte ich für die Hilfe bei analytischen Fragen und bei der Probenaufbereitung an den jeweiligen Unis in Göttingen und Köln danken.
Desweiteren gilt mein besonderer Dank meinen Hiwis, wobei ich hier insbesondere Lars Lindner hervorheben möchte, der mit uns zusammen die Schweizer Berge hochgeklettert ist um sie dann mit schwerem Gepäck wieder runterzugehen. Hierbei bedanke ich mich auch bei Dr. Philipp Häuselmann der uns eine interessante Führung durch die St. Beatus-Höhlen gab und durch die mir auch nochmal bewusst geworden ist, dass ich in diesem Leben kein Speläologe mehr werde.
Mein großer Dank gilt auch noch meinen lieben (ehem.) Kollegen und ehem. Masteranten für sehr schöne, aufschlussreiche, hilfreiche, kaffeegetränkte, kuchengestärkte, feierabendliche Unterhaltungen. Danke, Katharina, Nils, Meike, Philipp, Maurits, Julia, Moritz, Dominik, Lena, George, Jean, Lars, Jörg, Fanfan und Gang.
Privat wurde ich auch sehr gut unterstützt und hier gebührt der Dank insbesondere Gaby und meiner Familie, die immer an mich geglaubt hat. Und dann noch ein Danke an meinen Markus. Für alles.

Curriculum vitae

Name:	Cornelia Wangenheim
Geburtstag:	26.05.1987
Geburtsort:	Oldenburg (Oldb)
Staatsangehörigkeit:	Deutsch

07/2006	**Abitur**
10/2006 - 09/2009	**Bachelor of Science (Geowissenschaften)**
	Leibniz Universität Hannover
08/2010 - 01/2011	**Auslandssemester**
	Stockholms Universitet, Schweden
10/2009 - 09/2012	**Master of Science (Geowissenschaften)**
	Leibniz Universität Hannover

2013 - 2016	**Wissenschaftliche Mitarbeiterin**
	Institut für Geologie, Leibniz Universität Hannover
2013 - 2016	**Promotionsstudium**
	Institut für Geologie, Leibniz Universität Hannover

Conference contributions (Abstracts)

Wangenheim, C., Glotzbach, C.: Quantifying Glacial Erosion in the European Alps with Thermochronological Age Distributions, AGU Fall Meeting, San Francisco 2015 (Poster)

Wangenheim, C., Glotzbach, C.: Quantifying glacial erosion in the European Alps using apatite fission track dating, EGU, Vienna 2015 (Oral presentation)

Herwegh, M., Mock, S., Wehrens, P., Baumberger, R., Berger, A., **Wangenheim, C.**, Glotzbach, C., Kissling, E.: The Front of the Aar Massif: A Crustal-Scale Ramp Anticline?, EGU, Vienna 2015

Wangenheim, C., Glotzbach, C., Kubik, P. W.: Quantifying glacial erosion combining bedrock and detrital thermochronology in the Bernese Alps, 14th International Conference on Thermochronology, Chamonix 2014 (Poster)